Hydraulic Actuator Force Control: Quantitative Design and Stability Analysis

by

Masoumeh Esfandiari

A Thesis submitted to the Faculty of Graduate Studies of
The University of Manitoba
in partial fulfilment of the requirements of the degree of

Doctor of Philosophy

Department of Mechanical Engineering
The University of Manitoba

Abstract

Automotive active suspension, advanced seismic testing, and force/torque emulations of space manipulators are examples of applications, where the hydraulic actuator force control is required. In double-rod hydraulic actuators, where the piston area is equal in both the actuator chambers, the actuator force is the differential pressure across the actuator multiplied by the piston effective area. Having this proportional relationship between the actuator force and the differential pressure, the focus of this work is to control the actuator force of a double-rod hydraulic actuator by controlling the differential pressure across the actuator. The double-rod hydraulic actuator of this study is run by two independent circuits: 1) electro-hydraulic actuation, where a flow control valve and high supply pressure are employed, and 2) electro-hydrostatic actuation, where a fixed-displacement pump and variable speed electric motor are employed. In general, developing controllers for hydraulic actuators is challenging due to the presence of parametric uncertainties and uncertain nonlinearities in these actuators. For electro-hydraulic actuation, the hydraulic function becomes highly nonlinear which adds to the complexity of the control problem. In electro-hydrostatic actuation, high inertia of rotational parts in electric motor lowers the dynamic performance of the system. Also, a specific challenge in force control of hydraulic actuators is the limiting effect of environment dynamics on the maximum achievable tracking bandwidth.

Considering the above challenges, in this research for the first time, quantitative feedback theory (QFT) is employed to control the hydraulic actuator force. Using QFT, a robust, linear, fixed-gain, and low-order controller is designed for each actuation system which: (*i*) keeps the closed-loop response within desired tracking bounds (*ii*) guarantees the closed-loop stability around desired operating points, (*iii*) rejects disturbance within desired tolerances, and (*iv*) achieves desired tracking bandwidth, despite the presence of parametric uncertainties in the hydraulic system and environment. Among the performance criteria, special attention is paid to achieve high tracking bandwidth. Trade-offs between different performance criteria towards achieving high tracking bandwidth, are discussed. Experimental results are presented to validate that the performance criteria are satisfied by the designed QFT controllers.

The QFT controllers are synthesized based on the families of frequency responses of the hydraulic actuation systems. For the electro-hydraulic actuation system, the family of frequency responses is obtained by linearizing the hydraulic nonlinear function around operating points of interest. For the electro-hydrostatic actuation system, the family of frequency responses is derived by applying an advanced form of fast Fourier transform on experimental input-output data. This means that the designed QFT controllers guarantee the stability of the closed-loop system, only for these families of the frequency responses. In this thesis, to investigate the nonlinear stability of the closed-loop systems with QFT controllers, for the first time, Takagi-Sugeno (T-S) fuzzy modeling and its corresponding stability theory are used. The stability conditions are presented in the form of linear matrix inequalities (LMIs). As a result, the nonlinear stability of the designed QFT controllers for both the actuation systems is proven in the presence of parametric uncertainties.

To my parents

and

to my love

Mansoor

Acknowledgments

I would like to sincerely thank my PhD adviser, Professor Nariman Sepehri, for his invaluable and incredible advice, support, and help through all parts of my PhD research including theoretical development, experiments, and publications. By his guidance and patiently sharing his in-depth knowledge, I have gained incredible experience on hydraulic actuation systems at the Fluid-power and Tele-robotics Laboratory.

I sincerely appreciate all of considerations of my internal advisory committee at the University of Manitoba, Professor Balakrishnan (Bala) and Professor Filizadeh, for their careful reviews, and helpful comments and suggestions on my PhD thesis and before in progress report sessions during the course of my research. I also sincerely appreciate all of considerations of my external examiner, Professor Shi for his careful review, comments and suggestions on my PhD thesis. During my PhD studies at the University of Manitoba, I have also had the opportunity to know Professor Wu as my inspiration for being a very successful and considerate woman professor in engineering.

I wish to thank my lab mates for all the friendship and laughter we had together.

I wish to send my gratitude to my beloved family, especially my parents who have always supported me in anyways they could.

Lastly and most important to my love, Mansoor who stood by me in difficult time and unconditionally offered his love, friendship, and support. He reminded me how limitless, strong, and competent we can be and I am grateful to share this life journey with him, a journey with no limit and no end!

Contents

List of Figures

List of Tables

Nomenclature

Parameters and Variables

x_p	actuator displacement (m)
v_p	actuator velocity (m/sec)
Q_1, Q_2	hydraulic fluid flows (m^3/sec)
P_1, P_2	pressures in each side of actuator (Pa)
P_L	output pressure (Pa)
u_v	control signal to servovalve (V)
f_a	actuator force (N)
f_s	interacting force (N)
f_l , f_f	external and friction forces (N)
m_e	environment mass (kg)
m_h	total mass of piston and rod (kg)
d_h	hydraulic viscous damping (N.sec/m)
d_e	environment damping (N.sec/m)
k	environment stiffness (N/m)
P_s, P_r	hydraulic supply and return pressures (Pa)
A	piston area (m^2)
V_1, V_2	volume of actuator chambers (m^3)
V_t	total volume of actuator chambers (m^3)
k_{sp}	spool valve position gain (m/V)
τ	servovalve time constant (sec)
x_v	spool displacement (m)
w	valve orifice area gradient (m^2/m)
β	fluid bulk modulus (Pa)
k_e, k_i	external and internal leakage coefficients (m^3/sec/Pa$^{1/2}$)
k_p, k_{1p}, k_{2p}	flow pressure coefficients (m^3/sec/Pa)
k_s, k_{1s}, k_{2s}	valve flow gains (m^2/sec)
K_v	flow coefficient (m$^{3/2}$/kg$^{1/2}$)
Q_U, Q_D	flows at pump inlet and outlet (m^3/sec)
P_U, P_D	pressures at pump inlet and outlet (Pa)
u_m	control signal applied to servodrive (V)
ω_m	velocity of servomotor (rad/sec)
k_m	servomotor gain (rad/V.sec)
τ_m	servomotor time constant (sec)
D_p	pump displacement (m^3/rev)
C_{ep}, C_{ip}	pump external and cross-port leakage coefficients (m^3/sec/Pa$^{1/2}$)
P_{pipe}	pressure drop across pipes (Pa)
σ_0	average stiffness of bristles in LuGre friction model (N/m)
σ_1	micro damping of bristles in LuGre friction model (N.sec/m)
F_s, F_c	stiction and Coulomb friction forces (N)
v_s	Stribeck velocity (m/sec)

Transfer Functions

C	controller
F	pre-filter
$G_{P_L}(s, \alpha)$	equivalent linear transfer functions for electro-hydraulic actuator
S	sensitivity
T	complementary sensitivity

Vectors and Matrices

$\boldsymbol{A}_\rho^*$, $\boldsymbol{B}_\rho^*$	matrices defined in T-S fuzzy model of hydraulic actuator
$\boldsymbol{x}$	state vector of hydraulic actuator
$\boldsymbol{x_c}$	state vector of QFT controller

Chapter 1

Introduction

1.1 Motivation

Hydraulic actuators have high force-to-weight ratio, capability of producing linear movement, and fast response. Hydraulic actuators have higher stiffness than electrical motors, which means little drop in speed when loads are applied (Merritt, 1967). Hydraulic fluid provides an exceptional characteristic for hydraulic actuators by taking the generated heat out to a heat exchanger, and due to lubricant characteristic of the fluid, the components have long life. Hydraulic actuators can hold a load over an extended time, without generating excessive heat, which is a usual case for electric actuators (Merritt, 1967). These advantages make hydraulic actuators appropriate choices for a wide range of industrial applications (Merritt, 1967). Some of these applications are crane operation (Melik-Gaikazov et al., 1975), aircraft flight-control surfaces (Bowers et al., 1996), automotive active suspension (Hrovat, 1997), injection molding devices (Newton, 1969), and force/torque emulation of space manipulators (Zhu and Piedboeuf, 2005). In these applications, one of the following variables is controlled: (*i*) actuator position, (*ii*) interacting force, and (*iii*) actuator force. The difference between the actuator force and the interacting force is explained as follows. A typical hydraulic actuation system controls the flow of fluid into and out of the actuator chambers. As a result, a pressure differential, also known as the output pressure is built-up between the two chambers. This pressure acts on the piston effective area and generates the actuator force (see Figure 1.1). In double-rod hydraulic actuators, the actuator force is the output pressure multiplied by the piston effective area, and therefore has a proportional relationship with the output pressure. The actuator force accelerates the actuator itself and deals with the friction between the piston and the cylinder walls. The rest of the actuator force is applied on environment and deals with external forces. This force is called the interacting force and can be measured by a force sensor. In real-life applications, attaching a force sensor at the end of the rod can be challenging (Nabulsi et al., 2007).

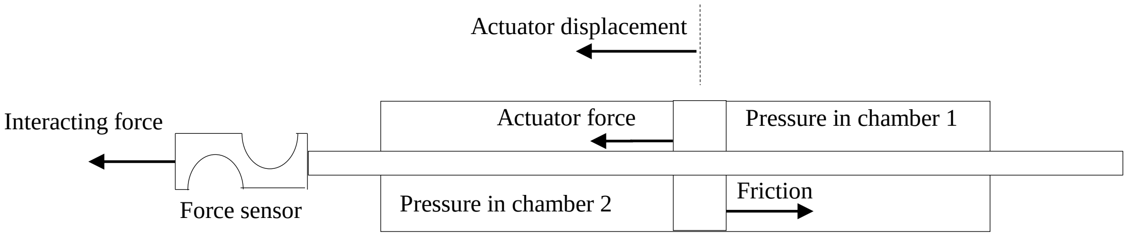

Figure 1.1. Double-rod hydraulic cylinder.

In this thesis, the control variable is the actuator force of a double-rod hydraulic actuator, and due to the proportional relationship between the actuator force and the output pressure in double-rod hydraulic actuators, the actuator force is controlled alternatively by controlling the output pressure. As a result, here the two terms of the actuator force and the output pressure are interchangeably used.

Developing control systems for hydraulic actuators has been challenging (Niksefat and Sepehri, 2001). Hydraulic actuators are subjected to a great deal of uncertain nonlinearities, and parametric uncertainties. Examples of uncertain nonlinearities are leakage, friction, and external disturbances. The values of the parameters of hydraulic actuation systems (e.g. bulk modulus and viscous coefficient) change with time and with variations in environmental conditions such as temperature (Yao et al., 2000; Chinniah, 2004; Turolla, 2013). For electro-hydraulic actuators, where the control valve directs the fluid flow, the hydraulic function becomes highly nonlinear, which adds to the complexity of the control problem. Another challenge specifically associated with the force control of hydraulic actuators, either the actuator force or interacting force, is the limiting effect of environment dynamics on the maximum achievable tracking bandwidth (Dyke et al., 1995). The environment dynamics appear in the force dynamics through a “natural velocity feedback” path in hydraulic systems (Alleyne and Liu, 1999; Lamming, 2009). This phenomenon causes the magnitude of the force response to drop significantly at the natural frequency of the environment, preventing the actuator from properly applying force at this frequency (Alleyne and Liu, 1999; Sivaselvan et al., 2008).

Stability is another important criterion in the developing of actuator force control systems. Guaranteed nonlinear stability for the control systems developed based on Lyapunov theory has been achieved at the cost of complexity, high computational burden, and need for various sensory data (Liu and Alleyne, 2000). On the other hand, output-feedback linear controllers with low computational burden provide only small-signal stability around operating points (Niksefat and Sepehri, 2001; Banos and Horowitz, 2004).

In addition to force control in electro-hydraulic actuators, force control of electro-hydrostatic actuators has been a new topic in recent literature, due to higher energy efficiency, easier maintenance, and lower price of electro-hydrostatic counterparts than electro-hydraulic actuators (Truong et al., 2007; Ahn et al., 2008; Lovrec and Kastrevc, 2011). The above advantages in electro-hydrostatic actuators have been obtained due to a different flow control mechanism than that in electro-hydraulic actuators. Electro-hydrostatic actuators utilize variable rotational speed motors and fixed-displacement pumps to control the flow instead of flow control valves connected to high supply pressure (Habibi and Goldenburg, 1999). Due to the rising price of energy, and the falling price of frequency inverters and servomotors, demand for electro-hydrostatic actuators has increased (Radermacher et al., 2013). However, electro-hydrostatic actuators have lower dynamic performance as compared with electro-hydraulic actuators, due to high inertia of rotational parts in the variable speed electric motor (Lovrec and Ulaga, 2007; Radermacher et al., 2013). Therefore, there is a need to develop controllers that can exploit the maximum performance of electro-hydrostatic actuators (Radermacher et al., 2013).

By developing stable and robust control systems that satisfy desired performance criteria in the actuator force response, hydraulic actuators can be considered as reliable and high performance sources of force. In the next section, efforts that have been done so far to control both the actuator force and the interacting force in electro-hydraulic actuators as well as electro-hydrostatic actuators are presented.

1.2 Review of Force Control in Hydraulic Systems

1.2.1 Electro-Hydraulic Actuation

In this section, first efforts to deal with challenges in the control of the actuator force and the output pressure of electro-hydraulic actuators are presented. To compensate the undesirable effect of environment dynamics on the performance of force control systems, Conrad and Jensen (1988) suggested using a positive feedback from the velocity of the actuator at the point of its attachment to the environment. Therefore the approach required a velocity sensor. The velocity is then combined with the control signal in the force control loop. The above structure is known as the "velocity correction loop" (Conrad and Jensen, 1988). Dimig et al. (1999) used this concept to control the actuator force for the effective force testing in the seismic testing techniques.

Alleyne and Liu (1999) used an example of a PID controller and explained that PID controllers cannot resolve the bandwidth limitation problem in the control of actuator force. Same authors demonstrated that in comparison to simple linear controllers, nonlinear controllers provide a better performance and higher tracking bandwidth in actuator force control (Alleyne and Liu, 1999; 2000). They designed a Lyapunov-based nonlinear controller with adaptation law to control the actuator force, which achieved a bandwidth of 20 Hz (Liu and Alleyne, 2000). A limited number of uncertain parameters were considered in their work. They also employed the passivity theory to design a robust output pressure controller similar to the back-stepping method to decouple state errors, but the model of environment and full state feedback were required (Alleyne and Liu, 2000). Yao et al. (2012) designed a nonlinear adaptive robust actuator force controller for the hydraulic load simulator and increased robustness against nonlinear uncertainties. However, the achieved bandwidth in tracking results was around 0.25 Hz. From the above literature, the researchers have investigated using either simple PID controllers or complex nonlinear controllers for actuator force control, while PID controllers cannot resolve the bandwidth limitation in force control and nonlinear controllers require several sensors. The performance of robust fixed-gain linear controllers which are more complex that PID, but less complex than nonlinear controllers, have not been investigated in actuator force control, especially in terms of maximum achievable bandwidth. Robust fixed-gain linear controllers are easier to implement and require less sensory data than nonlinear controllers. Research on using H_∞ technique to design a fixed-gain linear controller for the aerodynamic loading system showed a poor performance on tracking bandwidth, i.e., less than 1 Hz (Laval et al., 1996). In this thesis, Quantitative feedback theory (QFT), introduced by Horowitz (1993) is selected as s suitable technique to design robust fixed-gain linear controllers for the actuator force. The reasons of the suitability of this selection along with a short description on QFT technique are given as follows. QFT design technique guarantees robust performance and stability for the control system within a certain range of inputs-outputs of the system, and in the presence of bounded parametric uncertainties (Horowitz, 1993). The QFT controller is designed in the frequency domain using Nichols chart and Bode diagram. In this technique, the frequency responses of the original nonlinear plant within a certain input-output sets are represented in the Nichols chart, known as plant templates. Using these plant templates, the performance constraints such as stability, tracking, and disturbance rejection are graphically presented in the Nichols chart. At the end, the QFT controller is a transfer function that makes the loop transmission function to satisfy the QFT bounds in the Nichols chart. The graphical representation of design criteria and graphical controller design in the Nichols chart, result in a reasonable trade-off between the complexity of the controller and satisfying the design criteria. In addition, QFT controller is fixed-gain and linear, which reduces online computations as compared with nonlinear time variant robust control techniques. For the first time, the author of this thesis employed QFT design technique to improve the actuator force/output pressure tracking bandwidth, as well as satisfying tracking, stability, and disturbance rejection requirements in double-rod electro-hydraulic actuators (Esfandiari and Sepehri, 2014).

Major efforts in interacting force control of electro-hydraulic actuators are as follows. Jacazio and Balossini (2005) employed velocity correction loop to control the interacting force in testing of flight-control surfaces in an airplane, and achieved the high accuracy in force control, in the presence of different disturbances. Plummer (2007) designed a load velocity feedback filter and employed compliance between the actuator and the environment in the form of spring to improve the performance of the interacting force control system and achieved a bandwidth of 30 Hz in aerodynamic force emulation of Formula One car test rig. In this work, uncertainty was only considered for the environment, and in addition to force sensor, the motion sensor was required. QFT was successfully used to control the interacting force in stiffness dominant environments (Niksefat and Sepehri, 1999; 2000). To control the interacting force in a hardware-in-the-loop load emulator, QFT technique was employed (Karpenko and Sepehri, 2012). The same technique was used for the interacting force control of a three-axis road simulator, with acceptable tracking performance, but no discussion was presented on the effects of environment dynamics on the maximum achievable bandwidth (Kim et al., 2011). Nam (2001) designed a QFT controller for the interacting force of aerodynamic load simulator, in which the performance of the system was investigated via only simulations.

1.2.2 Electro-Hydrostatic Actuation

For electro-hydrostatic actuators, the literature on the control of the outlet pressure of the pump is described here. Lovrec and Ulaga (2007) presented a detailed comparison between the outlet pressure responses of a pump-controlled hydraulic actuator and an electro-hydrostatic actuator, using PID controllers. Pump-controlled hydraulic actuators utilize constant speed motors with variable-displacement pumps. Authors showed that the pressure response of the electro-hydrostatic actuator is slower than that of the pump-controlled actuation system (Lovrec and Ulaga, 2007). In another work, outlet pressure control was implemented by a PID controller, in a press-brake hydraulic machine using a combination of an induction motor and a fixed-displacement pump within an energy-saving load-sensing drive concept (Lovrec et al., 2009). In the above studies, the performance of the systems was only examined via step input references; no results on tracking bandwidth were provided. Aside from the above work on the outlet pressure control of the pump in electro-hydrostatic actuators, there has not been any research on the robust control of differential pressure across the actuator in electro-hydrostatic actuation systems.

To improve the performance of PID controllers in controlling the interacting force of electro-hydrostatic actuators dealing with variable stiffness environments, an intelligent switching control technique was utilized (Ahn and Chau, 2006). In this technique, based on the value of the environment stiffness, a specific PID controller was selected for the control loop. The performance of the controller was experimentally evaluated using a set-up equipped with a fixed-displacement pump, an AC servomotor, and a single-rod hydraulic actuator (Ahn and Chau, 2006). To improve the performance of PID controllers to deal with varied external loading, fuzzy membership functions were employed in the interacting force control of electro-hydrostatic actuators (Truong et al., 2007). In this technique, each gain of the PID controller was tuned by an independent fuzzy tuner. The resulting adaptive controller experimentally showed better tracking performance in the presence of varied disturbances as compared with the conventional PID controllers (Truong et al., 2007). In order to add learning ability to fuzzy-PID controllers, robust extended Kalman filter (REKF) was employed (Ahn and Truong, 2009). Using REKF the ideal state vector of the fuzzy PID controller was estimated for the next step based on the current error, the current state vector, and previous data. The experimental results of applying online tuning REKF fuzzy-PID controller showed significant improvement in performance and higher tracking precision of the control systems as compared with the conventional fuzzy-PID or the PID controllers (Ahn and Truong, 2009). While PID controllers are popular due to their simple design and implementation, above techniques improved the performance of force control systems by eliminating this simplicity and using nonlinear time-varying terms in PID controllers. In terms of fixed-gain linear controllers, QFT was utilized to control the interacting force of electro-hydrostatic actuators in load simulators (Dinh et al., 2008). In this work, the family of linear time invariant transfer functions was obtained from experimental frequency responses. QFT controller was designed to satisfy the tracking performance, stability, and disturbance rejection for the family of transfer functions. The transient response specifications were set for a settling time less than 1 sec and overshoot less than 5% (Dinh et al., 2008). In order to improve the performance of QFT controllers to deal with large uncertainties in interacting force control, online tuning of the coefficients of QFT controllers was outlined by Truong et al. (2008).

1.3 Objectives and Methodology

The first objective of this thesis is to develop robust, linear, low-order, and fixed-gain controllers for the actuator force/output pressure of electro-hydraulic and electro-hydrostatic actuators which are subjected to parametric uncertainties. The controllers are required to provide high tracking bandwidth, disturbance rejection, stability, and acceptable time and frequency responses for the closed-loop system. These criteria must be satisfied despite parametric uncertainties in the actuation systems and environment. This is the first attempt on the actuator force control based on QFT, where only the actuator chamber pressures are employed (Esfandiari and Sepehri, 2014).

In order to achieve the above objective, QFT is selected as the design methodology. To design QFT controllers, the family of frequency responses of the actuation systems for the entire range of parametric uncertainties is required. For the electro-hydraulic actuator, the family of frequency responses is obtained by linearization of the hydraulic nonlinear function around operating points of interest, using small-signal method. This linearization approach accurately represents the hydraulic dynamics around the operating points. Also it allows considering a wide range of parametric uncertainties in the obtained linearized models, without causing high computational burden. Challenges towards achieving a high bandwidth output pressure control of hydraulic actuators are described. This discussion is carried out by hypothetical increase in the tracking bandwidth, assigned in the performance criteria. It will be shown how satisfying high bandwidth criterion results in lowering the robust stability of the closed-loop system as well as deteriorating the performance in transient step response. The results of the discussion are used in the QFT controller design. For the electro-hydrostatic actuator, due to the lack of information on the uncertainty ranges of parameters, the small-signal approach cannot be employed. Instead, the family of frequency responses are obtained directly by applying an advanced form of fast Fourier transform on the experimental inputs-outputs data. The method provides high quality frequency responses of the electro-hydrostatic actuator. For both electro-hydraulic and electro-hydrostatic actuators, the results of applying the QFT controllers on the experimental set-up are presented.

The second objective of this research is to analyze the nonlinear stability of the closed-loop systems. QFT controllers only guarantee the closed-loop stability for the family of frequency responses that the controllers were initially designed for. The family of frequency responses represent the real system only over specific operating conditions and input-output sets, or for particular values of system parameters. To investigate the nonlinear stability of the designed QFT controllers without the above limitations, Takagi-Sugeno (T-S) fuzzy modeling and its corresponding stability theory are employed. The suggested solution has been presented by the author of this thesis for the first time (Esfandiari and Sepehri, 2013). T-S fuzzy models are formed as weighted sum of linear models, which blend easily with linear QFT controllers

(Tanaka and Wang, 2001). This way, the nonlinear stability of the closed-loop system can be investigated in the presence of parametric uncertainties, friction, and internal and external leakages. Stability conditions are then presented in the form of linear matrix inequalities (LMIs), which can be solved using MATLAB LMI Toolbox (Boyd et al., 1994; Gahinet et al., 1995).

1.4 Thesis Outline

Chapter 2 presents the description of the electro-hydraulic and the electro-hydrostatic actuation systems under study. Mathematical models describing both the actuation systems are also presented.

Chapter 3 presents an overview of QFT design technique, design steps, and relationship between performance criteria. The information presented in this chapter is used in Chapters 5 and 6 in order to design the robust QFT controllers.

Chapter 4 presents T-S fuzzy modeling and its stability theory. In this chapter, a T-S fuzzy model for the double-rod electro-hydraulic actuator is derived. The effectiveness of the T-S fuzzy modeling and its stability theory to analyze the stability of the closed-loop systems of hydraulic actuators is verified by considering three case studies. The first two case studies are already-developed nonlinear controllers for hydraulic actuators based on passivity and Lyapunov theories. In the third case study, the nonlinear stability of a recently developed QFT position controller for a parametrically uncertain hydraulic actuator is investigated. Overall, this chapter provides enough practical examples to support using T-S fuzzy modeling and its stability theory with confidence in analyzing the stability of QFT controllers developed through next chapters.

In Chapter 5, a QFT controller is designed for the output pressure of the electro-hydraulic actuator. First, using small-signal method, the family of frequency responses of the electro-hydraulic actuator is obtained. Using the family of frequency responses, a QFT controller is designed to provide acceptable time and frequency responses, disturbance rejection, and stability for the closed-loop system. A detailed discussion is presented next, on challenges of using QFT to increase the tracking bandwidth in the output pressure of electro-hydraulic actuators. The conflicts between performance criteria towards achieving a higher bandwidth are discussed. The results are used to redefine the performance criteria and then design a new QFT controller and pre-filter which provide higher tracking bandwidth for the closed-loop system. The experimental results of applying the controller with higher tracking bandwidth, on the electro-hydraulic actuator are presented. After designing the QFT control system and experimental verification, the stability of the QFT controllers is investigated using T-S fuzzy modeling and its stability theory. This analysis is carried out in the presence of uncertainty in the parameters of the nonlinear model of electro-hydraulic actuator and the environment.

Chapter 6 describes the design of an output pressure controller for the electro-hydrostatic actuator. Again QFT is employed as the design approach. The family of frequency responses of the electro-hydrostatic actuator is obtained by applying an advanced form of fast Fourier transform on experimental inputs-outputs data. Using the family of frequency responses, a robust QFT controller is designed. Experimental results are also presented and the nonlinear stability of the designed QFT controller is investigated using T-S fuzzy modeling and its stability theory. This stability analysis is carried out in the presence of uncertainty in the parameters of the system, environment, friction, and external and internal leakages. The contributions of this research are given in Chapter 7, along with suggestions for future research.

Chapter 2

Hydraulic Actuation Systems

The double-rod hydraulic actuator in the experimental set-up of this research can be controlled by two actuation systems: electro-hydraulic and electro-hydrostatic, shown in Figure 2.1. In the following sections, components, circuits, and functionality of both the electro-hydraulic and electro-hydrostatic actuation systems are described. In addition, the nonlinear models of these actuation systems are presented.

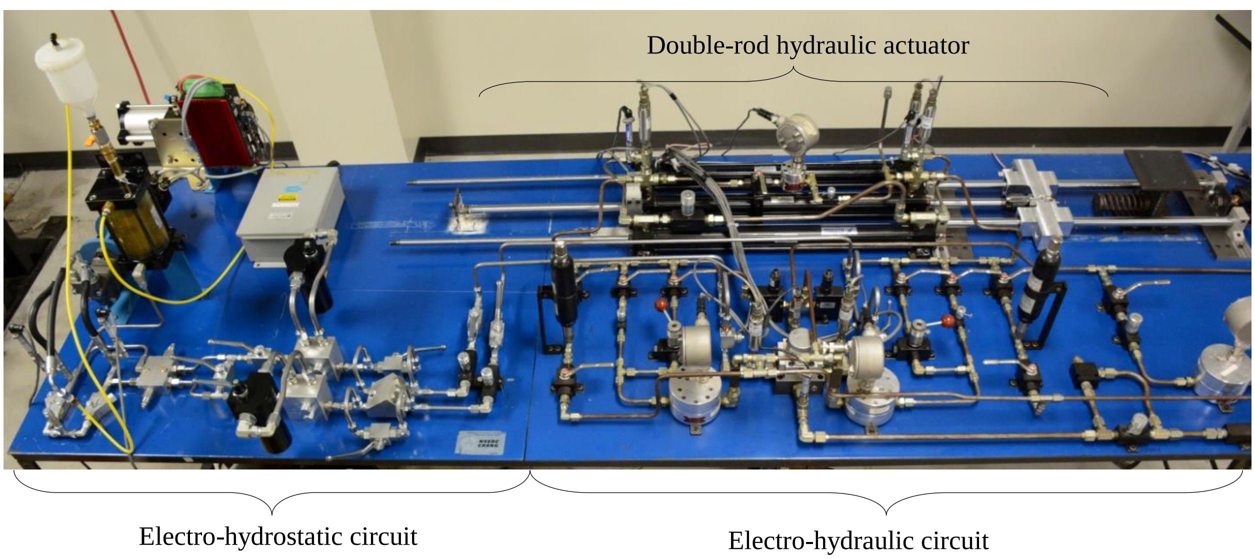

Figure 2.1. Experimental set-up: electro-hydraulic circuit (right), electro-hydrostatic circuit (left).

2.1 Electro-Hydraulic Actuation

2.1.1 Test-Rig

The photograph and schematic diagram of the electro-hydraulic actuator are shown in Figure 2.2. The main components of this system are the double-rod actuator, a servovalve and a high pressure supply, also known as hydraulic power supply. The double rod hydraulic actuator is a heavy-duty actuator, manufactured by Parker, and has a 38.1 mm bore, annulus area of 633 mm^2, and a 610 mm stroke. The fluid flow is controlled by D765, a nozzle-flapper servovalve manufactured by Moog with a 31 L/min (8.3 GPM) flow capacity at 17.2 MPa (2500 psi) supply pressure, and a rise time of 2 msec.

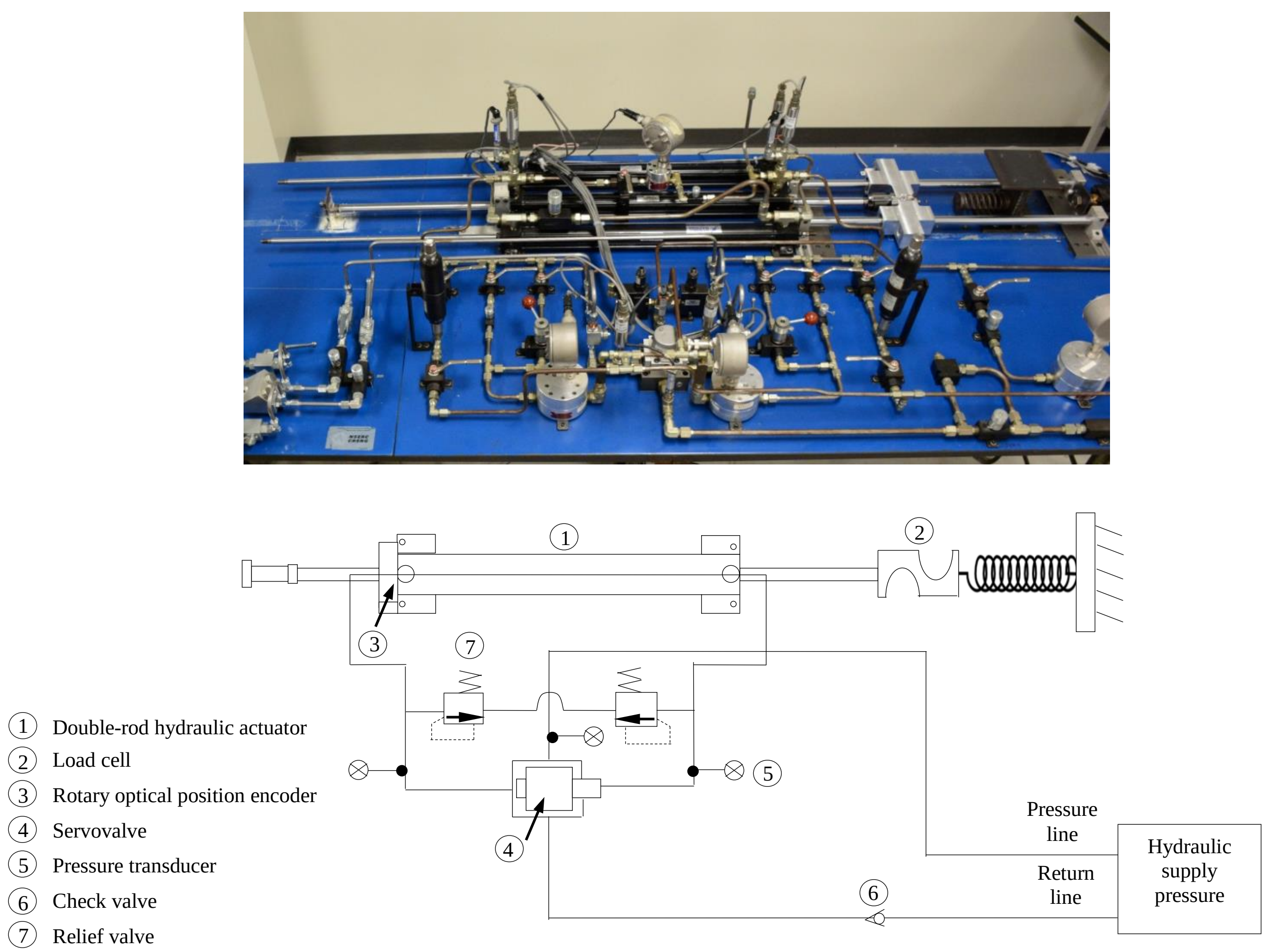

Figure 2.2. Electro-hydraulic actuator, test-bed and schematic.

The D765 uses a linear variable differential transformer (LVDT) that measures the position of the spool. Using a closed-loop position control system in the servovalve, an accurate position control of the spool to the command signal becomes possible. The pressures of the fluid in the supply and the return ports of the servovalve are measured by two Ashcroft-K1 pressure transducers with a 0-21 MPa range and a full-scale accuracy of ±0.5%. To measure the pressure at the control port of the servovalve, two Sensotech-FPG pressure transducers with a range of 0-21 MPa and a full-scale accuracy of ±0.1% are placed. Since fluid pressure drops as a result of piping between the servovalve and the actuator chambers, another pair of Sensotech-FPG pressure transducers is installed directly for the chambers. The actuator displacement is measured by a rotary encoder (Bourns ENS1J-B28) with a resolution of 1024 counts/revolution. Maximum displacement is 0.6 m which is the length of the rod. The system consists of a fluid reservoir, to keep the hydraulic fluid at a low pressure and use as needed. The hydraulic power supply is a variable displacement pump with the nominal pressure between 17 and 21 MPa (2500 to 3000 psi). The nominal supply pressure can be set by adjusting a pressure relief valve. The experimental hardware is interfaced to a desktop computer by a DAS16F input–output board and a M5312 24-bit quadrature incremental encoder card. The desktop computer runs the Windows XP operating system. DAS16F input–output board digitizes the analog signal and apply the software generated control signal to the servovalve. The nominal sampling rate of the interface and control software is approximately 1 kHz.

2.1.2 Modeling

A schematic diagram and the system variables of the electro-hydraulic actuator interacting with the environment are shown in Figure 2.3. The control signal activates the servovalve spool to move. The following first-order dynamic equation represents the relationship between the control signal u_v and the spool displacement x_v (Alleyne and Liu, 2000; Liu and Alleyne, 2000; Niksefat and Sepehri, 2001):

$$\dot{x}_v = \frac{-1}{\tau} x_v + \frac{k_{sp}}{\tau} u_v \tag{2.1}$$

where k_{sp} is the gain and τ is the time constant of the servovalve. Spool displacement changes the fluid flows at the servovalve control ports according to the following equations:

$$Q_1 = K_v w x_v \sqrt{\frac{P_s - P_r}{2} + \mathrm{sgn}(x_v)(\frac{P_s + P_r}{2} - P_1)} \tag{2.2a}$$

$$Q_2 = K_v w x_v \sqrt{\frac{P_s - P_r}{2} + \mathrm{sgn}(x_v)(P_2 - \frac{P_s + P_r}{2})} \tag{2.2b}$$

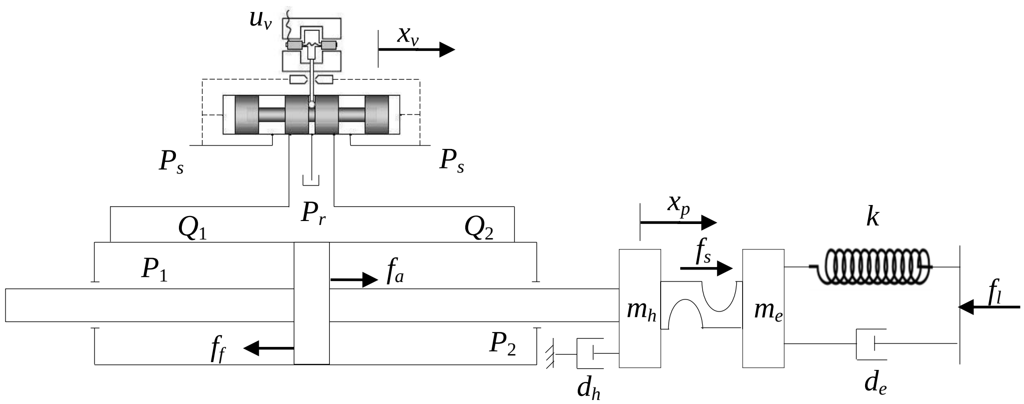

Figure 2.3. Variables in electro-hydraulic actuator.

where P_s and P_r are the hydraulic supply and return pressures, respectively. In equation (2.2) constant $K_v = \sqrt{2} C_d \rho^{-0.5}$ is the flow coefficient, w is the orifice area gradient, C_d is the coefficient of the discharge and ρ is the hydraulic fluid density. The input and output flows in turn change the pressures in each of actuator chambers as follows:

$$\dot{P}_1 = \frac{\beta}{V_1}(Q_1 - k_i(P_1 - P_2) - k_e P_1 - A v_p) \tag{2.3a}$$

$$\dot{P}_2 = \frac{\beta}{V_2}(-Q_2 + k_i(P_1 - P_2) - k_e P_2 + A v_p) \tag{2.3b}$$

where v_p is the actuator velocity, β is the effective bulk modulus of the hydraulic fluid, and A refers to the piston effective area. k_i is the actuator internal (cross-port) leakage coefficient and k_e is the actuator external leakage coefficient. The volume of the hydraulic oil in each side of the piston is given by variables V_1 and V_2 as follows:

$$V_1 = V_{01} + A x_p \tag{2.4a}$$

$$V_2 = V_{02} - A x_p \tag{2.4b}$$

where V_{01} and V_{02} are the initial volume of the fluid in each side of the actuator. In double-rod hydraulic actuators, the pressure differential P_1-P_2 multiplied by the piston effective area A determines the actuator force, $f_a=A(P_1-P_2)$. This force accelerates the actuator itself and deals with friction force acting between the piston and the cylinder walls, f_f, and linear viscous friction $d_h v_p$, where d_h is the viscous damping coefficient of the hydraulic fluid. The rest of the actuator force is applied on the environment and deals with the external force f_l. The mentioned force is shown by f_s in Figure 2.3 and can be measured by a force sensor. Assuming a high stiffness for the force sensor as compared with the stiffness of the environment and the actuator, the dynamic equations are:

$$m_h \ddot{x}_p = f_a - d_h v_p - f_s - f_f \tag{2.5}$$

$$m_e \ddot{x}_p = f_s - d_e v_p - k x_p - f_l \tag{2.6}$$

where the total mass of the piston and rod of the actuator is shown by m_h; the environment is represented by mass m_e, damping d_e and stiffness k. Now, the entire nonlinear model of the double-rod electro-hydraulic actuator based on equations (2.1)-(2.6) are written as follows:

$$\dot{x}_p = v_p \tag{2.7a}$$

$$\dot{v}_p = \frac{1}{m}(A(P_1 - P_2) - kx_p - dv_p - f_d) \tag{2.7b}$$

$$\dot{P}_1 = \frac{\beta}{V_{01} + Ax_p}(K_v w x_v \sqrt{\frac{P_s - P_r}{2} + \mathrm{sgn}(x_v)(\frac{P_s + P_r}{2} - P_1)} - k_i(P_1 - P_2) - k_e P_1 - Av_p) \tag{2.7c}$$

$$\dot{P}_2 = \frac{\beta}{V_{02} - Ax_p}(-K_v w x_v \sqrt{\frac{P_s - P_r}{2} + \mathrm{sgn}(x_v)(P_2 - \frac{P_s + P_r}{2})} + k_i(P_1 - P_2) - k_e P_2 + Av_p) \tag{2.7d}$$

$$\dot{x}_v = \frac{-1}{\tau} x_v + \frac{k_{sp}}{\tau} u_v \tag{2.7e}$$

where $m=m_h+m_e$ represents combined mass of the piston, rod, and environment, $d=d_h+d_e$ represents the total damping coefficient of the electro-hydraulic actuator consisting of the actuator viscous damping and the damping of environment. f_d is the combination of friction f_f and external force f_l; $f_d = f_f + f_l$. For friction f_f, a LuGre model is considered. This model has been developed based on the modeling of sliding surfaces with elastic bristles which separate and bond (Tran et al., 2012). When two surfaces are sliding, the bristles are deformed with deflection of η. The rate of this deflection is represented by a spring-like behaviour as follows:

$$\frac{d\eta}{dt} = v_p - \sigma_0 \psi(v_p)\eta \tag{2.8}$$

where, σ_0, is the average stiffness of bristles and $\psi(v_p)$ is the following nonlinear term:

$$\psi(v_p) = \frac{|v_p|}{F_c + (F_s - F_c)e^{-|v_p / v_s|^{\alpha_f}}} \tag{2.9}$$

In the above equation, F_s corresponds to the stiction force; F_c is the Coulomb friction force; α_f is a geometry dependent parameter, and v_s is called Stribeck velocity. The friction force f_f is determined by the following equation:

$$f_f = \sigma_0 \eta + \sigma_1 \dot{\eta} = \sigma_1 v_p + \left(\sigma_0 - \sigma_1 \sigma_0 \psi(v_p)\right)\eta \tag{2.10}$$

In equation (2.10), parameter σ_1 is the micro damping coefficient. Note that the effect of viscous friction has already been incorporated into the system model as dv_p, and therefore is not considered in (2.10). The parameters of friction model were identified according to the procedure outlined in (Tran et al., 2012) and given in Table 2.1. The nominal values and the variation range of other parameters of the system are given in Table 2.1. These values were obtained from manufacturer's catalogs and earlier reported investigations (Karpenko and Sepehri, 2008; 2009; 2012). In this table, the valve flow gain k_s and flow pressure coefficient k_p are related to the linearized model of the electro-hydraulic actuator which will be explained in Chapter 5.

Table 2.1. Values of parameters of electro-hydraulic actuation system.

Parameter	Nominal Value	Range
Supply pressure, P_s (MPa)	17.2	-
Spring stiffness, k (kN/m)	90	70-130
Total mass, m (kg)	12.3	10-14
Total damping coefficient, d (N.sec/m)	250	200-400
Piston area, A (m^2)	6.33×10^{-4}	-
Chambers initial volume, V_{01} and V_{02} (m^3)	234×10^{-6}	-
Servovalve time constant, τ (sec)	0.0022	0.002-0.0026
Valve orifice area gradient, w (m^2/m)	0.02075	-
Spool valve position gain, k_{sp} (μm/V)	25	23.1-27
Fluid bulk modulus, β (MPa)	689	650-700
Flow coefficient, K_v ($m^{3/2}/kg^{1/2}$)	0.0292	-
Valve flow gain, k_s (m^2/sec)	1.5	1.34-1.73
Flow pressure coefficients, k_p (m^3/sec/Pa)	0	$0\text{-}1.09\times10^{-11}$
Stribeck velocity, v_s (m/sec)	0.01	-
Coulomb friction F_c (N)	75	-
Stiction friction F_s (N)	240	-
Average stiffness of bristles σ_0 (N/m)	1.04×10^{9}	-
Friction geometry parameter α_f	1	-
Micro damping coefficient σ_1 (N.sec/m)	100	-

2.2 Electro-Hydrostatic Actuation

2.2.1 Test-Rig

A schematic diagram of the electro-hydrostatic actuator of this research is shown in Figure 2.4. The main components of this system are the double-rod hydraulic actuator, a fixed-displacement pump and a variable speed electric servomotor. The double-rod actuator is the same actuator discussed in Section 2.1.1. The features of other component and the system functioning are presented as follows.

The fixed-displacement hydraulic pump that has been used in this experimental set-up is a F11-005-HU-CV-K-000-000-0 from Parker, with the maximum speed of 4000 rpm clockwise and counter clockwise. The pump provides a constant flow rate in each cycle. This pump has fixed-displacement of 4.9 cm^3/rev, and a maximum limit of pressure rated at 5000 psi. Referring to

Figure 2.4, the leakage from the pump case drain goes to reservoir 1 which is manually connected to the pressurized reservoir 2 before an experiment starts. Reservoir 2 is pressurized by 120 psi using an air booster to avoid cavitation in the system. Two pressure transducers are also connected to the inlet and the outlet of the pump. The pump is coupled to the servomotor by a flexible Oldham coupler to synchronize the rotation of the pump and the servomotor, shown in Figure 2.5.

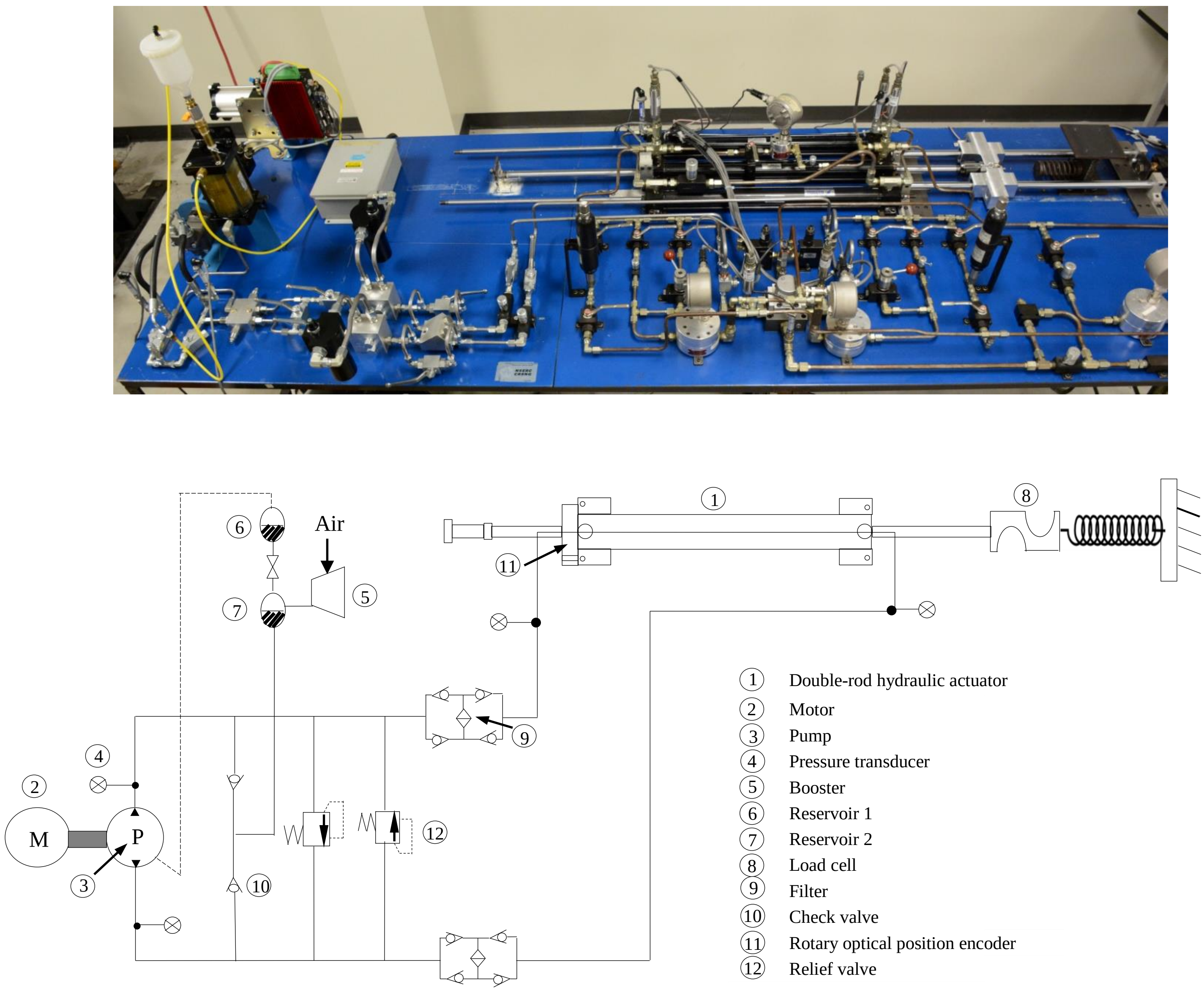

Figure 2.4. Electro-hydrostatic actuator, test-bed and schematic.

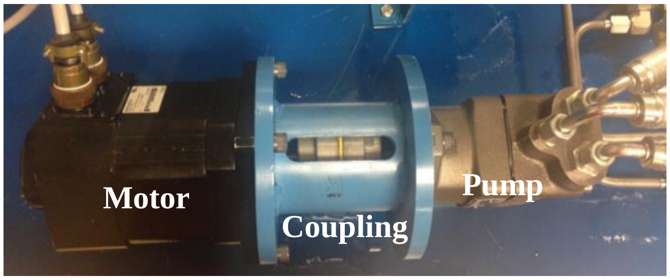

Figure 2.5. Coupling between fixed-displacement pump and servomotor.

The servomotor in the experimental set-up is M-4650 made by Teknic, a permanent magnet rotary servomotor which is assisted by a sealed, high bandwidth, and precise differential encoder to measure the position of the servomotor. Since the encoder has a unique floating mount design, if the axial shaft moves slightly, the encoder moves with the servomotor shaft. The servomotor is connected to the servodrive SSt-6000-R which is interfaced to a high speed computer using an I/O board. The I/O board receives the pressure data from sensors installed in the actuator chambers and the pump inlet and outlet, as well as data from encoders that measure the actuator displacement and the servomotor position. The measured data by sensors and encoders are then available in the high speed computer for control purposes. In the high-speed computer, the pressure controllers are implemented in Simulink environment. In order to control the output pressure, the velocity of the electric motor is controlled. Corresponding to the command signal sent from the high-speed computer to the servodrive, it generates a PWM signal to run the servomotor. When the servomotor is running, based on the data sent by the attached encoder to the servomotor, the actual velocity of the servomotor is calculated. In servodrive, the actual velocity and the desired velocity are compared. Based on the velocity error, an internal control system in the servodrive generates a new signal to apply to the servomotor. This continues until velocity of the servomotor reaches the desired velocity. The servodrive internal controller consists of a PIV controller with dual feedforward terms, which provides a high performance tracking system with a settling time less than 1 msec. The servodrive utilizes an adaptive control algorithm called inverse modeling technique (IMT) based on neural fuzzy logic to enhance the robustness of the control system. The above features in servodrive have been digitally implemented in non-volatile EEPROM, and are accessible through a Windows based software, called Quickset, developed by Teknic. This software is used to configure and diagnose the servodrive. The sampling rate at which the data is collected is 1 kHz.

2.2.2 Modeling

In Figure 2.6, the schematic and system variables of the electro-hydrostatic actuator under study are shown. In the electro-hydrostatic actuator, the control signal u_m runs the servomotor to reach the velocity of ω_m according to the following first order differential equation:

$$\dot{\omega}_m = \frac{-1}{\tau_m}\omega_m + \frac{k_m}{\tau_m}u_m \tag{2.11}$$

where k_m is the servomotor gain, and τ_m is the servomotor time constant. Since, the servomotor and the pump are coupled together, by rotation of the servomotor, accordingly, pump rotates and generates the flows according to the following equations:

$$Q_U = D_p\omega_p - \frac{V_U}{\beta}\frac{dP_U}{dt} - C_{ip}(P_U - P_D) - C_{ep}P_U \tag{2.12a}$$

$$Q_D = D_p\omega_p + \frac{V_D}{\beta}\frac{dP_D}{dt} - C_{ip}(P_U - P_D) + C_{ep}P_D \tag{2.12b}$$

where Q_U and Q_D are the flow coming out and going into the pump, and P_U and P_D are the pressures at the outlet and inlet of the pump.

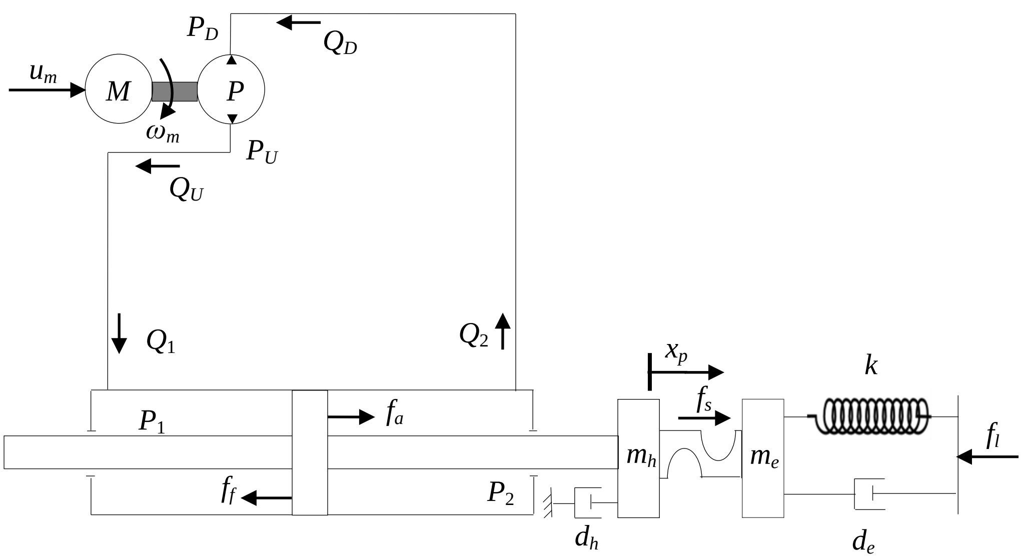

Figure 2.6. Variables in electro-hydrostatic actuator.

In equation (2.12), D_p is the pump displacement, ω_p is the pump angular velocity which is equal to servomotor angular velocity; $\omega_p = \omega_m$, C_{ep} is the external leakage coefficient of the pump, and C_{ip} is the pump cross-port leakage coefficient. V_U and V_D are the pump section volume associated with its outlet and inlet ports respectively.

The inlet and outlet of the pump are connected to the actuator chambers via some pipes which cause pressure drop. As a result, the relationship between pressures in the pump side and the actuator side are as follows:

$$P_1 = P_U - P_{pipe} \tag{2.13a}$$

$$P_2 = P_D + P_{pipe} \tag{2.13b}$$

where P_1 and P_2 are the pressures in the actuator chambers, and P_{pipe} shows the pressure drop across the pipes. From Figure 2.6, having no leak across the pipes, $Q_U=Q_1$ and $Q_D=Q_2$. The relationship between the flows and the pressures at the cylinder side are as follows:

$$Q_1 = Av_p + \frac{V_{01} + Ax}{\beta}\frac{dP_1}{dt} + k_e P_1 + k_i P_L \tag{2.14a}$$

$$Q_2 = Av_p - \frac{V_{02} - Ax}{\beta}\frac{dP_2}{dt} - k_e P_2 + k_i P_L \tag{2.14b}$$

where v_p is the actuator velocity. A refers to the piston effective area, β is the effective bulk modulus of the hydraulic fluid, k_i is the actuator internal leakage coefficient, and k_e is the actuator external leakage coefficient. V_{01} and V_{02} are the initial volumes of the oil in each side of the actuator. The pressure differential $P_1 - P_2$ acting on the piston effective area A generates the actuator force f_a:

$$f_a = (P_1 - P_2)A \tag{2.15}$$

The differential pressure P_1-P_2 is called the output pressure of the system and is shown by P_L. Resultant actuator force f_a accelerates the actuator itself and deals with force acting between the piston and the cylinder walls due to friction, f_f, and linear viscous friction $d_h v_p$, where d_h is the viscous damping of the hydraulic fluid. The rest of the actuator force is shown by f_s in Figure 2.6, is referred as the interacting force. This force manipulates the environment and deals with the external force f_l. The interacting force f_s is measurable by a force sensor. In Figure 2.6, the environment is modeled as a mass (m_e)-spring (k)-damper (d_e), and the actuator mass is shown by m_h. Assuming a high stiffness for the force sensor as compared with the stiffness of the environment and the actuator, the dynamic equation is as follows:

$$m\ddot{x}_p = f_a - kx_p - dv_p - f_l - f_f \tag{2.16}$$

where $m=m_h+m_e$ represents combined mass of the piston, rod, and environment, $d=d_h+d_e$ represents total damping coefficient and consists of the actuator viscous damping and the damping of environment. The nominal values of the system parameters are given in Table 2.2 using manufacturer's catalogs and earlier reported investigations (Karpenko and Sepehri, 2008; 2009; 2012). The friction model and corresponding parameters are same as in Section 2.1.2.

Table 2.2. Values of parameters of electro-hydrostatic actuation system.

Parameter	Nominal Value
Servomotor gain, k_m (rad/V.sec)	25
Servomotor time constant, τ_m (sec)	0.001
Spring stiffness, k (kN/m)	90
Total mass, m (kg)	12.3
Total damping coefficient, d (N.sec/m)	250
Fluid bulk modulus, β (MPa)	689
Fixed pump displacement, D_p (m^3/rev)	4.9×10^{-6}
Piston area, A (m^2)	6.33×10^{-4}
Total volume of the cylinder, V_{01}, V_{02} (m^3)	234×10^{-6}

2.3 Summary

In this chapter, features and functionality of electro-hydraulic and electro-hydrostatic actuation systems were described. Mathematical models of the actuation systems and their corresponding parameter values were presented. These models will be used in subsequent chapters for the design of robust output pressure controller and also nonlinear stability analysis of the control systems.

Chapter 3

Quantitative Feedback Theory

This chapter presents an overview of the quantitative feedback theory (QFT). Based on this theory, the designed controller guarantees robust performance and stability within a certain range of inputs-outputs of the system. The classical two-degree-of-freedom QFT feedback control system is presented, followed by the description of design steps in QFT. QFT design technique is used in the subsequent chapters to design robust output pressure controllers for electro-hydraulic and electro-hydrostatic actuators.

3.1 Control Block Diagram

Figure 3.1 illustrates the two-degree-of-freedom feedback structure that is used in QFT design technique. Note that here, two-degree-of-freedom means the presence of two measurable quantities, *R* and *Y*. In this thesis, no measurement is carried out on disturbance *D* (Yaniv, 1999).

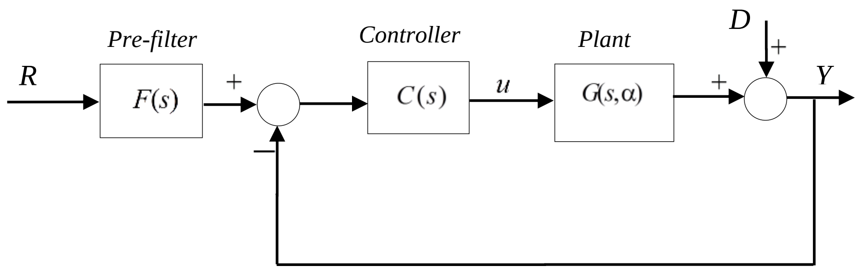

Figure 3.1. Two degree-of-freedom QFT control system.

In QFT design technique, a family of frequency responses of the uncertain nonlinear plant is required. These frequency responses can be obtained through different methods that will be explained in Section 3.2.1. In the control system shown in Figure 3.1, this family of frequency responses is obtained using the following transfer function:

$$G(s,\alpha)=\frac{\sum_{n=0}^{N} p_n(\alpha)s^n}{\sum_{m=0}^{M} q_m(\alpha)s^m} \tag{3.1}$$

where $\alpha \in \Omega \subset R^{\rho}$ is a vector of ρ uncertain parameters of the system. Ω is a compact set of parameter variations, given as:

$$\Omega=\{\alpha:\alpha_i \in [\alpha_1 \quad \alpha_2], i=1,...,\rho\} \tag{3.2}$$

Each uncertain parameter $\alpha_i (i=1,...,\rho)$ varies independently within an interval (Niksefat and Sepehri, 2001). In control structure in Figure 3.1, the desired response is shown by *R*. Employing QFT design technique, the controller *C*(*s*) and the pre-filter *F*(*s*) must be designed such that the output of the control system, i.e., *Y* follows the desired command *R* within some given tolerance despite uncertainty in the parameters of the system and nonidealities. The nonidealities include measurement noise, unmodeled dynamics, and disturbance in the control system. In QFT, the controller and the pre-filter are designed in the frequency domain. The controller is designed through a loop-shaping process in the Nichols chart, and the pre-filter is designed using the Bode diagram. Therefore, all desired specifications should be represented as constraints in frequency domain. Then the constraints are demonstrated as bounds on the loop transmission function in the Nichols chart. This way QFT provides a quantitative relationship between desired specifications, and system uncertainties and nonidealities. The graphical representation of the design constraints in the Nichols chart helps the designer to make a better decision on the complexity of the controller in order to satisfy the performance criteria.

3.2 Design Steps

In this section, steps for designing QFT controllers and pre-filters for plants with parametric uncertainties are explained in detail. These steps are generating templates, calculating bounds, loop-shaping, and pre-filter design.

3.2.1 Generating Plant Templates

The first step is to present the family of frequency responses of the uncertain nonlinear plant in the Nichols chart. These frequency responses can be obtained via different methods including small-signal (Niksefat and Sepehri, 2001), Fourier transformation (Karpenko and Sepehri, 2008), and Golubev (Golubev and Horowitz, 1982). To derive the frequency responses, a number of techniques such as small-signal method require a mathematical model of the plant, which is linearized around the operating points of interest. Other techniques such as Fourier transformation and Golubev are applied on the sets of input-output data of the system, which are obtained in certain operating conditions. Therefore, the derived frequency responses represent the original nonlinear plant within a certain input-output set or around some operating points.

Then the magnitude and phase of the family of frequency response are plotted in the Nichols chart for a finite number of frequencies, known as the array of design frequencies (Borghesani et al. 2003). In general, the frequencies where the shape of the template shows significant variations should be considered in this array (Borghesani et al. 2003). At each frequency of this array the phase and the magnitude of the family of frequency response are marked. For example for the system in Figure 3.1, the magnitude and phase of the plant, i.e. $G(s,\alpha)$ are calculated for the whole combination of the parameters variation and then marked in the Nichols chart. The region in the Nichols chart that is covered by the data points of the family of frequency response in a particular frequency is called the plant template in that frequency. The templates are used to generate bounds on the Nichols chart for the controller design. It is required choosing one arbitrary frequency response corresponding to a specific vector of uncertain parameters, α_0. The plant designated to this set of parameter values is called the nominal plant, i.e., $G_0(j\omega,\alpha_0)$. The corresponding loop transfer function is also called nominal loop transfer (or transmission) function, i.e., $L_0(j\omega) = C(j\omega)G_0(j\omega, \alpha_0)$, where $L(j\omega)$ is the loop transmission function, $L(j\omega) = C(j\omega)G(j\omega, \alpha)$. The nominal plant is used to calculate the QFT bounds in the next section, and the nominal loop is used to design the QFT controller.

3.2.2 Design Specifications in Frequency Domain

Representation of the performance criteria in the frequency domain is as follows:

i) For the stability of the closed-loop system and noise rejection (Guzman et al., 2011), the following constraint on the complementary sensitivity function must be satisfied for the entire range of parameters uncertainties:

$$|T(j\omega)| = \left|\frac{L(j\omega)}{1+L(j\omega)}\right| \le M_t \ \ \forall\omega \in [0\ \infty) \tag{3.3}$$

If M_t is a constant, it guarantees the following amount of gain margin and phase margin for the closed-loop system (Yaniv, 1999):

$$GM = 20\log_{10}\left\{\frac{M_t+1}{M_t}\right\} \text{dB} \tag{3.4}$$

$$PM = 2\sin^{-1}\left\{\frac{1}{2M_t}\right\} \text{deg} \tag{3.5}$$

However guaranteed gain and phase margins, do not imply a good robust stability margin (Levine, 1996). Robust stability margin is determined by the inverse of the shortest distance between the Nyquist plot of the loop transmission function from the critical point (-1,0), i.e., $|1+L(j\omega)|$. Robust stability margin also appears in the peak of the magnitude of the sensitivity transfer function, i.e., $\max(|S(j\omega)|=1/|1+L(j\omega)|)$. Therefore, to guarantee the robust stability margin, in the next section, an appropriate upper bound on the sensitivity magnitude is imposed.

ii) To attenuate the effect of disturbance D on the output, and guarantee robust stability, the following constraint on sensitivity function must be satisfied for the entire range of parameters variation:

$$|S(j\omega)| = \left|\frac{Y}{D}\right| = \left|\frac{1}{1+L(j\omega)}\right| \le M_s \ \ \forall\omega \in [0\ \infty) \tag{3.6}$$

The complementary sensitivity and sensitivity transfer functions in a closed-loop system satisfy the following equation (Levine, 1996):

$$T(j\omega) + S(j\omega) = 1 \tag{3.7}$$

From the above equation and equations (3.3) and (3.6), the following constraint on the upper bound of the complementary sensitivity function, i.e., M_t and the upper bound of the sensitivity function. i.e. M_s is derived (Levine, 1996):

$$M_t + M_s \ge 1 \tag{3.8}$$

Constraint (3.8) indicates that sensitivity and complementary sensitivity functions cannot be small (less than 1) at the same frequency. In control systems, measurement noise becomes large at high frequencies, while disturbances appear at low frequencies. Therefore, a reasonable selection is firstly, to keep the sensitivity function as low as possible at low frequencies. Selection of M_s <<1, results in $M_t \approx 1$, or $|L(j\omega)| >> 1$, which also implies good reference tracking. Secondly, the complementary sensitivity function must be kept as low as possible at high frequencies to reject noises. Selection of M_t<<1 results in $M_s \approx 1$ or $|L(j\omega)| << 1$. At intermediate frequencies both the sensitivity and the complementary sensitivity functions must be prevented from being excessively large. Having M_s>>1 or M_t>>1, implies that $|L(j\omega)| \approx 1$ and $\angle L(j\omega) \approx \pm 180^\circ$, and the system will be on the verge of instability (Levine, 1996). For strictly proper systems, the following equation holds:

$$\lim_{\omega\to\infty} C(j\omega)G(j\omega) = 0 \tag{3.9}$$

Thus:

$$\lim_{\omega\to\infty} |T(j\omega)| = \left|\frac{C(j\omega)G(j\omega)}{1+C(j\omega)G(j\omega)}\right| = 0 \tag{3.10a}$$

$$\lim_{\omega\to\infty} |S(j\omega)| = \left|\frac{1}{1+C(j\omega)G(j\omega)}\right| = 1 \tag{3.10b}$$

Equation (3.10a) shows that the complementary sensitivity transfer function has a low magnitude at high frequencies that is desirable in order to reject noise that happens at high frequencies.

Equation (3.10b) shows that the sensitivity has higher magnitude at high frequencies. For strictly proper systems, there is another important equation about sensitivity called Bode sensitivity integral, or waterbed effect as follows (Houpis et al., 2005):

$$\int_0^{\infty} \ln\left|S(j\omega)\right| d\omega = 0 \tag{3.11}$$

Equation (3.10) implies the fact that if the sensitivity is close to one at high frequencies, it becomes close to zero at low frequencies. From equations (3.10b) and (3.11), the sensitivity is low at low frequencies, which is desirable to reject disturbances that normally happen at low frequencies.

Therefore, the constant upper bounds on the magnitudes of the complementary sensitivity, $T(j\omega)$ and sensitivity $S(j\omega)$ are mostly effective for intermediate frequencies. According to Astrom (2002), to impose constant upper bounds on the magnitude of the complementary sensitivity and sensitivity transfer functions through whole range of frequencies, the constant must be chosen between 1 and 2.

iii) For the tracking of the desired command, the following constraint must be satisfied for the entire range of parameters variation.

$$\left|T_l(j\omega)\right| \le \left|F(j\omega)\frac{L(j\omega)}{1+L(j\omega)}\right| \le \left|T_u(j\omega)\right| \quad \forall\omega \in \left[0 \quad \infty\right) \tag{3.12}$$

where the upper and lower bounds $T_u(j\omega)$ and $T_l(j\omega)$ are determined by the designer. The shape of these bounds determines the transient response of the system and the closed-loop bandwidth. It is important to mention that satisfying the tracking constraint is done in two steps. The first step is done in the Nichols chart, where only the controller is designed. Towards this step, a constraint which only includes the controller and can be graphically represented in the Nichols chart is derived from the inequality (3.12) as follows:

$$20\log_{10}|T_l(j\omega)| \le 20\log_{10}\left|\frac{F(j\omega)L(j\omega)}{1+L(j\omega)}\right| \le 20\log_{10}|T_u(j\omega)|$$

$$\Rightarrow \begin{cases} 20\log_{10}\left|\frac{F(j\omega)L(j\omega)}{1+L(j\omega)}\right| \le 20\log_{10}|T_u(j\omega)| \Rightarrow 20\log_{10} F(j\omega) + 20\log_{10}\left|\frac{L(j\omega)}{1+L(j\omega)}\right|_{\max} \le 20\log_{10}|T_u(j\omega)| \\ -20\log_{10}\left|\frac{F(j\omega)L(j\omega)}{1+L(j\omega)}\right| \le -20\log_{10}|T_l(j\omega)| \Rightarrow -(20\log_{10} F(j\omega) + 20\log_{10}\left|\frac{L(j\omega)}{1+L(j\omega)}\right|_{\min}) \le -20\log_{10}|T_l(j\omega)| \end{cases}$$

Adding the two inequalities on the left results in the following formula:

$$20\log_{10} F(j\omega) + 20\log_{10}\left|\frac{L(j\omega)}{1+L(j\omega)}\right|_{\max} - (20\log_{10} F(j\omega) + 20\log_{10}\left|\frac{L(j\omega)}{1+L(j\omega)}\right|_{\min}) \le 20\log_{10}|T_u(j\omega)| - 20\log_{10}|T_l(j\omega)|$$

From the above inequality, the following relationship is derived, which relates the uncertainty in the plant to the tracking bounds and includes only the controller and not the pre-filter.

$$20\log_{10}\left|\frac{L(j\omega)}{1+L(j\omega)}\right|_{\max} - 20\log_{10}\left|\frac{L(j\omega)}{1+L(j\omega)}\right|_{\min} \le 20\log_{10}|T_u(j\omega)| - 20\log_{10}|T_l(j\omega)| \qquad (3.13)$$

The above inequality is used to generate the tracking bounds in the Nichols chart. Still the pre-filter must be designed to satisfy inequalities 3.14 and 3.15. These two inequalities are another representation of the constraint (3.12).

$$20\log_{10}|F(j\omega)| + 20\log_{10}\left|\frac{L(j\omega)}{1+L(j\omega)}\right|_{\max} \le 20\log_{10}|T_u(j\omega)| \qquad (3.14)$$

$$20\log_{10}|F(j\omega)| + 20\log_{10}\left|\frac{L(j\omega)}{1+L(j\omega)}\right|_{\min} \ge 20\log_{10}|T_l(j\omega)| \qquad (3.15)$$

3.2.3 Generating Bounds and Loop-Shaping

The performance constraints consisting of stability, tracking, and disturbance rejection should be graphically represented in the Nichols chart. These bounds are derived by moving the plant templates between the closed-loop magnitude contours on the Nichols chart. These bounds are used in loop-shaping as a guide for shaping the nominal loop transmission function.

Finally, once the QFT bounds are derived, the nominal loop transmission function, $L_0(j\omega) = C(j\omega)G_0(j\omega, \alpha_0)$, should be designed by adding proper poles and zeroes to the controller $C(j\omega)$, to satisfy all bounds while it should not cross the axis of positive magnitude at -180° (instability region in the Nichols chart). A typical plot of $L_0(j\omega)$ is given in Figure 3.2. This means that the nominal loop transmission function must stay close to the bounds and its magnitude must decrease rapidly as frequency increases. The requirement of low bandwidth in the controller is to avoid problems with amplification of noise and unmodeled dynamics.

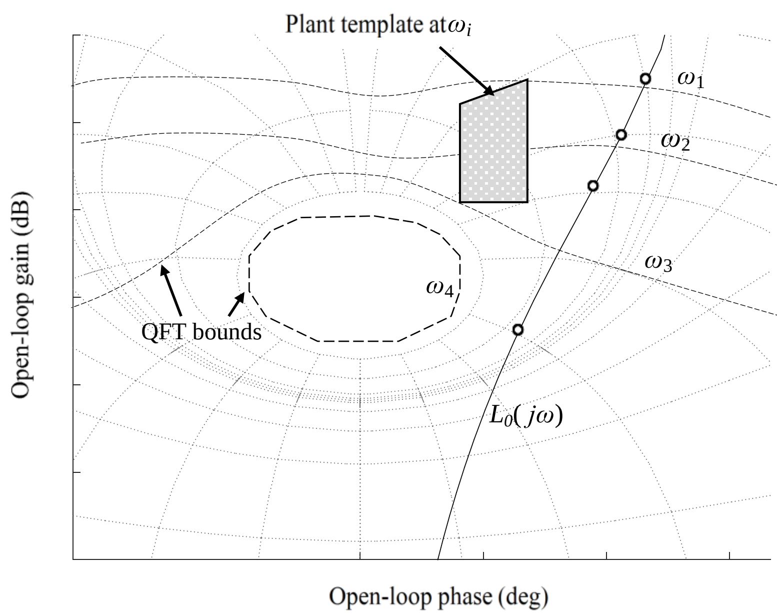

Figure 3.2. Plant template, QFT bounds, and Loop-shaping in Nichols chart.

3.2.4 Design of Pre-filter

Finally, if the tracking specifications are not satisfied, then a pre-filter $F(j\omega)$ is required to satisfy the inequalities (3.14) and (3.15), which can be designed in Bode diagram. Figure 3.3 shows the typical frequency responses of a system for the entire range of parametric uncertainties before and after a pre-filter is applied. Pre-filter moves frequency responses of system for the entire range of parametric uncertainties between the desired upper and lower bounds.

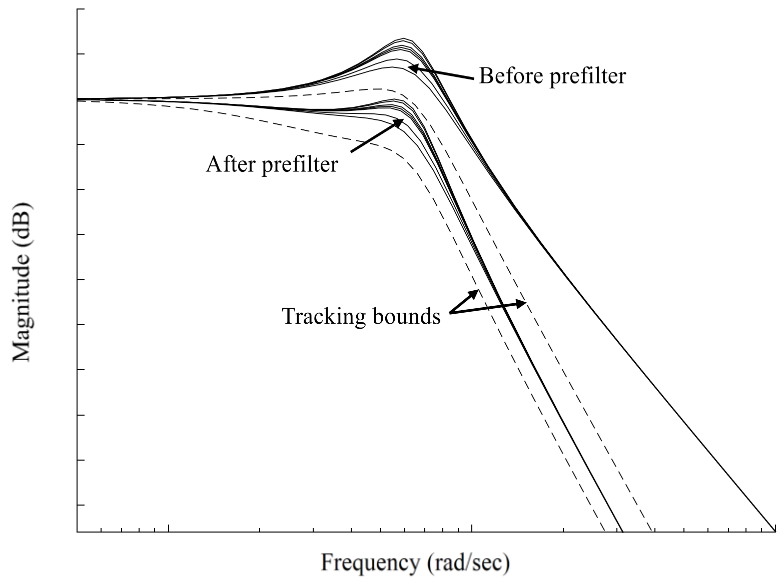

Figure 3.3. Frequency responses of closed-loop system before and after pre-filter.

3.3 Summary

The concept and design steps of QFT control systems were explained. It was shown how QFT provides a graphical relationship between desired specifications and system uncertainties. This helps the designer to make a better decision on the complexity of the controller. In Chapters 5 and 6, QFT design technique will be used to control the output pressure of the electro-hydraulic and electro-hydrostatic actuators under study.

Chapter 4

Stability Analysis Using T-S Fuzzy Modeling

As described in Chapter 3, QFT controllers are designed for the family of frequency responses of the nonlinear plant. These frequency responses are derived based on sets of input-output data obtained by running the plant in specified operating conditions, or linearizing the nonlinear plant around some operating points. As a result, the stability of the QFT control system is valid only over these particular sets of input-output and/or in a small-signal sense (Horowitz, 1976). Methods to solve the stability limitation of QFT control systems provide approximate stability results or suggest very conservative conditions on controller design (Barreiro and Banos, 2000; Banos et al., 2002). In this chapter a new solution based on Takagi-Sugeno (T-S) fuzzy modeling and its stability theory (Tanaka and Wang, 2001) is provided for the nonlinear stability analysis of QFT control systems, which provides the stability conditions in the form of linear matrix inequalities (LMIs) (Esfandiari and Sepehri, 2013). This solution overcomes the issues of the previous approaches, presented for QFT stability analysis. Review of fuzzy systems, T-S fuzzy modeling and corresponding stability theory are presented in Sections 4.1 and 4.2. In Section 4.3, a T-S fuzzy model describing the nonlinear functions of a double-rod electro-hydraulic actuator is derived. The effectiveness of the T-S fuzzy modeling and its stability theory for the nonlinear stability analysis of the control systems of hydraulic actuators is investigated by considering three case studies in Section 4.4. The first case study is a robust nonlinear controller previously designed based on the passivity theory for the pressure control of a hydraulic actuator (Alleyne and Liu, 2000). The second case study relates to a bilateral haptic control system of a hydraulic actuator, which was previously designed based on Lyapunov stability theory (Zarei-Nia and Sepehri, 2012). In the third case study, the T-S fuzzy modeling and its stability approach are employed to investigate the nonlinear stability of a QFT position controller for the first time. This QFT controller previously was designed for an electro-hydraulic actuator by Karpenko and Sepehri (2008).

4.1 Fuzzy Systems

A fuzzy system describes a nonlinear system based on fuzzy logic, where inputs are analyzed based on their degree of membership to defined fuzzy sets (a continuous value between zero and one), in contrast to classical logic, based on true or false, (a discrete value: zero or one). A fuzzy system consists of fuzzification, If-Then rules, inference process, aggregation, and defuzzification. Using a simple example, the functionality of each part in a fuzzy system is explained. The example is a two-input, one-output, three-rule fuzzy system to adjust the necessary time for irrigation of a garden. Inputs are the ambient temperature and soil moisture, and the output is a linguistic representation of the applied values to the lawn sprinkler system, which adjust how long the irrigation must be. The Following rules are defined to map inputs to outputs linguistically:

If ambient temperature is low And soil is wet, Then sprinkler works for a short time.

If temperature is high And soil is dry, Then, sprinkler works for a longer time.

If temperature is high And soil is moist, Then, sprinkler works for an average time.

In each rule, the part after If called antecedent, and the part after Then, is called conclusion. The values of temperature and moisture are measured by sensors, which are crisp values. Therefore, in the first step, these crisp values should be mapped to a relative fuzzy set through fuzzification process. The associated fuzzy values are the rating of a membership associated to a fuzzy set. For example, for the fuzzification of the ambient temperature t, three membership functions $\mu_l(t)$, $\mu_m(t)$, and $\mu_h(t)$ are defined. These three functions exemplify low, medium, and high temperatures, respectively (see Figure 4.1).

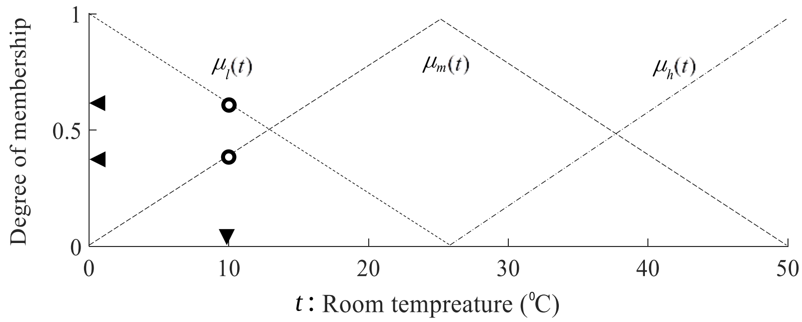

Figure 4.1. Fuzzy membership functions.

From Figure 4.1, the crisp temperature input of t=10˚C, belongs to the fuzzy set of low temperature with a grade of μ_l (10˚C)=0.6, belonging to the fuzzy set of medium temperature with a grade of μ_m(10˚C)=0.4, and belonging to the fuzzy set of high temperature with μ_h(10˚C)=0.

If the antecedent of a given rule engages more than one input using logical operations of And or Or, such as above example, a fuzzy operator should be applied to obtain one number that represents the result of the antecedent for that rule. Fuzzy operators are mathematical formulations that substitute And and Or in the antecedent part of a fuzzy rule. Two well-known operators for And are: min (minimum) and prod (product), and two well-known operators for Or are max (maximum) and probor (probabilistic), (Lee, 1990; Xu and Da, 2003). For the above example only And operator was used. Using the fuzzy operators, the result of the antecedent part of each rule is obtained as a single number.

The result of the antecedent of each rule is used to reshape the fuzzy set in the conclusion part of that rule. This process is called fuzzy inference. For inference, two well-known methods are employed: min (minimum), which truncates the output fuzzy set, and prod (product), which scales the output fuzzy set. The result of inference process for each rule is a fuzzy set corresponding to that rule (Lee, 1990; Xu and Da, 2003). These fuzzy sets which represent the results of rules for specific input values, must be combined into a single fuzzy set. This process is called aggregation. The final fuzzy set is converted to a crisp value through defuzzification process (Lee, 1990; Xu and Da, 2003). In this example the result of the defuzzification is the amount of time that the sprinkler must irrigate the garden.

In the above example, in both antecedent and conclusion parts of each rule, fuzzy sets were used. These types of fuzzy systems are called linguistic fuzzy systems. However, if fuzzy sets are only used in antecedent part and the conclusion consists of crisp (non-fuzzy) functions of input variables in antecedent, then it is called Takagi–Sugeno (T-S) fuzzy model. Due to the presence of linguistic variables in the first type of fuzzy systems, classical stability and design theories cannot be used. On the other hand, T-S fuzzy models employ crisp functions on the conclusion parts. Thus, a wide range of available tools in the area of classical control, stability, and identification can be utilized (Tanaka and Wang, 2001).

4.2 Takagi–Sugeno (T-S) Fuzzy Model

The concept of T-S fuzzy models was introduced by Takagi and Sugeno (1985). T-S fuzzy models can distribute the task of modeling and control of a nonlinear system into modeling and control of local linear systems, which are easier to handle (Tanaka and Wang, 2001). Ultimately, defuzzification process integrates the local tasks and yields the overall model. It has been proven that any nonlinear system can be represented by a T-S model with arbitrary accuracy (Tanaka and Wang, 2001). The stability of T-S fuzzy systems was first investigated by Tanaka and Sugeno (1992). The idea was to find a common quadratic Lyapunov function for all local models in a T-S fuzzy system. Searching for this common Lyapunov function was stated as a linear matrix inequality (LMI) problem. The resultant LMI constraints can be solved by convex optimization algorithms, available in software like MATLAB LMI Toolbox (Gahinet et al., 1995). In the following sections, construction and stability conditions of T-S fuzzy systems are described.

4.2.1 Construction of a T-S Fuzzy Model

In general there are two approaches for constructing T-S fuzzy models: (*i*) identification (fuzzy modeling) using input-output data and (*ii*) derivation from given nonlinear system equations, using sector nonlinearity approach. Using sector nonlinearity approach, a nonlinear system can be exactly represented by a T-S fuzzy model (Tanaka and Wang, 2001; Ohtake et al., 2003). The goal is to find a sector $[b_2 \quad b_1]x(t)$ to represent the nonlinear system $\dot{x}(t) = f(x(t))$ as

$[\mu_1 b_1 + \mu_2 b_2]x(t)$, where, $x(t)$ is the system state variable, $b_{i(i=1,2)}$ are scalars, and μ_1 and μ_2 are positive nonlinear membership functions such that $\sum_{i=1}^{2}\mu_i = 1$. As a result, the original nonlinear system $\dot{x}(t) = f(x(t))$ is represented as a weighted sum of local linear models, $b_1 x(t)$ and $b_2 x(t)$. Note that in general $x(t)$ can be a vector of system states, which in this case, $b_{i(i=1,2)}$ are matrices. Consider the following nonlinear system with one variable x:

$$\dot{x} = (3 + x^2)x, \quad x \in [-4 \quad 5] \tag{4.1}$$

Using T-S fuzzy modeling, it is shown that for each value of $x \in [-4 \quad 5]$, the nonlinear function (4.1) can be represented by two linear functions, $b_1 x$ and $b_2 x$, with two corresponding degrees of memberships μ_1 and μ_2. This relationship is shown below:

$$\dot{x} = (3 + x^2)x = \sum_{i=1}^{2}\mu_i b_i x = (\mu_1 b_1 + \mu_2 b_2)x \tag{4.2}$$

where the membership functions μ_1 and μ_2 are defined as follows:

$$\mu_1 = \frac{b_1 - (3 + x^2)}{b_1 - b_2} \tag{4.3a}$$

$$\mu_2 = \frac{(3 + x^2) - b_2}{b_1 - b_2} \tag{4.3b}$$

and b_1 and b_2 are the extremums of the nonlinear function (4.1) for $x \in [-4 \quad 5]$:

$$b_1 = \max(3 + x^2)\Big|_{x=5} = 28 \tag{4.4a}$$

$$b_2 = \min(3 + x^2)\Big|_{x=0} = 3 \tag{4.4b}$$

The nonlinear function (4.1) is shown within the sector in Figure 4.2.

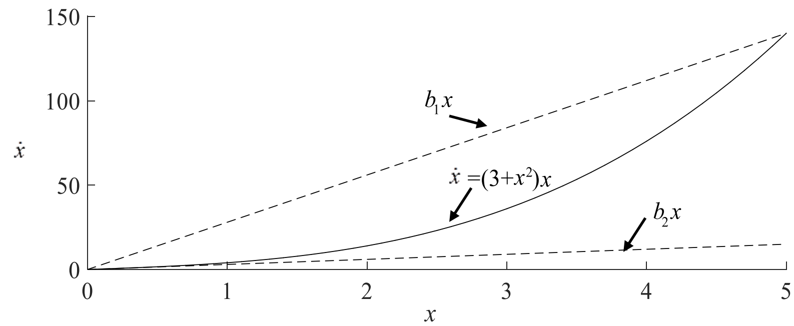

Figure 4.2. Sector nonlinearity approach.

4.2.2 Stability Analysis of a T-S Fuzzy Model

Consider a T-S fuzzy model, described by the following equation:

$$\dot{\boldsymbol{x}} = \sum_{\rho=1}^{r} \boldsymbol{A}_{\rho}^{cl} \boldsymbol{x} \tag{4.5}$$

where r is the number of fuzzy rules or equivalently number of local linear models. The stability of (4.5) can be established from the corresponding local linear models i.e., $\boldsymbol{A}_{\rho}^{cl}\boldsymbol{x}(\rho \in [1 \quad r])$, using the following theorem.

Theorem: The equilibrium point of the continuous T-S fuzzy system described by (4.5) is globally asymptotically stable if there exists a common positive definite matrix $\boldsymbol{P}$ such that for $\rho = 1 \ldots r$:

$$\begin{cases} \boldsymbol{P} = \boldsymbol{P}^{\mathrm{T}} > 0 & (4.6) \\ \boldsymbol{A}_{\rho}^{cl\,\mathrm{T}} \boldsymbol{P} + \boldsymbol{P}\boldsymbol{A}_{\rho}^{cl} < 0 & (4.7) \end{cases}$$

Proof: (Tanaka and Sugeno, 1992; Tanaka and Wang, 2001). According to the above theorem, in order to prove the stability of any system described by the T-S fuzzy model (4.5), a common matrix $\boldsymbol{P}$ must be found that satisfies conditions (4.6) and (4.7). Fortunately, these conditions can be stated as linear matrix inequalities (LMIs) (Boyd et al., 1994). These LMIs can be solved using available LMI Toolboxes (Gahinet et al., 1995). If LMIs are found feasible, it means that the solution matrix $\boldsymbol{P}$ exists. Any stability results for system in (4.5) can then be extended to the original nonlinear model due the exact representation (zero modeling error) of the original nonlinear system by the T-S fuzzy model within the corresponding sectors (Tanaka and Wang, 2001).

4.3 T-S Fuzzy Model of a Double-Rod Electro-Hydraulic Actuator

4.3.1 Nonlinear Model

In this section, using equations (2.1)-(2.7), presented in Section 2.1.1, the nonlinear dynamic equations of the double-rod electro-hydraulic actuator are obtained with variables, x_p, v_p, P_L, x_v, and η. Combining the differential equations of P_1 and P_2, to derive one equation for P_L, is carried out to avoid numerical problems when solving stability LMIs, presented in (4.6) and (4.7). It is also necessary for stability analysis of controllers, which will be designed for the output pressure, P_L, in this case. To obtain a differential equation for P_L, first, equation (2.3b) is subtracted from (2.3a). It is assumed that the piston is centered such that $V_{01}=V_{02}=V_t/2$. This assumption is made based on the fact that stability problems are more serious and challenging when the piston is centered (Merritt, 1967). It is also a valid assumption in pressure/force control applications, with small piston displacement around the midstroke. Also the definition and equation of the load flow Q_L are used, which are as follows:

$$Q_L = \frac{Q_1 + Q_2}{2} = K_v w x_v \sqrt{\frac{P_s - \text{sgn}(x_v) P_L}{2}} \tag{4.8}$$

As a result, the differential equation of P_L is:

$$\dot{P}_L = \frac{4\beta}{V_t}\left(K_v w x_v \sqrt{\frac{P_s - \text{sgn}(x_v) P_L}{2}} - k_T P_L - A v_p\right) \tag{4.9}$$

where $k_T = (k_i + \frac{k_e}{2})$, and is called the total leakage coefficient in the electro-hydraulic actuator. Then the friction in equation (2.10) is substituted for f_f in equation (2.7b), and f_l is considered as zero. The resultant equations are shown as follows:

$$\dot{x}_p = v_p \tag{4.10a}$$

$$\dot{v}_p = \frac{A}{m}(P_L - \frac{k}{A}x_p - \frac{d+\sigma_1}{A}v_p - \frac{(\sigma_0 - \sigma_1\sigma_0\psi(v_p))\eta}{A}) \tag{4.10b}$$

$$\dot{P}_L = \frac{4\beta}{V_t}(K_v w x_v \sqrt{\frac{P_s - \mathrm{sgn}(x_v)P_L}{2}} - k_T P_L - Av_p) \tag{4.10c}$$

$$\dot{x}_v = -\frac{1}{\tau}x_v + \frac{k_{sp}}{\tau}u_v \tag{4.10d}$$

$$\dot{\eta} = v_p - \sigma_0\psi(v_p)\eta \tag{4.10e}$$

where $\psi(v_p)$ is as follows:

$$\psi(v_p) = \frac{|v_p|}{F_c + (F_s - F_c)e^{-|v_p/v_s|^{\alpha_f}}} \tag{4.11}$$

4.3.2 T-S Fuzzy Model

Using the procedure explained in Section 4.2.1, a T-S fuzzy model is now constructed for the system described by (4.10). The nonlinearity in (4.10) originates from the load flow Q_L and friction term $\psi(v_p)$, which are assigned to variables $z_1(t)$ and $z_2(t)$, as follows:

$$z_1(t) = K_v w \sqrt{\frac{P_s - \mathrm{sgn}(x_v)P_L}{2}} \tag{4.12}$$

$$z_2(t) = \frac{|v_p|}{F_c + (F_s - F_c)e^{-|v_p/v_s|^{\alpha_f}}} \tag{4.13}$$

Now, some sectors should be established to rewrite the nonlinear functions $z_1(t)$ and $z_2(t)$ as $z_1(t)x_v \in [g_2 \quad g_1]x_v$ and $z_2(t)\eta \in [\delta_2 \quad \delta_1]\eta$. First, consider the nonlinear function $z_1(t)$, which can be rewritten as follows:

$$z_1(t) = G_1(z_1(t))g_1 + G_2(z_1(t))g_2 \tag{4.14}$$

where $G_{i(i=1,2)}(z_1(t))$ are positive membership functions defined as follows:

$$G_1(z_1(t)) = \frac{z_1(t) - g_2}{g_1 - g_2} \tag{4.15a}$$

$$G_2(z_1(t)) = \frac{g_1 - z_1(t)}{g_1 - g_2} \tag{4.15b}$$

and $\sum_{i=1}^{2} G_i(z_1(t)) = 1$. In the above equations, g_1 and g_2 are the extremums of $z_1(t)$:

$$g_1 = \max_{x_v(t),P_L(t)}(z_1(t)) \tag{4.16a}$$
$$g_2 = \min_{x_v(t),P_L(t)}(z_1(t)) \tag{4.16b}$$

To determine the above extremums, note that the value of $z_1(t)$ depends on the value of variable P_L, the sign of the variable x_v, and the values of parameters K_v, w, and P_s. For now, it is considered that there is no uncertainty in the above parameters, and their values can be substituted from Table 2.1. To find out the extremums of $z_1(t)$, the variation range for P_L, is considered for $x_v \geq 0$, $[P_{L\min+}\ P_{L\max+}]$, and for $x_v < 0$, $[P_{L\min-}\ P_{L\max-}]$. Note that as P_L increases, $z_1(t)$ decreases for $x_v \geq 0$ and increases for $x_v < 0$. Therefore, depending on the application, the extremums are found based on the following values:

$$\begin{cases} x_v \geq 0 & \begin{cases} z_1(t) = K_v w\sqrt{\dfrac{P_s - P_{L\min+}}{2}} & (4.17a) \\ z_1(t) = K_v w\sqrt{\dfrac{P_s - P_{L\max+}}{2}} & (4.17b) \end{cases} \\ x_v < 0 & \begin{cases} z_1(t) = K_v w\sqrt{\dfrac{P_s + P_{L\min-}}{2}} & (4.17c) \\ z_1(t) = K_v w\sqrt{\dfrac{P_s + P_{L\max-}}{2}} & (4.17d) \end{cases} \end{cases}$$

Note that if the values of the parameters K_v, w, and P_s vary within a sector, they should be considered in the calculation of the extremums of $z_1(t)$ in (4.17). The same procedure is carried out for the nonlinear function $z_2(t)$. Having δ_1 and δ_2 as the extremums of $z_2(t)$, the following sector is defined: $z_2(t)\eta \in [\delta_2 \quad \delta_1]\eta$. In this sector, $z_2(t)$ can be written as follows:

$$z_2(t) = \mathit{\Gamma}_1(z_2(t))\delta_1 + \mathit{\Gamma}_2(z_2(t))\delta_2 \tag{4.18}$$

The membership functions $\mathit{\Gamma}_{\gamma(\gamma=1,2)}(z_2(t))$ are defined as follows:

$$\mathit{\Gamma}_1(z_2(t)) = \frac{z_2(t) - \delta_2}{\delta_1 - \delta_2} \tag{4.19a}$$
$$\mathit{\Gamma}_2(z_2(t)) = \frac{\delta_1 - z_2(t)}{\delta_1 - \delta_2} \tag{4.19b}$$

where $\sum_{\gamma=1}^{2}\Gamma_\gamma(z_2(t))=1$. Substituting equations (4.14) and (4.18), respectively instead of nonlinear terms $z_1(t)$ and $z_2(t)$, in equations (4.10), results in the following equations:

$$\dot{x}_p = v_p \tag{4.20a}$$

$$\dot{v}_p = \frac{A}{m}(P_L - \frac{k}{A}x_p - \frac{d+\sigma_1}{A}v_p - \frac{1}{A}\left(\sigma_0 - \sigma_1\sigma_0\sum_{\gamma=1}^{2}\Gamma_\gamma(z_2(t)))\delta_\gamma\right)\eta) \tag{4.20b}$$

$$\dot{P}_L = \frac{4\beta}{V_t}(x_v\sum_{i=1}^{2}G_i(z_1(t)))g_i - k_T P_L - Av_p) \tag{4.20c}$$

$$\dot{x}_v = -\frac{1}{\tau}x_v + \frac{k_{sp}}{\tau}u_v \tag{4.20d}$$

$$\dot{\eta} = v_p - \sigma_0\sum_{\gamma=1}^{2}\Gamma_\gamma(z_2(t)))\ \delta_\gamma\eta \tag{4.20e}$$

Since $\sum_{i=1}^{2}G_i(z_1(t))=1$ and $\sum_{\gamma=1}^{2}\Gamma_\gamma(z_2(t))=1$, therefore $\sum_{i=1}^{2}\sum_{\gamma=1}^{2}G_\mathrm{i}(z_1(t))\Gamma_\gamma(z_2(t))=1$, which can be used to present equation (4.20) by a matrix form as follows:

$$\dot{\vec{\boldsymbol{x}}}(t) = \sum_{i=1}^{2}\sum_{\gamma=1}^{2}\left(G_i\left(z_1(t)\right)\Gamma_\gamma(z_2(t))\right)\left(\boldsymbol{A}_{i\gamma}\vec{\boldsymbol{x}}(t) + \boldsymbol{B}u_v\right) \tag{4.21}$$

where $\vec{\boldsymbol{x}} = \begin{bmatrix} x_p & v_p & P_L & x_v & \eta \end{bmatrix}^\mathrm{T}$ is the vector of the hydraulic states, and $\boldsymbol{A}_{i\gamma}$ and $\boldsymbol{B}$ are given as follows:

$$\boldsymbol{A}_{i\gamma} = \begin{bmatrix} 0 & 1 & 0 & 0 & 0 \\ \frac{-k}{m} & \frac{-(\sigma_1+d)}{m} & \frac{A}{m} & 0 & \frac{-(\sigma_0-\sigma_0\sigma_1\delta_\gamma)}{m} \\ 0 & -\frac{4\beta A}{V_t} & -\frac{4\beta}{V_t}k_T & \frac{4\beta}{V_t}g_i & 0 \\ 0 & 0 & 0 & \frac{-1}{\tau} & 0 \\ 0 & 1 & 0 & 0 & -\sigma_0\delta_\gamma \end{bmatrix} \tag{4.22a}$$

$$\boldsymbol{B} = \begin{bmatrix} 0 & 0 & 0 & \frac{k_{sp}}{\tau} & 0 \end{bmatrix}^\mathrm{T} \tag{4.22b}$$

In derivation of (4.21), parametric uncertainties were not considered. If the uncertainty is bounded, a representation analogous to (4.14) or (4.18) can be considered (Du and Zhang, 2009).

For example, if the environment stiffness is an unknown value in sector [k_2=$k_{\min}$ k_1=$k_{\max}$], it can be rewritten as:

$$k = S_1(k)k_1 + S_2(k)k_2 \tag{4.23}$$

where, $S_1(k)$ and $S_2(k)$ are membership functions defined as:

$$S_1(k) = \frac{k - k_2}{k_1 - k_2} \tag{4.24a}$$

$$S_2(k) = \frac{k_1 - k}{k_1 - k_2} \tag{4.24b}$$

Substituting (4.23) instead of k in dynamic equations (4.20), the resultant T-S fuzzy model has the following format:

$$\dot{\vec{x}}(t) = \sum_{i=1}^{2}\sum_{\gamma=1}^{2}\sum_{l=1}^{2} G_i(z_1(t))\Gamma_\gamma(z_2(t))S_l(k)\left(\boldsymbol{A}_{i\gamma l}\vec{x}(t) + \boldsymbol{B}u_v\right) \tag{4.25}$$

With $\boldsymbol{B}$ as in (4.22b), and $\boldsymbol{A}_{i\gamma l}$ as follows:

$$\boldsymbol{A}_{i\gamma l} = \begin{bmatrix} 0 & 1 & 0 & 0 & 0 \\ \dfrac{-k_l}{m} & \dfrac{-(\sigma_1 + d)}{m} & \dfrac{A}{m} & 0 & \dfrac{-(\sigma_0 - \sigma_0\sigma_1\delta_\gamma)}{m} \\ 0 & -\dfrac{4\beta A}{V_t} & -\dfrac{4\beta}{V_t}k_T & \dfrac{4\beta}{V_t}g_i & 0 \\ 0 & 0 & 0 & \dfrac{-1}{\tau} & 0 \\ 0 & 1 & 0 & 0 & -\sigma_0\delta_\gamma \end{bmatrix} \tag{4.26}$$

Other uncertain parameters can also be easily included using a similar manner as for the stiffness case in above T-S fuzzy model. The summations in (4.25) can then be aggregated as one summation (Tanaka and Wang, 2001):

$$\dot{\vec{x}}(t) = \sum_{\rho=1}^{8} q_\rho(z(t))\left(\boldsymbol{A}_\rho^*\vec{x}(t) + \boldsymbol{B}_\rho^* u_v\right) \tag{4.27}$$

where, $q_\rho(z(t)) = G_i(z_1(t))\Gamma_\gamma(z_2(t))S_l(k)$, and $\boldsymbol{A}_\rho^*$, $\boldsymbol{B}_\rho^*$, ρ, are as follows:

$$\boldsymbol{A}_\rho^* = \boldsymbol{A}_{i\gamma l},\ \boldsymbol{B}_\rho^* = \boldsymbol{B} \tag{4.28}$$

$$\rho = l + 2(\gamma - 1) + 4(i - 1) \tag{4.29}$$

Note that variable $z(t)$ in $q_\rho(z(t))$, is only used to simplify addressing $z_1(t)$, $z_2(t)$, and k. Now, T-S fuzzy model for the electro-hydraulic actuator with equations in (4.10) is as follows:

Model rule 1:

IF z_1(t) is G_1, and z_2(t) is Γ_1, and k is S_1
THEN $\dot{\vec{\boldsymbol{x}}}(t) = \boldsymbol{A}_1^* \vec{\boldsymbol{x}}(t) + \boldsymbol{B}_1^* u_v$
$\vdots$

Model rule 8:
IF z_1(t) is G_2, and z_2(t) is Γ_2, and k is S_2
THEN $\dot{\vec{\boldsymbol{x}}}(t) = \boldsymbol{A}_8^* \vec{\boldsymbol{x}}(t) + \boldsymbol{B}_8^* u_v$

4.4 Case Studies

In this section, the T-S fuzzy modeling and its stability theorem described in previous sections are employed to analyze the stability of three control systems developed for hydraulic actuators. The first case study relates to a nonlinear pressure controller designed for an uncertain model of a hydraulic actuator (Alleyne and Liu, 2000). The stability of this control system was proven previously using the passivity theory. In Section 4.4.1, the stability is verified again using the T-S fuzzy modeling and its stability approach. Here, this example is used to show the feasibility of the T-S fuzzy modeling approach. The second case study relates to the bilateral haptic control scheme for hydraulic actuators designed based on Lyapunov stability theory (Zarei-Nia and Sepehri, 2012). Stability of this control system was not discussed in the presence of parametric uncertainties. Using fuzzy modeling and its stability approach, the range of parameters for which the system remains stable is obtained thus extending the stability bounds. Finally, the approach is tried on a QFT position controller previously designed for the electro-hydraulic actuator by Karpenko and Sepehri (2008).

4.4.1 Case Study 1

Alleyne and Liu (2000) developed a robust nonlinear force/pressure controller for a hydraulic actuator with modeling errors and bounded uncertainties. In their experimental set-up, the cylinder is attached to a slide in contact with a linear spring. The following equations describe the system:

$$\dot{\xi}_1 = \xi_2 \tag{4.30a}$$

$$\dot{\xi}_2 = -\frac{k}{m}\xi_1 - \frac{b}{m}\xi_2 + \frac{A}{m}x_1 \tag{4.30b}$$

$$\dot{x}_1 = \underbrace{-\alpha\xi_2 - \beta x_1}_{f_1(\xi,x_1)} + \underbrace{\gamma(\sqrt{P_s - \mathrm{sgn}(x_2)x_1})}_{g_1(\xi,x_1)} x_2 \tag{4.30c}$$

$$\dot{x}_2 = \underbrace{-\frac{1}{\tau}x_2}_{f_2(\xi,x_1,x_2)} + \underbrace{\frac{k_{sp}}{\tau}}_{g_2(\xi,x_1,x_2)} u \tag{4.30d}$$

where ξ_1 and ξ_2 indicate the slide position and the velocity, respectively. x_1 denotes the cylinder pressure differential, x_2 is the valve spool position, and u is the control signal. The output to be controlled is the pressure differential x_1. Description and the values for the parameters in (4.30) are provided in Table 4.1. Nonlinear functions $f_1(\xi, x_1)$, $f_2(\xi, x_1, x_2)$, $g_1(\xi, x_1)$ and $g_2(\xi, x_1, x_2)$, are used in the controller design.

Table 4.1. Values of parameters in the system described by (4.30).

Parameter	Nominal value
Supply pressure, P_s (MPa)	10.3
Hydraulic coefficient, α (N/m^3)	1.51×10^{10}
Hydraulic coefficient, β (1/sec)	1.0
Hydraulic coefficient, γ (kg$^{0.5}$/m$^{1.5}$sec^2)	7.28×10^{8}
Load spring stiffness, k (kN/m)	16
Mass, m (kg)	24
Viscous damping, b (N.sec/m)	310
Piston area, A (m^2)	3.26×10^{4}

Accordingly, to achieve a stable force/pressure tracking system, the following control law was proposed by Alleyne and Liu (2000):

$$u \equiv \frac{1}{g_2}(-f_2 + \dot{x}_{2desired} - k_2 e_2) \tag{4.31a}$$

$$x_{2desired} \equiv \frac{1}{g_1}(-f_1 + \dot{x}_{1desired} - k_1 e_1) \tag{4.31b}$$

where $x_{1desired}$ and $x_{2desired}$ are the desired differential pressure and the desired valve spool displacement respectively. Errors e_1=x_1-$x_{1desired}$ and e_2=x_2-$x_{2desired}$, scaled by controller gains k_1 and k_2 are used to determine the control signal u. To determine the controller coefficients k_1 and k_2, first the controller equations (4.31) are substituted in the system equations (4.30) to construct the error dynamic equations as follows:

$$\dot{e}_1 = -k_1 e_1 + g_1 e_2 \tag{4.32a}$$

$$\dot{e}_2 = -k_2 e_2 \tag{4.32b}$$

Using the passivity theory, the global stability of (4.32) has been proven, previously, providing the controller gains to be selected as $k_1 = \max(|g_1|)$ and $k_2 = k_{sp} / \tau > 0$ (Alleyne and Liu, 2000). To analyze the stability of system (4.32) by the T-S stability theorem described in Section 4.2.2, first (4.32) must be represented by a T-S fuzzy model. Selecting the controller gains as $k_1 = \max(|g_1|) = \gamma\sqrt{P_s - \mathrm{sgn}(x_2)x_1} = 3.01\times10^{12}$ and $k_2 = k_{sp} / \tau = 1000$ (Alleyne and Liu, 2000), the error dynamic equations (4.32) are represented as the following T-S fuzzy model:

$$\begin{bmatrix} \dot{e}_1 \\ \dot{e}_2 \end{bmatrix} = \sum_{i=1}^{2} T_i \begin{bmatrix} -k_1 & t_i \\ 0 & -k_2 \end{bmatrix} \begin{bmatrix} e_1 \\ e_2 \end{bmatrix} \tag{4.33}$$

In (4.33), the membership functions $T_{i(i=1,2)}$ are defined as follows:

$$T_1 = \frac{\gamma\sqrt{P_s - \mathrm{sgn}(x_2)x_1}) - t_2}{t_1 - t_2} \tag{4.34a}$$

$$T_2 = \frac{t_1 - \gamma\sqrt{P_s - \mathrm{sgn}(x_2)x_1})}{t_1 - t_2} \tag{4.34b}$$

The extremums $t_{i(i=1,2)}$ are found for $P_L \in \left[-(2/3)P_s \quad (2/3)P_s\right] = \left[-6.86\,\mathrm{MPa} \quad 6.86\,\mathrm{MPa}\right]$. $(2/3)P_s$ is considered as the maximum output pressure as applied to hydraulic actuator (Merritt, 1967):

$$t_1 = \max(\gamma\sqrt{P_s - \mathrm{sgn}(x_2)x_1}) = \gamma\sqrt{10.3\,\mathrm{MPa} + 7\,\mathrm{MPa}} = 3.01\times10^{12}\ \frac{1}{\sec^2}\sqrt{\frac{\mathrm{kg.Pa}}{\mathrm{m}^3}} \tag{4.35a}$$

$$t_2 = \min(\gamma\sqrt{P_s - \mathrm{sgn}(x_2)x_1}) = \gamma\sqrt{10.3\,\mathrm{MPa} - 7\,\mathrm{MPa}} = 1.35\times10^{12}\frac{1}{\sec^2}\sqrt{\frac{\mathrm{kg.Pa}}{\mathrm{m}^3}} \tag{4.35b}$$

LMIs are now constructed based on conditions (4.6), (4.7), and two local linear models described by equation (4.33). Using the MATLAB LMI toolbox, the LMIs are found feasible given the following common positive definite matrix $\boldsymbol{P}$ as the solution:

$$\boldsymbol{P} = \begin{bmatrix} 1.17 & -0.72 \\ -0.72 & 9.72\times10^{8} \end{bmatrix} \tag{4.36}$$

Therefore, according to the stability theorem in Section 4.2.2, the closed-loop system is stable. This is exactly what was concluded based on the passivity theory used by Alleyne and Liu (2000). The result of this case study shows that the T-S fuzzy models and corresponding stability can be reliably employed to investigate the nonlinear stability of hydraulic control systems.

4.4.2 Case Study 2

Case study 2 is employed to not only confirm the existing stability results, but also extend the results to include uncertainty in a system parameter used by the controller. Zarei-nia and Sepehri (2012) developed a bilateral control system which allows a hydraulic actuator to achieve a stable position tracking at the slave side while, at the master side, the haptic device provides the feeling of tele-presence to the operator. The following equations were used by them to present the dynamics of the whole system:

Slave side
$$\dot{x}_1 = x_2 \tag{4.37a}$$
$$\dot{x}_2 = \frac{A}{m_s} x_3 - \frac{d}{m_s} x_2 - \frac{k_s}{m_s} x_1 \tag{4.37b}$$
$$\dot{x}_3 = \frac{-A}{C} x_2 + \frac{c_d w}{C\sqrt{\rho}} x_4 \sqrt{P_s - \mathrm{sgn}(x_4) x_3} \tag{4.37c}$$
$$\dot{x}_4 = \frac{-1}{\tau} x_4 + \frac{k_{sp}}{\tau} u \tag{4.37d}$$

Master side
$$\dot{x}_5 = v_6 \tag{4.37e}$$
$$\dot{x}_6 = \frac{1}{m_m}(F_h + F_m - k_d x_6 - k_h x_5) \tag{4.37f}$$

where, at the slave side, x_1, x_2, x_3 and x_4 are the actuator position, velocity, differential pressure and valve spool displacement, respectively. The control input is the voltage to the servovalve of the hydraulic actuator, shown by u. At the master side, x_5 and x_6 are the haptic device displacement and the velocity, respectively. F_h is the input force, originated from the operator and F_m is the control input applied to the master.

To implement a stable position tracking system, the following control laws were proposed (Zarei-nia and Sepehri, 2012):

$$u = \left[-K_{p1}(x_1 - x_5) - K_{p2} x_3\right]\sqrt{P_s - \mathrm{sgn}(x_4) x_3} \tag{4.38a}$$
$$F_m = K_{p3}(x_1 - x_5) + K_{p4} x_3 \tag{4.38b}$$

where K_{p1}, K_{p2}, K_{p3} and K_{p4} are constant gains. The description and values of the rest of the parameters are given in Table 4.2. To construct the closed-loop dynamic equations, the controller equations (4.38) were substituted into the master and the salve equations (4.37). The equilibrium of the closed-loop system was determined by imposing $\dot{x}_{i(i=1..6)} = 0$ as follows:

Table 4.2. Values of parameters in system described by (4.37).

Parameter	Nominal value
Supply pressure, P_s (MPa)	17.2
Hydraulic compliance, C (m^5/N)	2×10^{-13}
Spring stiffness, k_s (kN/m)	125
Piston and rod mass; slave side, m_s (kg)	12.3
Viscous damping coefficient, d (N.sec/m)	250
Piston area, A (m^2)	6.33×10^{-4}
Orifice coefficient of discharge, c_d	0.6
Hydraulic fluid density, ρ (kg/m^3)	847.15
time constant, τ (msec)	0.03
Valve orifice area gradient, w (m^2/m)	0.02075
Valve gain, k_{sp} (m/V)	2.79×10^{-5}
Inertia of master, haptic, m_m (kg)	0.545
Viscous coefficient at master side, k_d (N.sec/m)	2
Stiffness of human arm, k_h (N/m)	1000

$$\vec{x}_{eq} = \begin{bmatrix} x_{1eq} & x_{2eq} & x_{3eq} & x_{4eq} & x_{5eq} & x_{6eq} \end{bmatrix}^{\mathrm{T}} = \begin{bmatrix} x_{1ss} & 0 & x_{3ss} & 0 & x_{5ss} & 0 \end{bmatrix}^{\mathrm{T}} \tag{4.39}$$

where x_{1ss}, x_{2ss} and x_{3ss} are as follows:

$$x_{1ss} = \frac{K_{p1} A F_h}{(K_{p2}K_{p3}k_s - K_{p1}K_{p4}k_s + K_{p1}k_h A + K_{p2}k_h k_s)} \tag{4.40a}$$

$$x_{2ss} = \frac{K_{p1} k_s F_h}{(K_{p2}K_{p3}k_s - K_{p1}K_{p4}k_s + K_{p1}k_h A + K_{p2}k_h k_s)} \tag{4.40b}$$

$$x_{3ss} = \frac{K_{p1} A F_h + K_{p2} k_s F_h}{(K_{p2}K_{p3}k_s - K_{p1}K_{p4}k_s + K_{p1}k_h A + K_{p2}k_h k_s)} \tag{4.40c}$$

Defining $\vec{e} = \vec{x} - \vec{x}_{eq}$, the following error states were then derived:

$$\dot{e}_1 = e_2 \tag{4.41a}$$

$$\dot{e}_2 = \frac{A}{m_s} e_3 - \frac{d}{m_s} e_2 - \frac{k_s}{m_s} e_1 \tag{4.41b}$$

$$\dot{e}_3 = -\frac{A}{C} e_2 + \frac{c_d w}{C\sqrt{\rho}} e_4 \sqrt{P_s - \mathrm{sgn}(e_4)(e_3 + x_{3ss})} \tag{4.41c}$$

$$\dot{e}_4 = -\frac{1}{\tau} e_4 + \frac{k_{sp}}{\tau} [-K_{p1}(e_1 - e_5) - K_{p2} e_3] \sqrt{P_s - \mathrm{sgn}(e_4)(e_3 + x_{3ss})} \tag{4.41d}$$

$$\dot{e}_5 = e_6 \tag{4.41e}$$

$$\dot{e}_6 = \frac{1}{m_m} (K_{p3}(e_1 - e_3) + K_{p4} e_3 - k_d e_4 - k_h e_5 \tag{4.41f}$$

where, e_1, e_2, e_3 and e_4 are the actuator position error, velocity error, differential pressure error and valve spool displacement error, respectively. Error states e_5 and e_6 are the haptic device displacement error and the velocity error at the master side, respectively.

By employing Lyapunov stability theory, the authors concluded the following conditions to guarantee the stability of dynamic equations in (4.41):

$$\frac{9C}{7A} < \frac{K_{p2}}{K_{p1}} \tag{4.42a}$$

$$K_{p3} < \frac{k_h(K_{p2}A - K_{p1}C)}{7K_{p2}A - 5K_{p1}C} \tag{4.42b}$$

$$K_{p4} = K_{p3}\frac{C}{A} \tag{4.42c}$$

Now, the stability analysis of (4.41) is re-examined using T-S fuzzy modeling and the corresponding stability theorem. First using the T-S fuzzy modeling procedure discussed in Section 4.3.2, the only nonlinearity term in (4.41) is represented as follows:

$$z(t) = \sqrt{P_s - \operatorname{sgn}(e_4)(e_3 + x_{3ss})} = \sum_{i=1}^{2} h_{si} H_{si}(z(t)) = \sum_{j=1}^{2} h_{cj} H_{cj}(z(t)) \tag{4.43}$$

Since this term appears in both the system and the controller equations, subscripts s and c are used to separately refer to this nonlinear term in the third and fourth differential equations in (4.41). Membership functions $H_{si(i=1,2)}$ and $H_{cj(j=1,2)}$ are defined as follows:

$$H_{c1}(z(t)) = \frac{z(t) - h_{c2}}{h_{c1} - h_{c2}} \tag{4.44a}$$

$$H_{c2}(z(t)) = \frac{h_{c1} - z(t)}{h_{c1} - h_{c2}} \tag{4.44b}$$

$$H_{s1}(z(t)) = \frac{z(t) - h_{s2}}{h_{s1} - h_{s2}} \tag{4.44c}$$

$$H_{s2}(z(t)) = \frac{h_{s1} - z(t)}{h_{s1} - h_{s2}} \tag{4.44d}$$

Using nominal value for supply pressure given in Table 4.2, and for $P_L \in [-(2/3)P_s \quad (2/3)P_s] = [-11.5\,\text{MPa} \quad 11.5\,\text{MPa}]$, the extremums $h_{si(i=1,2)}$ and $h_{cj(j=1,2)}$ are found as follows:

$$h_{c1} = h_{s1} = \max(z(t)) = \max(\sqrt{P_s - \operatorname{sgn}(e_4)(e_3 + x_{3ss})}) = \max(\sqrt{P_s - \operatorname{sgn}(x_4)(x_3)}) = \sqrt{17.2\,\text{MPa} + 11\,\text{MPa}} = 5310\sqrt{\text{Pa}} \tag{4.45a}$$

$$h_{c2} = h_{s2} = \min(z(t)) = \min(\sqrt{P_s - \operatorname{sgn}(e_4)(e_3 + x_{3ss})}) = \min(\sqrt{P_s - \operatorname{sgn}(x_4)(x_3)}) = \sqrt{17.2\,\text{MPa} - 11.5\,\text{MPa}} = 2490\sqrt{\text{Pa}} \tag{4.45b}$$

Substituting (4.43) in (4.41), results in the following equation:

$$\begin{bmatrix} \dot{e}_1 \\ \dot{e}_2 \\ \dot{e}_3 \\ \dot{e}_4 \\ \dot{e}_5 \\ \dot{e}_6 \end{bmatrix} = \sum_{i=1}^{2}\sum_{j=1}^{2} H_{si}(z(t))H_{cj}(z(t)) \begin{bmatrix} 0 & 1 & 0 & 0 & 0 & 0 \\ \frac{-k_s}{m_s} & \frac{-d}{m_s} & \frac{A}{m_s} & 0 & 0 & 0 \\ 0 & \frac{-A}{C} & 0 & \frac{c_d w}{C\sqrt{\rho}} h_{si} & 0 & 0 \\ \frac{-k_{sp}K_{p1}}{\tau} & 0 & \frac{-k_{sp}K_{p2}}{\tau} h_{cj} & \frac{-1}{\tau} & \frac{k_{sp}K_{p1}}{\tau} & 0 \\ 0 & 0 & 0 & 0 & 0 & 1 \\ \frac{K_{p3}}{m_m} & 0 & \frac{K_{p4}-K_{p3}}{m_m} & \frac{-k_d}{m_m} & \frac{k_h}{m_m} & 0 \end{bmatrix} \begin{bmatrix} e_1 \\ e_2 \\ e_3 \\ e_4 \\ e_5 \\ e_6 \end{bmatrix} \tag{4.46}$$

Equation (4.46) accurately represents original nonlinear model (4.41). The stability theorem discussed in Section 4.2.2 is now employed for the stability analysis of the system represented in (4.46). First a set of controller gains that satisfies conditions (4.42) are substituted into (4.46); $K_{p1} = 0.05$, $K_{p2} = 2\times10^{-10}$, $K_{p3} = 0.0139$, and $K_{p4} = 4.4\times10^{-12}$. Next, linear matrix inequalities are constructed based on (4.6) and (4.7), and the local linear models in equation (4.46). Using the LMI toolbox, the common positive definite matrix $\boldsymbol{P}$ is found as follows:

$$\boldsymbol{P} = \begin{bmatrix} 5.21 & 0.08 & 0.27 & 1.99 & 2.48 & -2.07 \\ 0.08 & 7.24 & -0.27 & -1.49 & 0.83 & 1.1 \\ 0.27 & -0.27 & 8.52 & 0.78 & 0.31 & -0.75 \\ 1.99 & -1.49 & 0.78 & 12.19 & 8.98 & 12.71 \\ 2.48 & 0.83 & 0.31 & 8.98 & 349 & 40.53 \\ -2.07 & 1.1 & -0.75 & 12.71 & 40.53 & 813 \end{bmatrix} \tag{4.47}$$

Therefore, the proof of the stability for the controller in equation (4.38) with conditions (4.42) has been shown for the values of the parameters given in Table 4.2. However, the controller equation (4.38) requires an exact value for the supply pressure P_s. The issue of uncertainty in the value of supply pressure was not discussed in the reference by Zarei-nia and Sepehri (2012). Here, it is investigated to see whether the T-S fuzzy modeling and stability theorem can provide further insight into the stability of system (4.46) in the presence of uncertainty in the supply pressure. To incorporate such uncertainty, extremums $h_{si(i=1,2)}$ are re-calculated considering variation of P_s from its nominal value (17.2MPa), i.e., $P_s \in [13.8 \quad 22.6]\text{MPa}$. The new values for the extremums are then determined to be h_{s1} =6137 and h_{s2}= 2144. The positive definite matrix, $\boldsymbol{P}$ to satisfy the stability conditions (4.6) and (4.7), is determined to be:

$$
\boldsymbol{P} = \begin{bmatrix} 11 & 0.3 & 1.5 & 3.3 & 3.8 & 0.8 \\ 0.3 & 11 & -0.4 & -1.9 & -1.2 & 2.1 \\ 1.5 & -0.4 & 14 & 1.3 & 0.4 & 0.1 \\ 3.3 & -1.9 & 1.3 & 18 & 14 & 18 \\ 3.8 & -1.2 & 0.4 & 14 & 622 & 72 \\ 0.8 & 2.1 & 0.1 & 18 & 72 & 1450 \end{bmatrix} \tag{4.48}
$$

Selecting different gains for the controller based on condition (4.42) may extend or limit the allowable uncertainty ranges for the supply pressure.

This case study shows that T-S fuzzy modeling and corresponding stability theorem are not only effective to conclude the stability of a given control system, but also can be useful to extend the previously-developed stability results to include uncertainties.

4.4.3 Case Study 3

The previous two case studies established that the T-S fuzzy modeling approach is effective to investigate the stability of hydraulically-actuated control systems. In this section the approach is employed to study the nonlinear stability of QFT controllers. Before this, efforts have been made to incorporate nonlinear stability bounds in the design process of QFT controllers. Wang et al. (1990) employed the Circle Criterion in the process of QFT design to study the effects of time-varying gain on both the stability and performance of the control system. Oldak et al. (1994) suggested using describing function and the Circle Criterion along with QFT design to avoid limit cycles. Barreiro and Banos (2000) employed combined Circle Criterion and Popov Criterion to incorporate the Input/output (I/O) stability bounds in the process of QFT controller design for memoryless and sector-bounded nonlinear plants. Incorporating these stability bounds provide rigorous stability results, but assign very conservative restrictions on the QFT controller (Banos, 2007). Banos et al. (2002) employed harmonic balance and multiplier theory. Harmonic balance provides an approximated solution to the global stability problem, but results in very relaxed conditions. Multiplier theory is a less conservative version of absolute stability; however, finding appropriate multipliers is qualitative (Banos et al., 2002). Also, using the standard approach of construction of Lyapunov functions to ensure the stability of the already developed QFT control systems is very difficult, if not impossible. So the challenge is how to investigate and ensure the stability of a QFT control system, without assigning conservative conditions on the QFT controller, or face the challenge of finding a Lyapanov function. Using T-S fuzzy modeling approach and its stability theorem, without assigning conservative conditions on QFT controllers, a solution for the nonlinear stability analysis of QFT controllers is provided (Esfandiari and Sepehri, 2013). T-S fuzzy modeling for electro-hydraulic actuators have been previously used in the process of designing a fuzzy static output feedback controllers based on parallel distributed compensation scheme (Du and Zhang, 2009). Here, T-S fuzzy model of the electro-hydraulic actuator is blended with the designed QFT controller to investigate the nonlinear stability of the closed-loop system. Using this solution, the nonlinear stability analysis becomes independent from the design process of QFT controllers. In this solution, a T-S fuzzy model for the closed-loop system with QFT controller is developed and then it is investigated whether the local linear systems in the corresponding T-S fuzzy model satisfy the conditions of the theorem, presented in Section 4.2.2. This approach provides several advantages: it does not assign any conditions on QFT controller, parametric uncertainties can be incorporated in the stability analysis, and since the stability conditions are in the form of LMIs, they can be solved using available numerical algorithms (Boyed, et al., 1994). In this section, the above stability solution is applied on the case study of a QFT position controller developed earlier for a double-rod electro-hydraulic actuator (Karpenko and Sepehri, 2008). The equations describing the dynamics of the system to be controlled are shown below:

$$\dot{x}_p = v_p \tag{4.49a}$$

$$\dot{v}_p = \frac{1}{m}(AP_1 - AP_2 - kx_p - dv_p) \tag{4.49b}$$

$$\dot{P}_1 = \frac{\beta}{V_1}\left(k_v w x_v \sqrt{\frac{P_s - P_r}{2} + \mathrm{sgn}(x_v)\left(\frac{P_s + P_r}{2} - P_1\right)} - Av_p\right) \tag{4.49c}$$

$$\dot{P}_2 = \frac{\beta}{V_2}\left(-k_v w x_v \sqrt{\frac{P_s - P_r}{2} + \mathrm{sgn}(x_v)\left(P_2 - \frac{P_s + P_r}{2}\right)} + Av_p\right) \tag{4.49d}$$

$$\dot{x}_v = v_v \tag{4.49e}$$

$$\dot{v}_v = -\omega_v^2 x_v - 2\xi_v \omega_v v_v + k_{sp}\omega_v^2 u_v \tag{4.49f}$$

where x_p and v_p are the position and the velocity of the hydraulic actuator respectively. P_1 and P_2 denote the pressures in chambers 1 and 2, respectively. x_v and v_v are the position and the velocity of spool valve, respectively. The system input is the voltage applied to the servovalve (u_v). Description and values for the rest of the parameters are given in Table 4.3. Note that the system has parametric uncertainties for the supply pressure (P_s), bulk modulus (β), total mass (m), viscous damping (d), stiffness of the environment (k), and valve spool gain (k_{sp}).

Table 4.3. Values of parameters in the system described by (4.49).

Parameter	Nominal value	Uncertainty range
Effective piston area, A (mm^2)	633	-
Length of rod, L (mm)	610	-
Flow coefficient, K_v (m$^{3/2}$/kg$^{1/2}$)	0.0292	-
Orifice area gradient, w (mm^2/mm)	13.2	-
Valve damping ratio, ξ_v	0.9	-
Valve natural frequency, ω_v (Hz)	150	-
Supply pressure, P_s (MPa)	17.2	13.8-18.6
Total mass, m (kg)	12.3	11-13.7
Viscous damping, d (N.sec/m)	250	200-300
Fluid bulk modulus, β (MPa)	689	345-1030
Spool position gain, k_{sp} (μm/V)	28	25-31
Load stiffness, k (kN/m)	30	0-60

To provide accurate position tracking for the hydraulic actuator despite parametric uncertainties, the following QFT controller was designed by Karpenko and Sepehri (2008):

$$G(s) = \frac{U_v(s)}{E_{x_p}(s)} = \frac{2.76\times 10^6 (s+25)}{(s+16)(s^2+108s+120^2)} \tag{4.50}$$

where the input to the controller is the error between the desired position and the actual position, $e_{x_p} = (x_{pdesired} - x_p)$, and the output of the controller is the voltage signal, u_v, applied to the servovalve. To study the stability of the QFT controller in (4.50) for the hydraulic actuator in (4.49), the closed-loop system should be represented by a T-S fuzzy model. Figure 4.3 shows the closed-loop structure of the system using the state-space representation of the controller as follows:

$$\begin{cases} \dot{\vec{\boldsymbol{x}}}_c = \boldsymbol{A}_c \vec{\boldsymbol{x}}_c + \boldsymbol{B}_c (x_{pdesired} - x_p) \\ u_v = \boldsymbol{C}_c \vec{\boldsymbol{x}}_c \end{cases} \tag{4.51}$$

where, $\vec{\boldsymbol{x}}_c = [x_{c1} \ \cdots \ x_{c\lambda}]^{\mathrm{T}}$, is the state vector of the controller and $\boldsymbol{A}_c$, $\boldsymbol{B}_c$, $\boldsymbol{C}_c$ are given as follows:

$$\boldsymbol{A}_c = \begin{bmatrix} -124 & -16128 & -230400 \\ 1 & 0 & 0 \\ 0 & 1 & 0 \end{bmatrix} \tag{4.52a}$$

$$\boldsymbol{B}_c = \begin{bmatrix} 1 & 0 & 0 \end{bmatrix}^{\mathrm{T}} \tag{4.52b}$$

$$\boldsymbol{C}_c = \begin{bmatrix} 0 & 2760000 & 690000000 \end{bmatrix} \tag{4.52c}$$

For the above state-space representation, λ=3. The state-space representation of the controller will be added to the T-S fuzzy model of the hydraulic system.

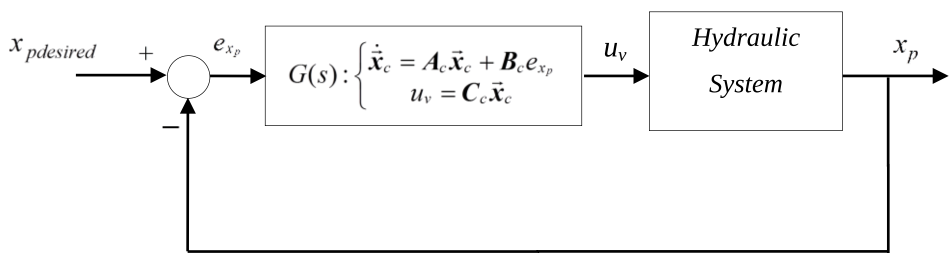

Figure 4.3. Closed-loop position control system.

For the hydraulic actuator, the T-S fuzzy model obtained in (4.21) and (4.22) can be used after removing the terms related to the friction and leakages, since the system presented in (4.49) does not include the friction and leakages. Also, the first order servovalve equation in (4.21) and (4.22) is replaced with the second order equations in (4.49). The uncertain parameters are incorporated in the T-S fuzzy model using the approach explained in Section 4.3.2. The resultant T-S fuzzy model is as follows:

$$\dot{\vec{x}}(t) = \sum_{i=1}^{2}\sum_{l=1}^{2}\sum_{n=1}^{2}\sum_{r=1}^{2}\sum_{j=1}^{2}\sum_{w=1}^{2} G_i(z_1(t))S_l(k)N_n(d)M_r(m)H_j(\beta)W_w(k_{sp})\left(\boldsymbol{A}_{ilnrjw}\vec{x}(t) + \boldsymbol{B}_{ilnrjw}u_v\right) \tag{4.53}$$

where $\boldsymbol{A}_{ilnrjw}$ and $\boldsymbol{B}_{ilnrjw}$ are as follows:

$$\boldsymbol{A}_{ilnrjw} = \begin{bmatrix} 0 & 1 & 0 & 0 & 0 \\ \frac{-k_l}{m_r} & \frac{-d_n}{m_r} & \frac{A}{m_r} & 0 & 0 \\ 0 & -\frac{4\beta_j A}{V_t} & 0 & \frac{4\beta_j}{V_t}g_i & 0 \\ 0 & 0 & 0 & 0 & 1 \\ 0 & 0 & 0 & -\omega_v^2 & -2\xi_v\omega_v \end{bmatrix} \tag{4.54a}$$

$$\boldsymbol{B}_{ilnrjw} = \begin{bmatrix} 0 & 0 & 0 & 0 & k_{sp_w}\omega_v^2 \end{bmatrix}^{\mathrm{T}} \tag{4.54b}$$

Note that $S_l(k)$, $N_n(d)$, $M_r(m)$, $H_j(\beta)$, and $W_w(k_{sp})$ are the membership functions related to the environment stiffness k, total damping d, total mass of m, effective bulk modulus β, and spool position gain k_{sp}. The uncertainty range of supply pressure P_s is incorporated in calculation of $g_{i(i=1,2)}$. The extremums $g_{i(i=1,2)}$ for $P_L \in \left[-(2/3)P_s \quad (2/3)P_s\right]$, and $P_s \in \left[13.8 \quad 18.6\right]\,\mathrm{MPa}$ are calculated as follows:

$$g_1 = \max(z_1(t)) = \max(\frac{K_v w}{\sqrt{2}}\sqrt{P_s - \mathrm{sgn}(x_v)P_L}) = \frac{K_v w}{\sqrt{2}}\sqrt{18.6\,\mathrm{MPa} + (\frac{2}{3}\times 18.6)\,\mathrm{MPa}} = 2.287\sqrt{\frac{\mathrm{m}^5\mathrm{Pa}}{\mathrm{kg}}} \qquad (4.55a)$$

$$g_2 = \min(z_1(t)) = \min(\frac{K_v w}{\sqrt{2}}\sqrt{P_s - \mathrm{sgn}(x_v)P_L}) = \frac{K_v w}{\sqrt{2}}\sqrt{13.6\,\mathrm{MPa} - (\frac{2}{3}\times 13.6)\,\mathrm{MPa}} = 0.881\sqrt{\frac{\mathrm{m}^5\mathrm{Pa}}{\mathrm{kg}}} \qquad (4.55b)$$

The summations in (4.53) can be aggregated as follows:

$$\dot{\vec{\boldsymbol{x}}}(t) = \sum_{\rho=1}^{64}\left(q_\rho(z(t))\right)\left(\boldsymbol{A}_\rho^*\vec{\boldsymbol{x}}(t) + \boldsymbol{B}_\rho^* u_v\right) \qquad (4.56)$$

where $\boldsymbol{A}_\rho^*$, $\boldsymbol{B}_\rho^*$, $q_\rho(z(t))$, and ρ, are:

$$\boldsymbol{A}_\rho^* = \boldsymbol{A}_{ilnrjw} \qquad (4.57a)$$

$$\boldsymbol{B}_\rho^* = \boldsymbol{B}_{ilnrjw} \qquad (4.57b)$$

$$q_\rho(z(t)) = G_i(z_1(t))S_l(k)N_n(d)M_r(m)H_j(\beta)W_w(k_{sp}) \qquad (4.57c)$$

$$\rho = w + 2(j-1) + 4(r-1) + 8(n-1) + 16(l-1) + 32(i-1) \qquad (4.57d)$$

Now to present the T-S fuzzy model of the closed-loop system, the state-space equations of the QFT controller in (4.51) is added to the T-S fuzzy model of the hydraulic actuator in (4.53) as follows:

$$\begin{cases} \dot{\vec{\boldsymbol{x}}}(t) = \sum_{\rho=1}^{64}\left(q_\rho(z(t))\right)\left(\boldsymbol{A}_\rho^*\vec{\boldsymbol{x}}(t) + \boldsymbol{B}_\rho^*\boldsymbol{C}_c\vec{\boldsymbol{x}}_c\right) & (4.58a) \\ \dot{\vec{\boldsymbol{x}}}_c = \boldsymbol{A}_c\vec{\boldsymbol{x}}_c + \boldsymbol{B}_c(x_{pdesired} - x_p) & (4.58b) \end{cases}$$

Since $\sum_{\rho=1}^{64}\left(q_\rho(z(t))\right) = 1$, the above equations can be easily combined as follows:

$$\begin{bmatrix} \dot{\vec{\boldsymbol{x}}} \\ \dot{\vec{\boldsymbol{x}}}_{\boldsymbol{c}} \end{bmatrix} = \sum_{\rho=1}^{64} q_\rho(z(t))\left(\begin{pmatrix} \boldsymbol{A}_\rho^* & \boldsymbol{B}_\rho^*\boldsymbol{C}_c \\ -\boldsymbol{B}_c\left[1 \quad (0)_{1\times 4}\right] & \boldsymbol{A}_c \end{pmatrix}\begin{bmatrix} \vec{\boldsymbol{x}} \\ \vec{\boldsymbol{x}}_{\boldsymbol{c}} \end{bmatrix} + \begin{bmatrix} (0)_{5\times 1} \\ \boldsymbol{B}_{\boldsymbol{c}} \end{bmatrix} x_{pdesired}\right) \qquad (4.59)$$

Equation (4.59) describes the T-S fuzzy model of the QFT positioning control system shown in Figure 4.3. To investigate the stability of this system using stability theorem discussed in Section 4.2.2, first by setting $\begin{bmatrix}\dot{\vec{x}}^{\mathrm{T}} & \dot{\vec{x}}_c^{\mathrm{T}}\end{bmatrix}^{\mathrm{T}} = \begin{bmatrix}\dot{x}_p & \dot{v}_p & \dot{P}_L & \dot{x}_v & \dot{v}_v & \dot{x}_{c1} & \cdots & \dot{x}_{c\lambda}\end{bmatrix}^{\mathrm{T}} = 0$, the following equilibrium point is obtained:

$$\begin{bmatrix}\vec{x}_{eq}^{\mathrm{T}} & \vec{x}_{ceq}^{\mathrm{T}}\end{bmatrix} = \begin{bmatrix} x_{pdesired} & 0 & \dfrac{kx_{pdesired}}{A} & 0 & 0 & x_{ceq1} & \cdots & x_{ceq\lambda}\end{bmatrix} \tag{4.60}$$

This equilibrium point (4.60) is not at the origin; therefore the error states are defined as $\vec{e} = \vec{x} - \vec{x}_{eq}$ and $\vec{e}_c = \vec{x}_c - \vec{x}_{ceq}$ with the following dynamic equations:

$$\begin{bmatrix}\dot{\vec{e}} \\ \dot{\vec{e}}_c\end{bmatrix} = \sum_{\rho=1}^{64} q_\rho(z(t)) \underbrace{\begin{pmatrix} \boldsymbol{A}_\rho^* & \boldsymbol{B}_\rho^*\boldsymbol{C}_c \\ -\boldsymbol{B}_c\begin{bmatrix}1 & (0)_{1\times 4}\end{bmatrix} & \boldsymbol{A}_c \end{pmatrix}}_{\boldsymbol{A}_{closed-loop}} \begin{bmatrix}\vec{e} \\ \vec{e}_c\end{bmatrix} \tag{4.61}$$

where $\boldsymbol{A}_{closed-loop}$ is as follows:

$$\boldsymbol{A}_{closed-loop} = \begin{bmatrix} 0 & 1 & 0 & 0 & 0 & [0]_{1\times\lambda} \\ \dfrac{-k_l}{m_r} & \dfrac{-d_n}{m_r} & \dfrac{A}{m_r} & 0 & 0 & [0]_{1\times\lambda} \\ 0 & -\dfrac{4\beta_j A}{V_t} & 0 & \dfrac{4\beta_j}{V_t} g_i & 0 & [0]_{1\times\lambda} \\ 0 & 0 & 0 & 0 & 1 & [0]_{1\times\lambda} \\ 0 & 0 & 0 & -\omega_v^2 & -2\xi_v\omega_v & k_{sp_w}\omega_v^2[\boldsymbol{C}_c]_{1\times\lambda} \\ [-\boldsymbol{B}_c]_{\lambda\times 1} & [0]_{\lambda\times 1} & [0]_{\lambda\times 1} & [0]_{\lambda\times 1} & [0]_{\lambda\times 1} & [\boldsymbol{A}_c]_{\lambda\times\lambda} \end{bmatrix} \tag{4.62}$$

Now, the stability of the system described by (4.61) and (4.62), can be investigated by T-S fuzzy stability theorem. Based on the stability conditions (4.6) and (4.7), the corresponding LMIs are constructed. It was found that in order to find feasible LMIs, the uncertainty ranges for some of the parameters presented in Table 4.3, must be reduced. Given the new range of uncertain parameters, the following positive definite matrix $\boldsymbol{P}$ is obtained:

$$
\boldsymbol{P} = \begin{bmatrix}
2.781 & -6.5 & 441 & 1283 & 1387 & 624.8 & 963.7 & -15.4 \\
-6.5 & 198 & -5.4 & -232 & -74.5 & -30 & -47 & -52 \\
441 & -5.4 & 315.7 & 228.4 & 119.4 & 106 & 151.1 & -7.4 \\
1283 & -232 & 228.4 & 2502 & 1868 & -451.7 & 582 & -35.9 \\
1387 & -74.5 & 119.4 & 1868 & 2361.4 & 851.3 & 1099.5 & 231.8 \\
624.8 & -30 & 106 & -451.7 & 851.3 & 2141 & 1389 & 821.5 \\
963.7 & -47 & 151.1 & 582 & 1099.5 & 1389 & 1927.4 & 690.8 \\
-15.4 & -52 & -7.4 & -35.9 & 231.8 & 821.5 & 690.8 & 855.4
\end{bmatrix} \quad (4.63)
$$

Table 4.4 compares the range of parameters, for which the LMIs becomes feasible, with the one used to design the QFT position controller. Accordingly, the nonlinear stability of the QFT controller, designed for the parametrically uncertain hydraulic actuator is proven using T-S fuzzy modeling and stability theorem. Since the approach is systematic, it can be used to analyze the stability of other QFT controller designed for hydraulic actuators.

Table 4.4. Range of parametric uncertainties used in QFT design, and those which result in feasible LMIs for system described in (4.49).

Parameter	Range in QFT design	Range for feasible LMIs
Supply pressure, P_s (MPa)	13.8-18.6	13.8-18.6
Total mass, m (kg)	11-13.7	11-11.4
Viscous damping, d (N.sec/m)	200-300	200-300
Fluid bulk modulus, β (MPa)	345-1030	690-710
Spool position gain, k_{sp} (μm/V)	25-31	25.1-30.7
Load stiffness, k (kN/m)	0-60	20-36

4.5 Summary

In this chapter, it was shown that T-S fuzzy modeling and its stability theorem are appropriate tools for the nonlinear stability analysis of QFT controllers, designed for hydraulic actuation systems with parametric uncertainties. Using this approach, the stability conditions of the closed-loop system can be presented as linear matrix inequalities (LMIs). In order to validate the functionality of T-S modeling and its stability approach, the stability of three well-established controllers, designed for hydraulic actuators were re-analyzed. The first control system was a nonlinear pressure controller developed for a hydraulic actuator based on the passivity theory. Using T-S fuzzy modeling and its corresponding stability conditions, the stability results were consistent with those obtained from the passivity theory. The second control system was a bilateral haptic control of a hydraulic actuator designed based on the Lyapunov theory. For this control system, the proposed approach was able to further extend the stability region that included parametric uncertainties. Having successful results of validation of T-S fuzzy modeling and its stability theory, the stability of a QFT position controller was analyzed. This approach will be used for the nonlinear stability analysis of QFT controllers that are designed in the next chapters.

Chapter 5

Output Pressure Control of Electro-Hydraulic Actuator

This chapter is divided into two parts. First, a QFT output pressure controller is designed for the electro-hydraulic actuator described in Chapter 2. Next, the nonlinear stability of the resulting control system is analyzed using T-S fuzzy modeling and its stability theorem. To design a QFT control system, first a family of frequency responses of the electro-hydraulic actuator is obtained by linearizing the hydraulic function and constructing an equivalent linear plant set in Section 5.1. Then a QFT controller and a pre-filter are designed to satisfy desired performance criteria consisting of tracking, stability, and disturbance rejection. By designing the QFT controller and pre-filter, the frequency responses of the closed-loop system are placed within an acceptable envelope of frequency responses for the entire range of parametric uncertainties. It is shown that the upper and lower bounds of the envelope determine the minimum and the maximum values of the closed-loop bandwidths. In Section 5.3 it is demonstrated that re-defining the bounds in order to increases the bandwidth contributes to reduction of the sensitivity over low frequencies and increase the sensitivity at higher frequencies - a phenomenon known as 'waterbed effect' (Houpis et al., 2005). The increased sensitivity makes the system vulnerable to disturbances and subsequently reduces the stability margin (Houpis et al., 2005). It is shown that any increase in the bandwidth pushes the hydraulic system closed-loop poles towards the imaginary axis, resulting in higher overshoot and longer settling time. Thus, it is imperative that the controller maintains an adequate balance between performance, stability, and disturbance rejection while achieving a high bandwidth for the pressure tracking of the hydraulic actuator. Based on the insights from the discussion, a new QFT control system with higher bandwidth is designed in Section 5.3, followed by the experimental verification. In Section 5.4, using the T-S fuzzy modeling and its stability theorem, the nonlinear stability of the designed QFT controllers is investigated. For this stability analysis, the effects of parametric uncertainties, friction, and external and internal leakages are described.

5.1 Family of Frequency Responses

In order to design a robust output pressure controller based on QFT, a family of frequency responses of the electro-hydraulic actuator are required for the entire range of parametric uncertainties given in Table 2.1. Here, the frequency responses are generated from an equivalent linear plant set of the hydraulic actuator. The plant set is obtained by linearization of flow equations presented in (2.2) around desired operating points using small-signal approach. Using Taylor series and expanding nonlinear flow equations (2.2) around the operating point (x_{vo}, P_{1o}, P_{2o}), the linearized flows are:

$$\Delta Q_1 = Q_1 - Q_{1o} = \frac{\partial Q_1}{\partial x_v}(x_v - x_{vo}) + \frac{\partial Q_1}{\partial P_1}(P_1 - P_{1o}) = k_{1s}\Delta x_v - k_{1p}\Delta P_1 \tag{5.1a}$$

$$\Delta Q_2 = Q_2 - Q_{2o} = \frac{\partial Q_2}{\partial x_v}(x_v - x_{vo}) + \frac{\partial Q_2}{\partial P_2}(P_2 - P_{2o}) = k_{2s}\Delta x_v + k_{2p}\Delta P_2 \tag{5.1b}$$

In (5.1), the partial derivatives of the input flow Q_1 and the output flow Q_2 with respect to x_v, are represented by k_{1s} and k_{2s}, respectively and called valve flow gains. Terms k_{1p} and k_{2p} are called flow pressure coefficients, which are the partial derivatives of the input and the output flows with respect to P_1 and P_2, respectively. Since the valve is symmetric and the actuator is double-rod, by assuming a negligible return pressure i.e., $P_r \approx 0$, the supply pressure is $P_s \approx P_1 + P_2$. Employing this relationship and having $P_L = P_1 - P_2$, a proper approximation is to consider $k_{1s} \approx k_{2s}$ and $k_{1p} \approx k_{2p}$. The valve coefficients can therefore be written in terms of operating point of output pressure $P_{Lo} = P_{1o} - P_{2o}$ as follows:

$$k_s = K_v w \sqrt{\frac{(P_s - \mathrm{sgn}(x_{vo}) P_{Lo})}{2}} \tag{5.2a}$$

$$k_p = \frac{K_v w |x_{vo}|}{\sqrt{2(P_s - \mathrm{sgn}(x_{vo})P_{Lo})}} \tag{5.2b}$$

Assuming small piston displacement around the midstroke in pressure/force control applications, the volume of the hydraulic oil in each side of the piston is approximated as $V_1 \approx V_2 \approx V_t/2$, where V_t is the total volume of the chambers 1 and 2. Finally, the following equations represent the linearized state-space equations of the hydraulic actuator around the operating point (x_{vo}, P_{Lo}):

$$\Delta \dot{x}_p = \Delta v_p \tag{5.3a}$$

$$\Delta \dot{v}_p = \frac{1}{m}(A\Delta P_L - k\Delta x_p - d\Delta v_p - \Delta f_d) \tag{5.3b}$$

$$\Delta \dot{P}_L = \frac{4\beta}{V_t}(k_s \Delta x_v - 0.5 k_p \Delta P_L - A\Delta v_p) \tag{5.3c}$$

In the above model, the external and internal leakages are considered as zero. Using the servovalve dynamic equation in (2.1) and equations in (5.3), the transfer functions from the servovalve input voltage (U_v) and disturbance forces (F_d) to the output pressure (P_L) is derived as:

$$P_L(s) = \left(\frac{2\beta k_s k_{sp}}{\tau s + 1}\right)\left(\frac{(ms^2 + ds + k)}{(ms^2 + ds + k)(0.5V_t s + \beta k_p) + 2A^2\beta s}\right)U_v(s) + \left(\frac{(2As)}{(ms^2 + ds + k)(0.5V_t s + \beta k_p) + 2A^2\beta s}\right)F_d(s) \tag{5.4}$$

The first term on the right hand side of equation (5.4) represents the equivalent linear plant set as $G_{P_L}(s,\alpha)$:

$$G_{P_L}(s,\alpha) = \frac{P_L(s)}{U_v(s)} = \left(\frac{2\beta k_s k_{sp}}{\tau s + 1}\right)\left(\frac{(ms^2 + ds + k)}{(ms^2 + ds + k)(0.5V_t s + \beta k_p) + 2A^2\beta s}\right) \tag{5.5}$$

where α refers to a vector of parameters of the system from Table 2.1. The second term on the right hand side of (5.4), shows the effect of disturbances on the output pressure, and is denoted by $D(s)$, which should be attenuated by a proper design for the controller:

$$D(s) = \left(\frac{(2As)}{(ms^2 + ds + k)(0.5V_t s + \beta k_p) + 2A^2\beta s}\right)F_d(s) \tag{5.6}$$

In (5.5) the value of the valve flow gain k_s and flow pressure coefficient k_p depend on the operating points. To define these operating points, first a set of acceptable output pressure responses are defined; then corresponding spool displacements are obtained using equation (2.7).

Figure 5.1 shows the plots of the outputs-inputs. Following procedure shows that if the coefficients k_s and k_p are calculated in both the steady-state operating points and transient points, transfer function (5.5) can successfully reproduce the response of the nonlinear model of the electro-hydraulic actuator in both transient time and stead-state. In this procedure, each acceptable pair of input-output response is divided into finite sections, and one transient point for each section is considered. For example, an arbitrarily output pressure response of the electro-hydraulic actuator with the corresponding valve spool displacement are shown in Figures 5.2a and 5.2b, respectively. Seven points consisting of transient points and (steady-state) operating point are considered and shown by circles in Figure 5.2. Table 5.1 shows the corresponding coefficients k_s and k_p using (5.2) for all seven points. Figure 5.2c shows the output pressure response of the transfer function (5.5) when the values of coefficients k_s and k_p are updated over time according to Table 5.1. Transfer function (5.5) with time-varying coefficients k_s and k_p is called equivalent piecewise linear model.

Comparing Figure 5.2a and Figure 5.2c, it is seen that for an arbitrary vector of uncertain parameter α, the transfer function (5.5) can successfully represent the nonlinear model (2.7) if k_s and k_p are allowed to change in a coordinated manner. Thus, for the entire acceptable set of input-output responses in Figure 5.1, coefficients k_s and k_p are calculated and their variation range are given in Table 2.1. These coefficients are considered as uncertain parameters in the equivalent linear plant set (5.5). The family of frequency responses of the equivalent linear plant set are shown in Figure 5.3 for the entire range of parameters given in Table 2.1.

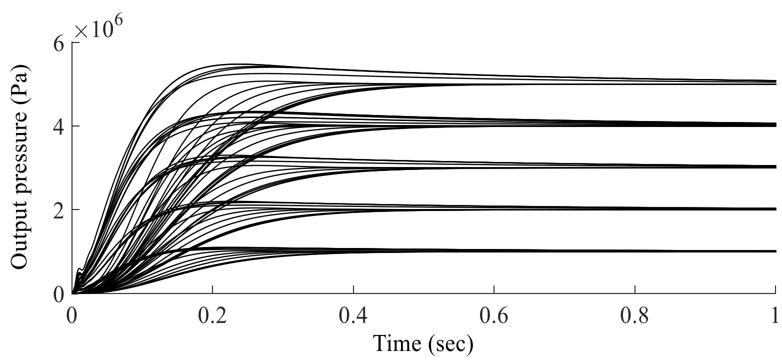

(a)

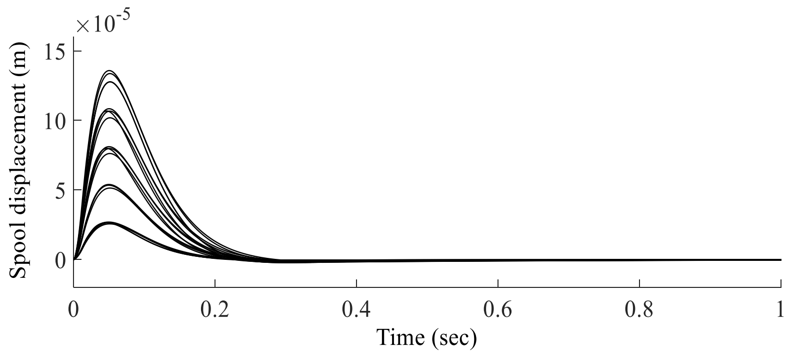

(b)

Figure 5.1. (a) Acceptable set of output pressure responses; (b) corresponding valve spool displacements.

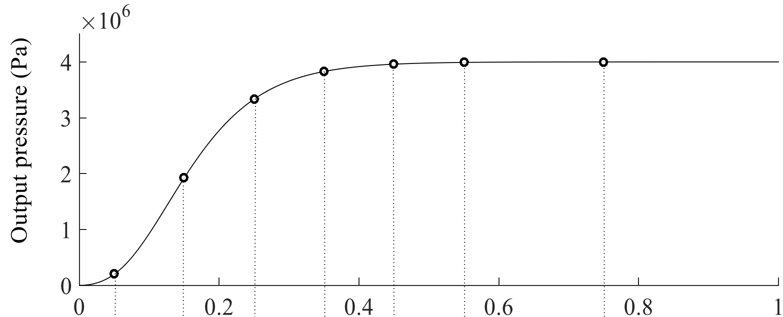

(a)

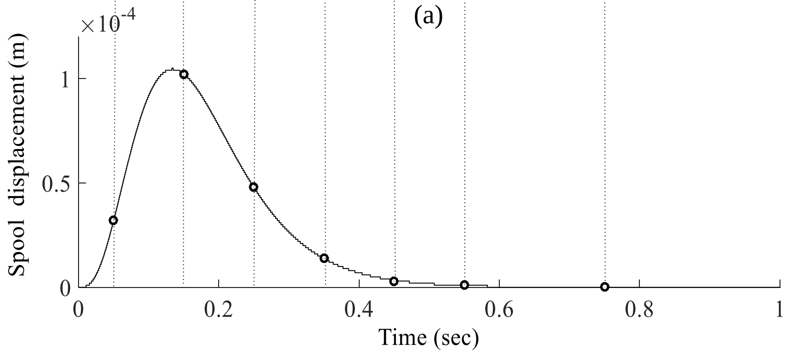

(b)

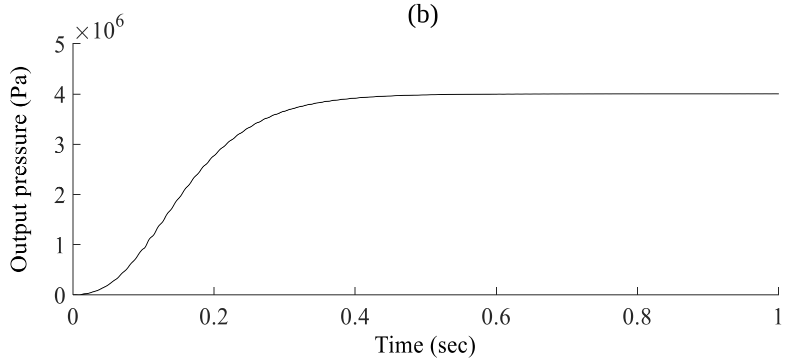

(c)

Figure 5.2. (a) Typical output pressure response; (b) corresponding valve spool displacement; (c) pressure response obtained from equivalent piecewise linear model.

Table 5.1. Flow and pressure coefficients for response in Figure 5.2.

Operating point	k_s (m^2/sec)	$k_p \times 10^{11}$ (m^3/sec/Pa)
1	1.72	0.32
2	1.63	1.08
3	1.55	0.53
4	1.53	0.16
5	1.52	0.03
6	1.52	0.01
7	1.73	0.00

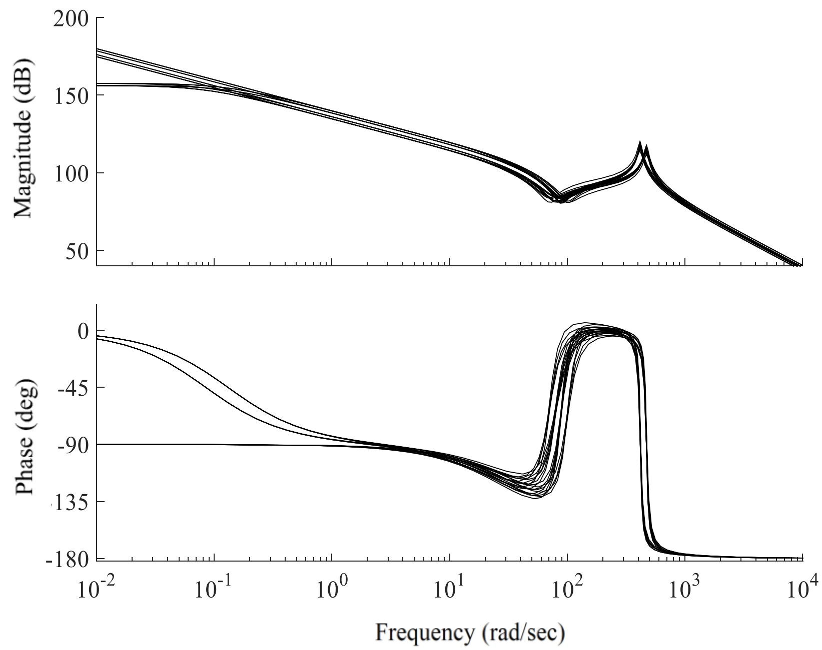

Figure 5.3. Bode plots of equivalent linear plant set.

5.2 Controller Design

In this section the steps for designing a QFT controller $C(s)$ and a pre-filter $F(s)$ for the output pressure of the electro-hydraulic actuator are described. The control structure is same as in Figure 3.1, for Y=P_L, R=$P_{Ldesired}$, and $G(s,\alpha) = G_{P_L}(s,\alpha)$. Generating templates, calculating bounds, loop-shaping, and designing a pre-filter are discussed respectively.

5.2.1 Generating Plant Templates

To generate plant templates, frequency responses obtained in Section 5.1 are plotted on the Nichols chart at the selected frequencies of ω={0.01,0.1,1,10,50,100,470} rad/sec, shown in Figure 5.4. In this figure, boundaries, shown by dashed-line distinguish the templates at each design frequency. These templates describe the total parametric uncertainty of the system in the frequency domain, used to generate QFT bounds, based on performance criteria. As can be seen from Figure 5.4, templates are bigger within two frequency ranges; around the natural frequency of the environment, i.e., $\omega_e = \sqrt{\frac{k}{m}}$, and around the natural frequency of the hydraulic system, $\omega_h = \sqrt{\frac{4\beta A^2}{mV_t} + \frac{k}{m}}$. This can also be clearly seen in bode plots in Figure 5.3. The reason of such drastic change in the templates is due to the low damping ratio (see Table 5.2). Table 5.2 gives the natural frequency and damping ratio of environment and electro-hydraulic actuator, derived from equation (5.5). Note that here, the term environment represents the load on the hydraulic actuator, originates from the total mass (m=m_h+m_e), total damping (d=d_h+d_e), and stiffness k.

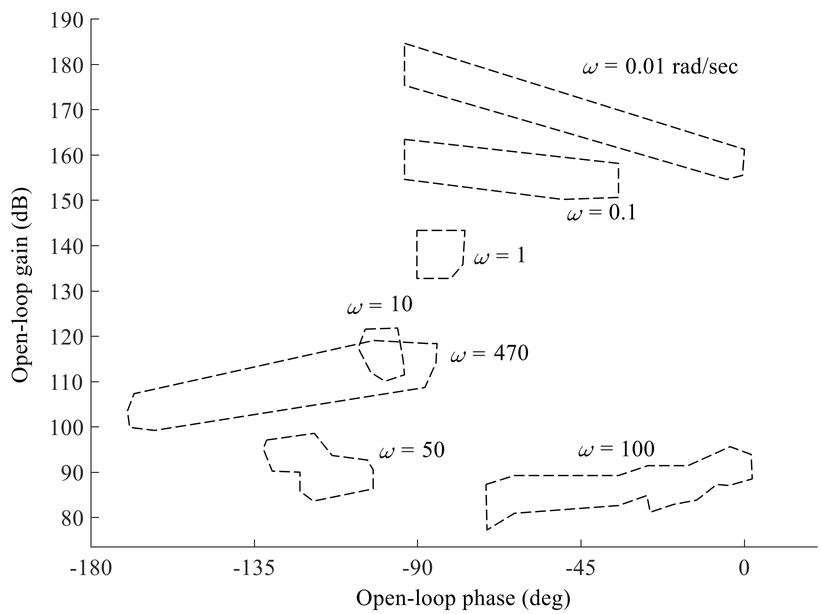

Figure 5.4. Plant templates at each design frequency (rad/sec) for entire range of parametric uncertainties.

Table 5.2. Natural frequency (rad/sec) and damping ratio of environment and electo-hydraulic actuator for entire variation range of parameters shown in Tables 2.1.

	hydraulic actuator	environment
Natural frequency	$\omega_h = \sqrt{\dfrac{4\beta A^2}{mV_t} + \dfrac{k}{m}} \in [415 \quad 475]$	$\omega_e = \sqrt{\dfrac{k}{m}} \in [70 \quad 105]$
Damping ratio	$\xi_h = \dfrac{dV_t\sqrt{\dfrac{4\beta A^2}{mV_t} + \dfrac{k}{m}}}{2(V_t k + 4\beta A^2)} \in [0.0254 \quad 0.0387]$	$\xi_e = \dfrac{d}{2\sqrt{mk}} \in [0.111 \quad 0.227]$

It is worth mentioning that in Figure 5.4, the large templates at very low frequencies, i.e., $\omega \leq 0.1$ rad/sec, are due to the variation range of flow pressure coefficient k_p which affects the system type (Karpenko and Sepehri, 2008).

5.2.2 QFT Bounds

The QFT design procedure is carried out in the Nichols chart, which requires all performance criteria to render in frequency domain. Employing templates, the corresponding graphical bounds are plotted in the Nichols chart (Borghesani et al., 2003). These QFT bounds depict the correlation between the actuator uncertainties and performance criteria at each design frequency. The following performance criteria are chosen:

i) *Closed-loop robust stability*. The robust stability constraint is given by placing an upper bound M_t on the complementary sensitivity transfer function:

$$\left|\frac{L(j\omega)}{1+L(j\omega)}\right| \leq M_t = 1.4 \ \forall \omega \in [0 \ \infty) \tag{5.7}$$

where $L(j\omega) = C\ (j\omega)G_{P_L}(j\omega, \alpha)$ is the loop transmission function. Criterion (5.7) implies a minimum gain margin of 4.68 dB, and a minimum phase margin of 42° for the closed-loop system according to equation (3.3) and (3.4).

ii) *Output disturbance rejection*. In a linear control system, the sensitivity transfer function is also the disturbance rejection function at the plant output. Therefore, to attenuate disturbances at the plant output, and to guarantee an acceptable robust stability margin, an upper tolerance must be imposed on the magnitude of the sensitivity transfer function as follows:

$$\left|\frac{1}{1+L(j\omega)}\right| \le M_s = 1.65 \;\; \forall\omega \in [0 \quad \infty) \tag{5.8}$$

In Section 5.3, it is discussed how the sensitivity upper bound influences the controller structure.

iii) *Robust reference input tracking*. The controller must satisfy inequality (5.9) for tracking performance requirement:

$$|T_l(j\omega)| \le \left|F(j\omega)\frac{L(j\omega)}{1+L(j\omega)}\right| \le |T_u(j\omega)| \;\; \forall\omega \in [0 \quad \infty) \tag{5.9}$$

where $T_u(j\omega)$ and $T_l(j\omega)$ are the upper and lower bounds, respectively. These bounds are built from specific time and frequency domain figures of merit (D'Azzo and Houpis, 1988). The time responses of the upper and lower bounds in (5.10) and (5.11) are shown in Figure 5.5. The bounds allow the system to have the maximum overshoot of 8% and settling time around 0.5 sec for the step response and provide a minimum bandwidth around 2 Hz (see equation (5.11)).

$$T_u(s) = \frac{15390(s+2)}{(s+2.28)(s+90)(s+150)} \tag{5.10}$$

$$T_l(s) = \frac{14400(s+15)}{(s+30)^2(s+20)(s+12)} \tag{5.11}$$

Design specifications (*i*)-(*iii*) are plotted as bounds on the Nichols chart and shown in Figure 5.6. These bounds are used in the next section to design a robust QFT controller through loop-shaping process.

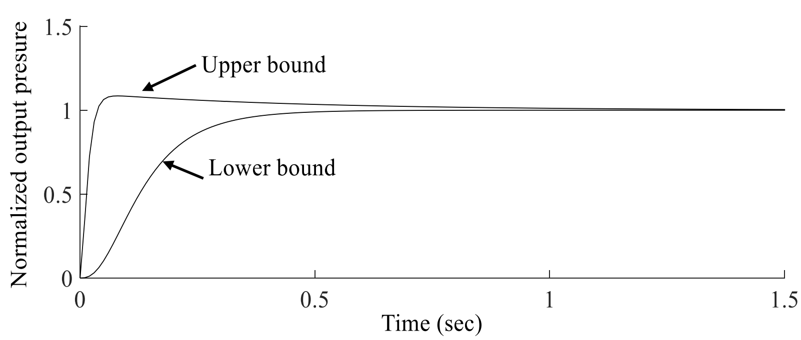

Figure 5.5. Time responses of tracking bounds.

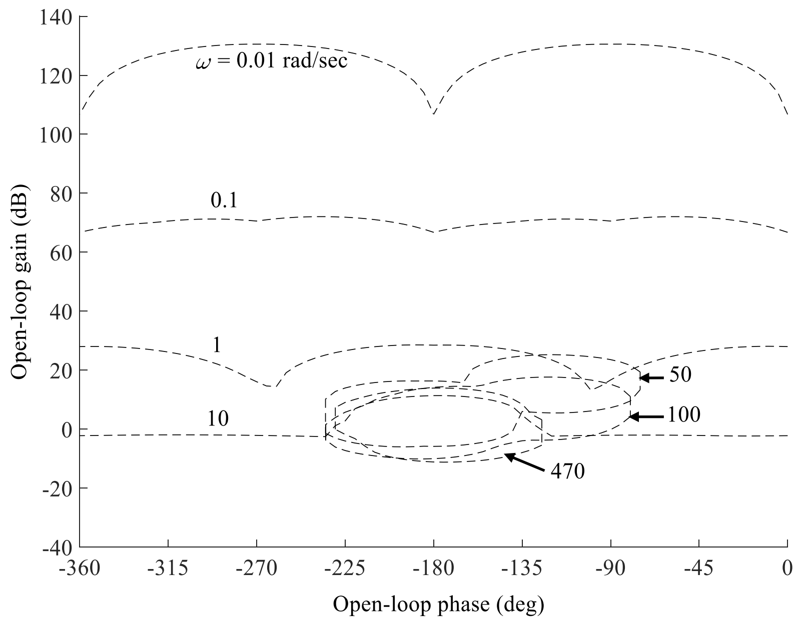

Figure 5.6. QFT bounds on Nichols chart for selected design frequencies (rad/sec).

5.2.3 Loop-Shaping and Pre-filter Design

Once the QFT bounds are constructed, by adjusting zeros and poles of the linear controller $C(s)$, the nominal loop transmission function, $L_0(s) = C(s)G_{P_{L0}}(s,\alpha)$, is shaped such that it lies on or above the corresponding open bounds and also does not enter the closed bounds at each frequency. According to Chapter 3, the controller should be designed with the minimum gain to reduce the cost of feedback, which refers to amplification of noise and effects of unmodeled dynamics. The nominal loop transmission function as well as the QFT bounds before any compensation, i.e., C=1, are shown in Figure 5.7a. It is also important to note that for the pressure control of the electro-hydraulic actuator with parametric uncertainties, simple structured controllers like proportional or integral-proportional do not guarantee a robust performance. To show this, the loop-shaping is shown using a proportional controller (0.0007 V/Pa) in Figure 5.7b, and using an integral-proportional controller ($0.16\times10^{-5} + \dfrac{3.37\times10^{-5}}{s}$) in Figure 5.7c. In both figures just a few regulations of the loop-shaping are satisfied.

Figure 5.8 shows the QFT bounds and the nominal loop transmission function using a more complex, yet low-order controller $C_1(s)$:

$$C_1(s) = \frac{18(s+0.75)}{s(s+210)(s^2+312s+50000)} \tag{5.12}$$

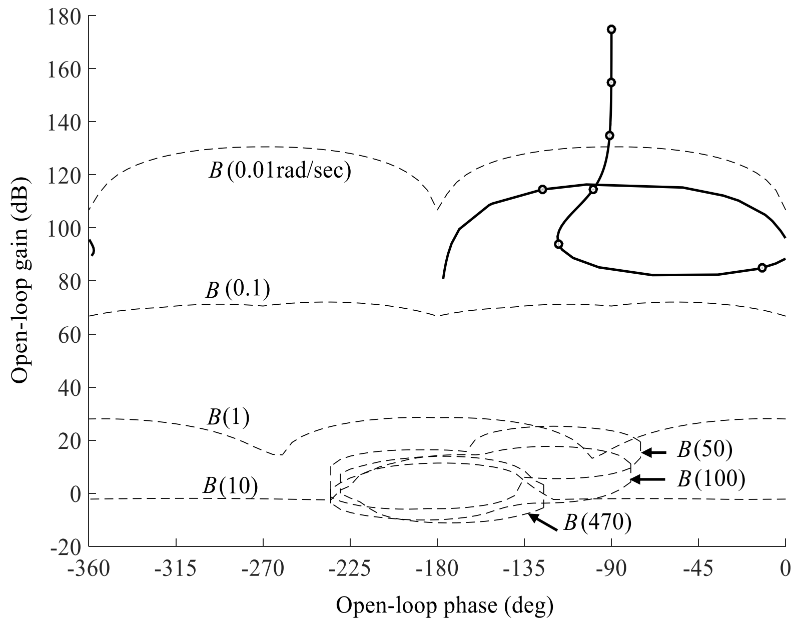

(a)

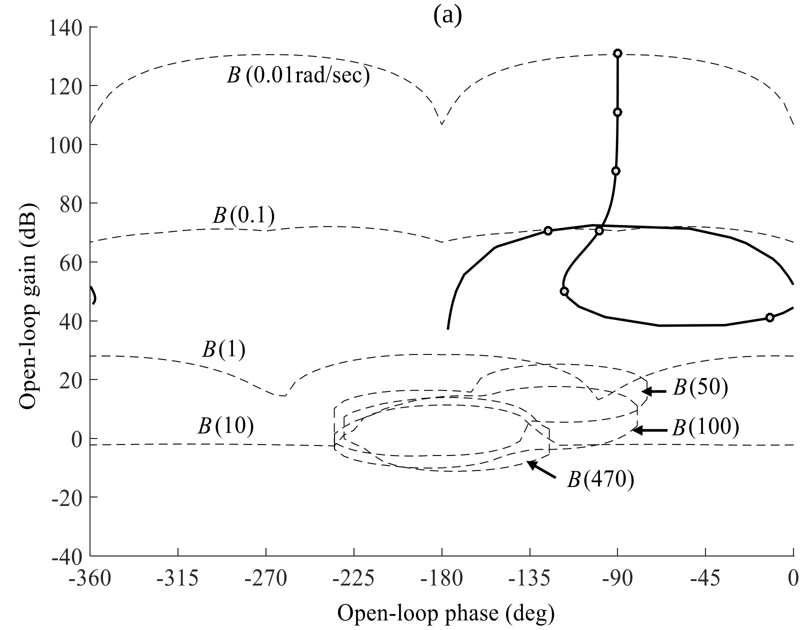

(b)

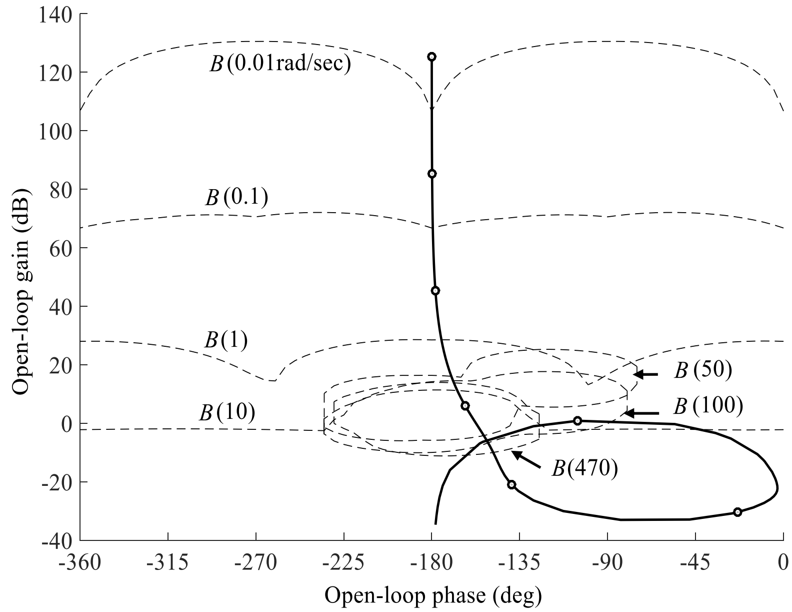

(c)

Figure 5.7. (a) QFT bounds and nominal loop transmission function before compensation; (b) after compensation by a proportional controller; (c) after compensation by a proportional-integral controller, at selected design frequencies (rad/sec).

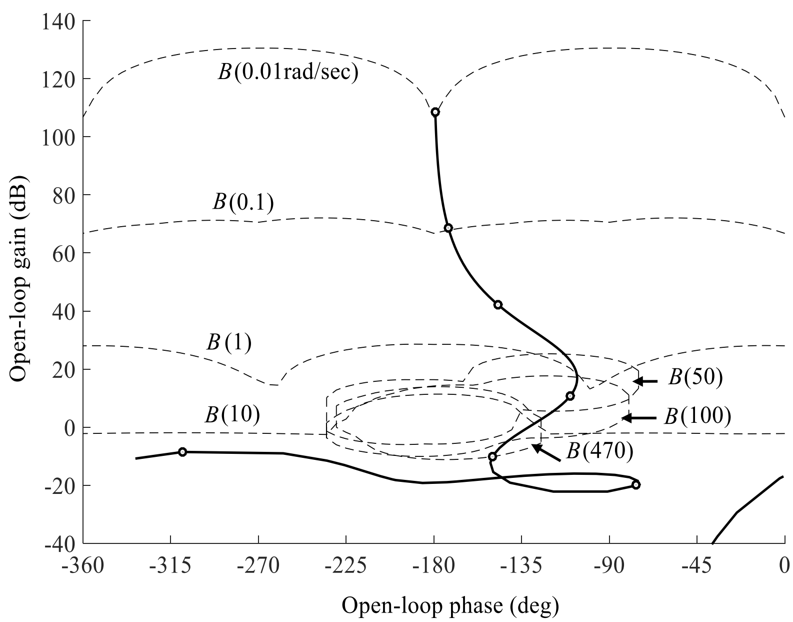

Figure 5.8. QFT bounds and compensated nominal loop transmission function using controller in (5.12).

Then to satisfy the tracking specification, pre-filter $F_1(s)$ is designed to place the closed-loop frequency responses in the desired range; between $T_l(s)$ and $T_u(s)$.

$$F_1(s) = \frac{141(s+7)}{(s+11)(s+90)} \tag{5.13}$$

Figure 5.9 shows the frequency response of the sensitivity and the closed-loop system using controller (5.12) and pre-filter (5.13) for the entire range of uncertainties given in Table 2.1.

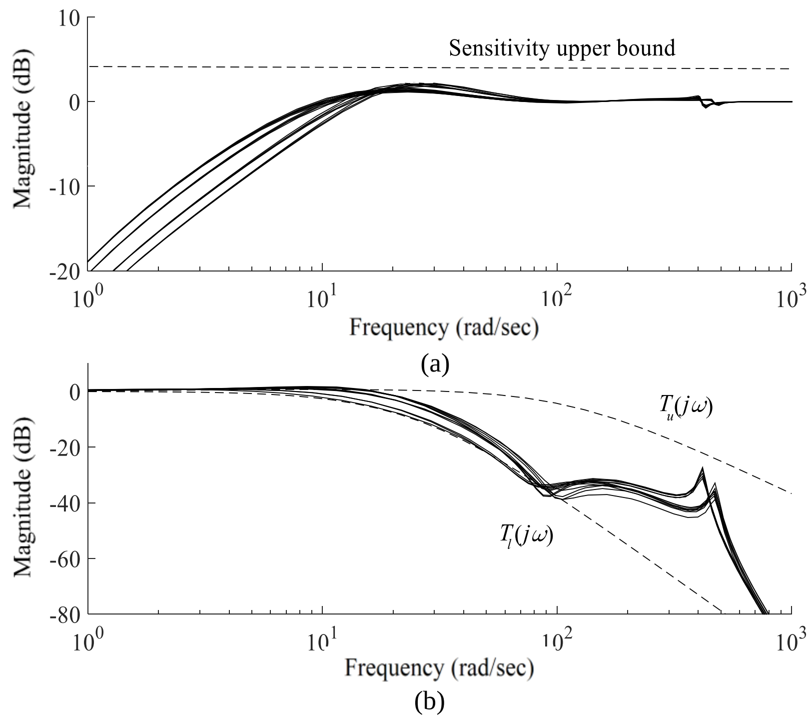

Figure 5.9. (a) Frequency responses of sensitivity; (b) corresponding frequency responses of closed-loop system, using controller (5.12) and pre-filter (5.13) and for entire range of parametric uncertainties given in Table 2.1.

5.2.4 Experimental Validation

In this section, the designed controller and the pre-filter are applied to the experimental test-bed of the electro-hydraulic actuator, described in Chapter 2. For these experiments, the actuator is operated against a spring of 125 kN/m. Figure 5.10 shows the normalized output pressure of the hydraulic actuator in tracking different desired step inputs with magnitudes of 1 MPa, 2 MPa, 3 MPa, 4 MPa and 5 MPa, as well as the corresponding control signals. These results show that the control system successfully tracks the desired step input of different magnitudes. The settling time is around 0.4 sec, and no overshoot is observed.

Figure 5.11 shows the output pressure of the hydraulic actuator to a desired sinusoidal input with the peak-to-peak amplitude of 4 MPa and the frequency of 1 Hz. Results show that the control system successfully tracks the desired sinusoidal input; the phase lag is 20° and the output amplitude reaches 95% of the desired input amplitude. The simulation results of the same input are shown in Figure 5.12. Next, the frequency of the input is increased to 2 Hz. Figure 5.13 shows the results. The phase lag is 30°, and the amplitude of the output is 80% of the desired input, which is still considered acceptable according to the definition of the bandwidth (less than -3 dB attenuation). The simulation results of the same input are shown in Figure 5.14.

As a result, employing controller (5.12) and pre-filter (5.13), the achieved bandwidth for the pressure tracking is around 2 Hz. In the next section, it is explained under what conditions, higher bandwidth can be obtained.

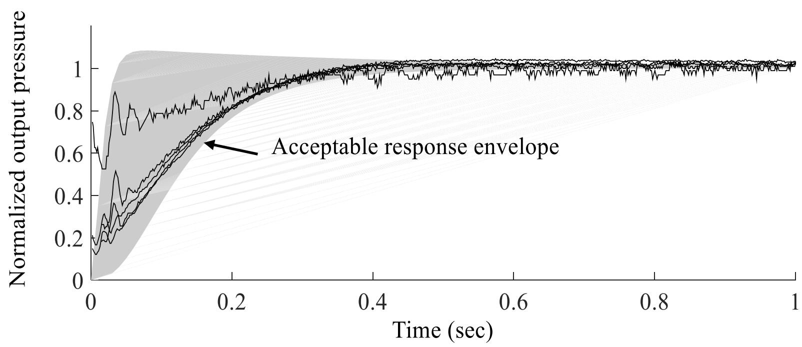

(a)

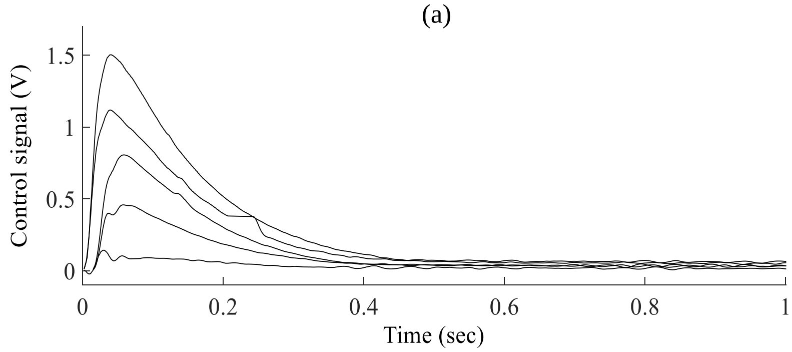

(b)

Figure 5.10. (a) Normalized output pressure responses in tracking of different step inputs (1-5 MPa); (b) corresponding control signals.

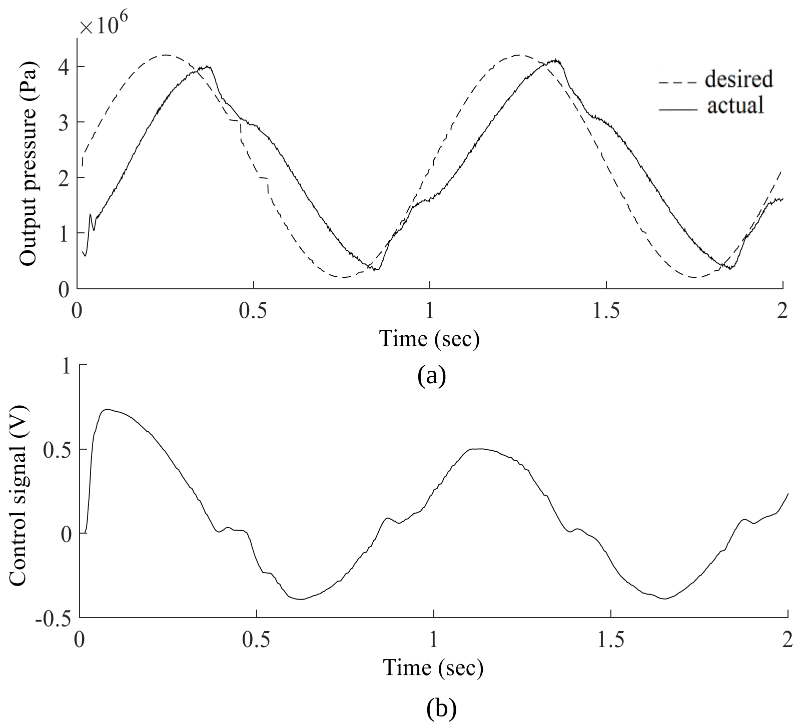

Figure 5.11. (a) 1 Hz sinusoidal output pressure tracking; (b) corresponding control signal.

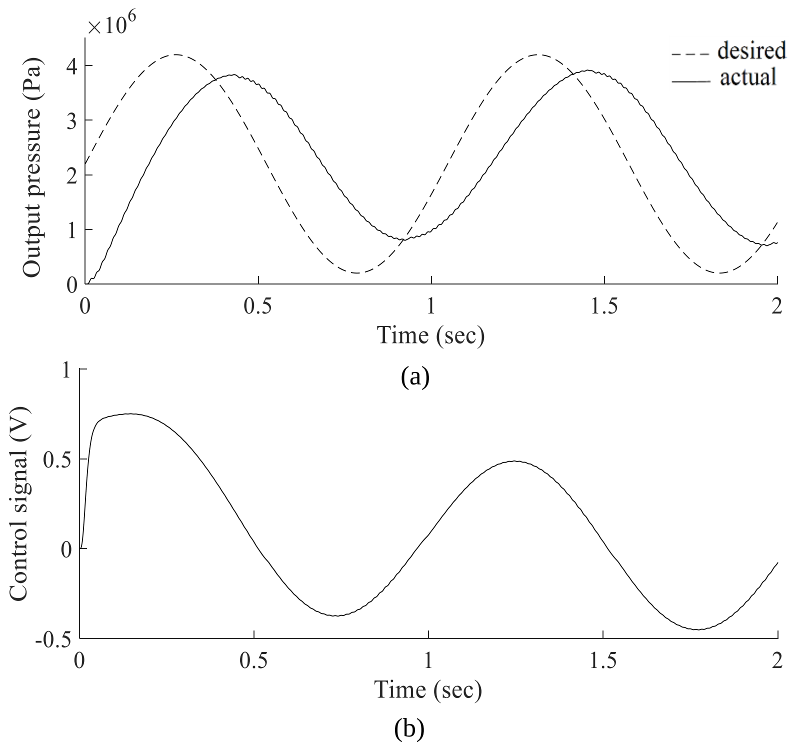

Figure 5.12. Simulation results: (a) 1 Hz sinusoidal output pressure tracking; (b) corresponding control signal.

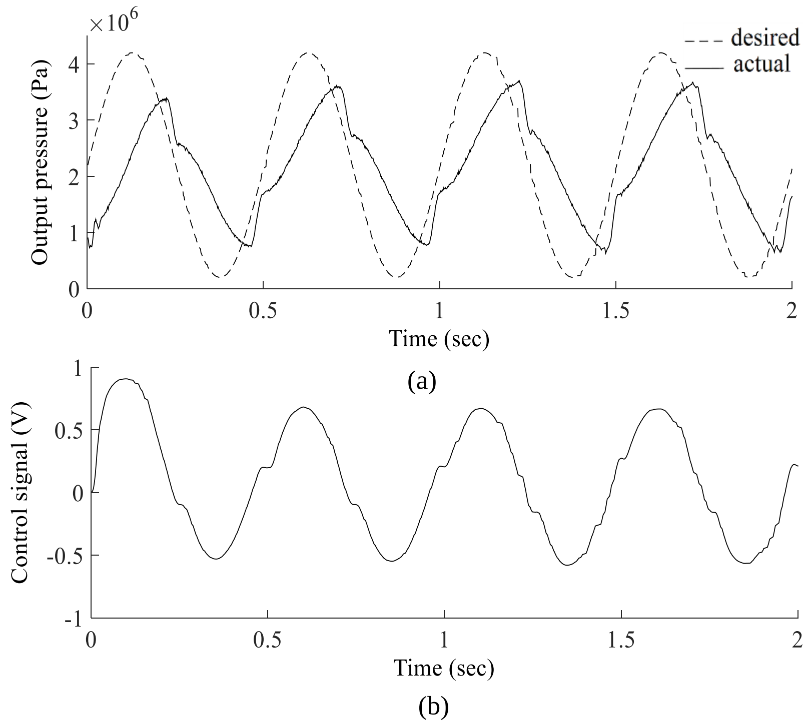

Figure 5.13. (a) 2 Hz sinusoidal output pressure tracking; (b) corresponding control signal.

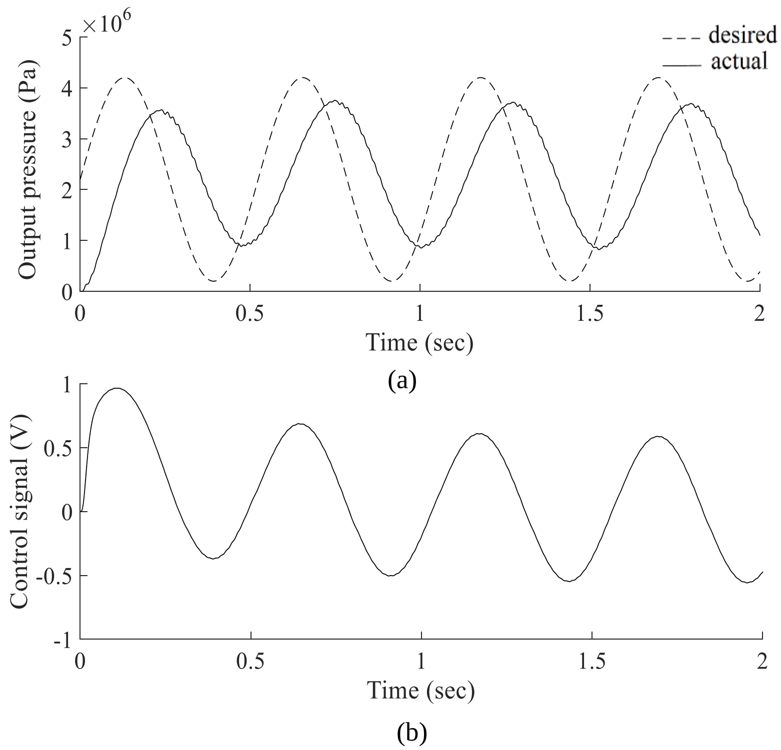

Figure 5.14. Simulation results: (a) 2 Hz sinusoidal output pressure tracking; (b) corresponding control signal.

5.3 Increasing Tracking Bandwidth

5.3.1 Challenges

In order to achieve the pressure tracking bandwidth higher than 2 Hz, the tracking bounds should be re-defined. This will result in new QFT bounds and designing a new QFT controller and pre-filter. However, the process is not straightforward and introduces a number of challenges. The main challenge in increasing the pressure tracking bandwidth originates from the natural velocity feedback in the hydraulic actuation function. Thus, first the effect of the natural velocity feedback on bandwidth is explained, followed by a discussion on trade-off among different performance criteria to achieve optimum responses.

Figure 5.15 shows the two-degree-of-freedom of QFT control system of hydraulic actuator using controller $C_1(s)$ and pre-filter $F_1(s)$ given by equations (5.12) and (5.13). In this block diagram the relationship between the output pressure P_L and the actuator position x_p is shown by transfer function $G_e(s)$.

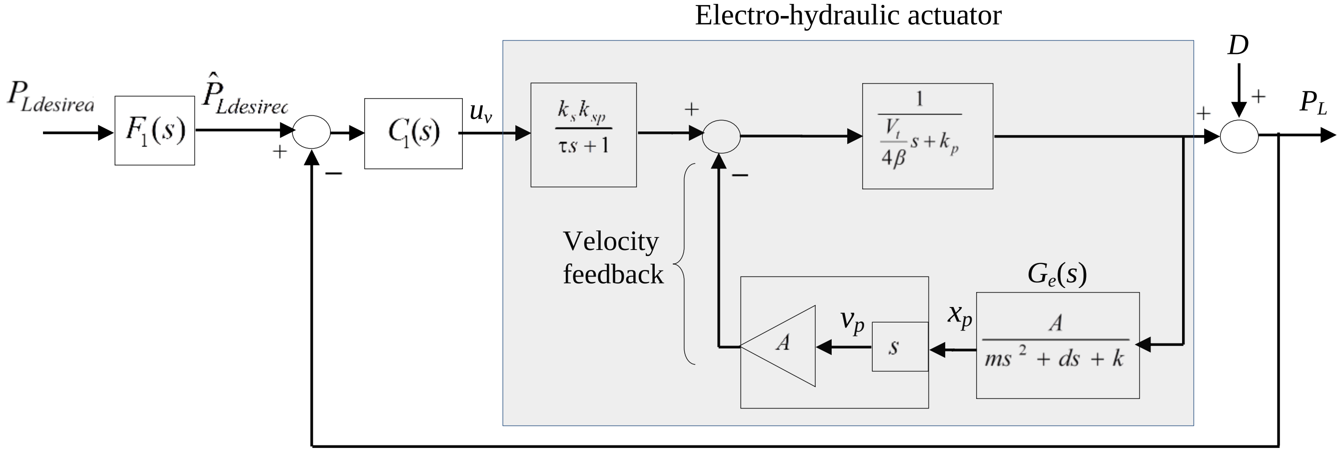

Figure 5.15. Detailed block diagram of actuator-environment dynamics and control system.

The positions of the poles of $G_e(s)$ depend on the parameters m, d and k. These poles appear as zeros in the open-loop transfer function of the system given by equation (5.5). For lightly damped environments, these zeros are located near the imaginary axis, resulting in a drop in the frequency response magnitude of the output pressure. This drop, which occurs at the natural frequency of the environment ($\sqrt{\frac{k}{m}}$), also known as the anti-resonance frequency, limits the pressure tracking bandwidth of the actuator (Sivaselvan et al., 2008; Alleyne and Liu, 1999; Lamming, 2009). This is clearly seen from Figure 5.3 where the frequency response magnitudes of the closed-loop transfer functions drop at a frequency within [70 105] rad/sec, depending on the values for m and k given in Table 2.1. This drop, which is closely related to the parameters of the environment, was covered by the lower tracking bound in Section 5.2 (see equation (5.11)), limits subsequently the closed-loop bandwidth to 2 Hz.

Changing the pressure tracking bounds for increased bandwidth, leads to a shift in the magnitude of the closed-loop frequency responses for the family of transfer functions. It also changes the locations of the closed-loop poles. For example, Figure 5.16 shows the root locus plot of dominant complex poles for the block diagram shown in Figure 5.15 for the nominal values given in Table 2.1. Note that open-loop zeros are the poles of the environments. An upward shift in the frequency response translates into moving the closed-loop poles from their initial position along the direction shown by the arrows in Figure 5.16. While, the relocated closed-loop poles increase the tracking bandwidth, the corresponding damping ratio, ξ is reduced causing the transient response to exhibit more overshoot.

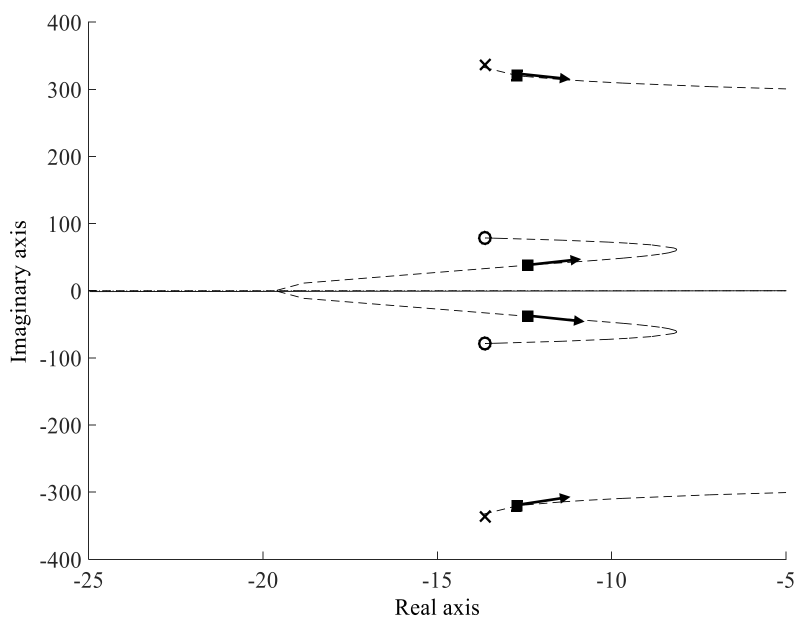

Figure 5.16. Close-up view of root locus around dominant closed-loop complex poles.

Furthermore, the real parts of the complex poles, i.e., $\xi\omega$, decreases leading to longer settling time. Thus, new tracking bounds must be defined to allow overshoot and longer settling time - a compromise towards increasing the bandwidth.

Another consideration when increasing the output pressure tracking bandwidth is to observe the sensitivity of the control system to output disturbances. Figure 5.17 compares the frequency response magnitude of the sensitivity transfer function, for the nominal plant and the QFT controller (5.12), with the one having its closed-loop poles relocated for increased bandwidth (see Figure 5.16).

From Figure 5.17, the sensitivity of the system with higher bandwidth is less at low frequencies (which is expected). However, less sensitivity at low frequencies is accompanied by higher sensitivity peaks at high frequencies due to the "waterbed effect" (Houpis et al., 2005). High sensitivity decreases the closed-loop stability margin. Therefore, careful selection of the sensitivity upper bound is important. Unnecessary low upper bound for the sensitivity, limits the maximum achievable bandwidth through the QFT design process while a thoughtless design with high upper bound for sensitivity can jeopardize the stability of the system.

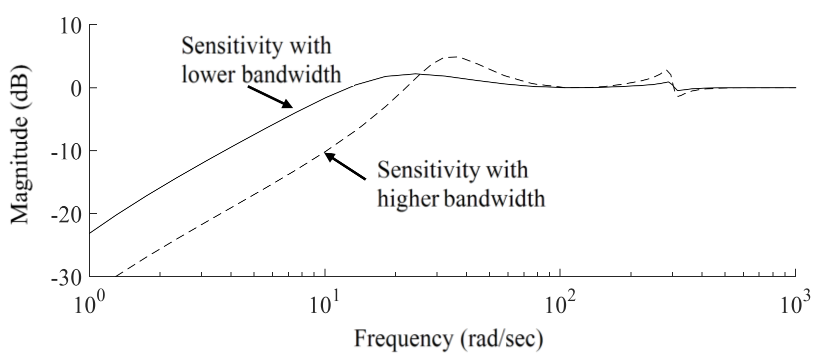

Figure 5.17. Sensitivity magnitude corresponding to closed-loop poles in Figure 5.14 (solid line), and after relocating closed-loop poles in Figure 5.14 (dashed line).

From the above discussion, in order to design a QFT controller with increased output pressure tracking bandwidth, first, new tracking bounds should incorporate higher overshoot and longer settling time. Second, higher sensitivity can be permitted as long as the stability and robustness of the closed-loop system are not jeopardized.

5.3.2 Controller Design

Applying the results of the discussion in Section 5.3.1, to achieve higher tracking bandwidth, new tracking bounds are defined by equations (5.14) and (5.15). These bounds allow the system to have the overshoot from 0% up to 23% and the longer settling time within 0.1-0.9 sec for the step response as shown in Figure 5.18. Given these new tracking bounds, the bandwidth of 3Hz and more is expected (see equation (5.15)).

$$T_u(s) = \frac{1.7\times 10^4 (s+2.2)}{(s+2.8)(s+90)(s+150)} \tag{5.14}$$

$$T_l(s) = \frac{42000}{(s+35)^3} \tag{5.15}$$

The constraints for the robust closed-loop stability and output disturbance rejection are kept the same as equations (5.7) and (5.8), respectively.

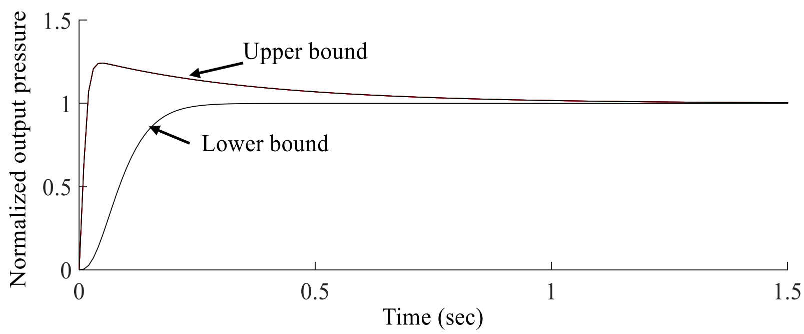

Figure 5.18. Time responses of new tracking bounds.

Employing the new performance criteria and after loop-shaping process, shown in Figure 5.19, the following QFT controller and pre-filter are designed:

$$C_2(s) = \frac{8(s+2.1)}{s(s+210)(s^2+223s+50000)} \tag{5.16}$$

$$F_2(s) = \frac{9\times 10^5 (s+8)}{(s+180)(s+150)(s+270)} \tag{5.17}$$

Figure 5.20 shows the frequency responses of the closed-loop system and the corresponding sensitivity using controller (5.16) and pre-filter (5.17) for parameter values given in Table 2.1.

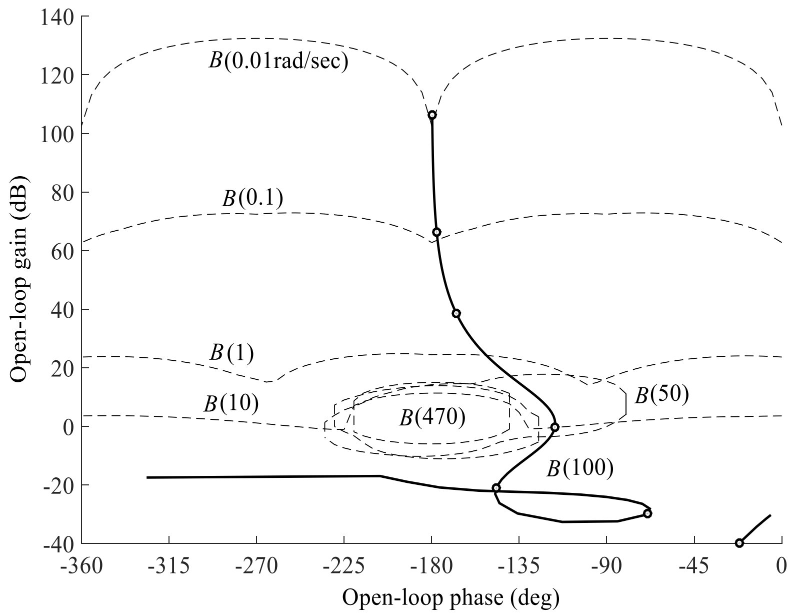

Figure 5.19. QFT bounds on Nichols chart with nominal loop transmission function with controller (5.16).

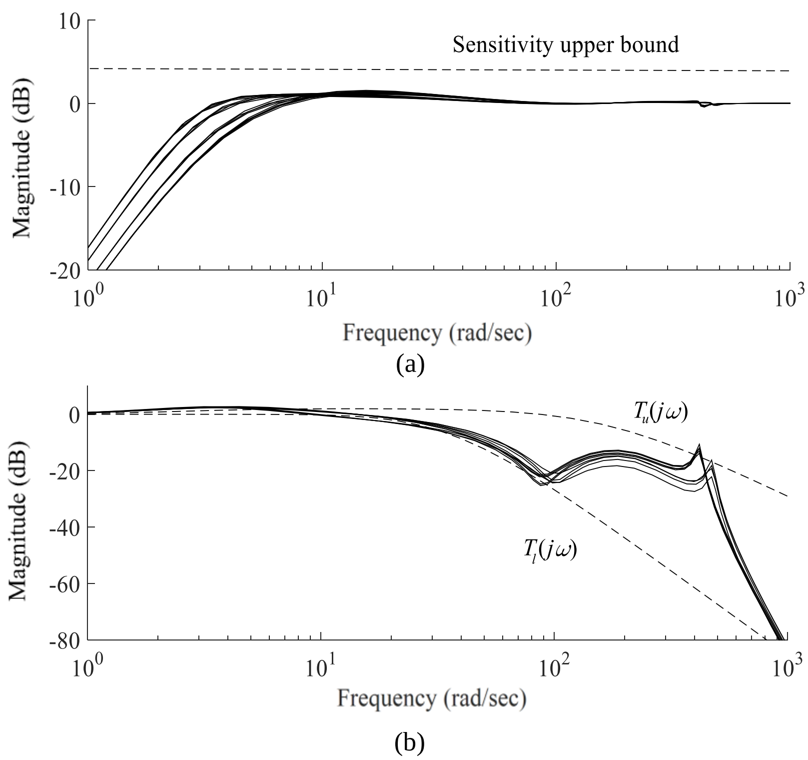

Figure 5.20. (a) Frequency responses of sensitivity; (b) corresponding frequency response of closed-loop system, using controller (5.16) and pre-filter (5.17) for entire range of parametric uncertainties given in Table 2.1.

5.3.3 Experimental Validation

In this section, the experimental results of applying the controller (5.16) and the pre-filter (5.17) on the electro-hydraulic actuator are presented. Figure 5.21 shows the output pressure tracking performance of the hydraulic actuator given different desired step inputs of amplitudes 1 MPa, 2 MPa, 3 MPa, 4 MPa and 5 MPa. The corresponding control signals are also shown. Figure 5.19 shows the overshoot (22%) and settling time (1 sec) of the responses are increased as compared with the step responses shown for the first design (see Figure 5.10). Figures 5.22 and 5.24 show the system response in tracking of a sinusoidal input with the peak-to-peak amplitude of 4 MPa and frequencies of 5 and 6 Hz, respectively. The closed-loop system successfully tracks the desired output pressure of 5 Hz. In tracking the input signal of 6 Hz, the magnitude of the output pressure is attenuated more but is still within 80% of the desired magnitude. The corresponding simulation results for inputs of 5 and 6 Hz are shown in Figures 5.23 and 5.25, respectively. As a result, the increase in the closed-loop tracking bandwidth with adequate margin of stability was possible for the same environment as in the previous test (see Section 5.2) at the expense of an increased overshoot of 22% and longer settling time of 1 sec for tracking step inputs.

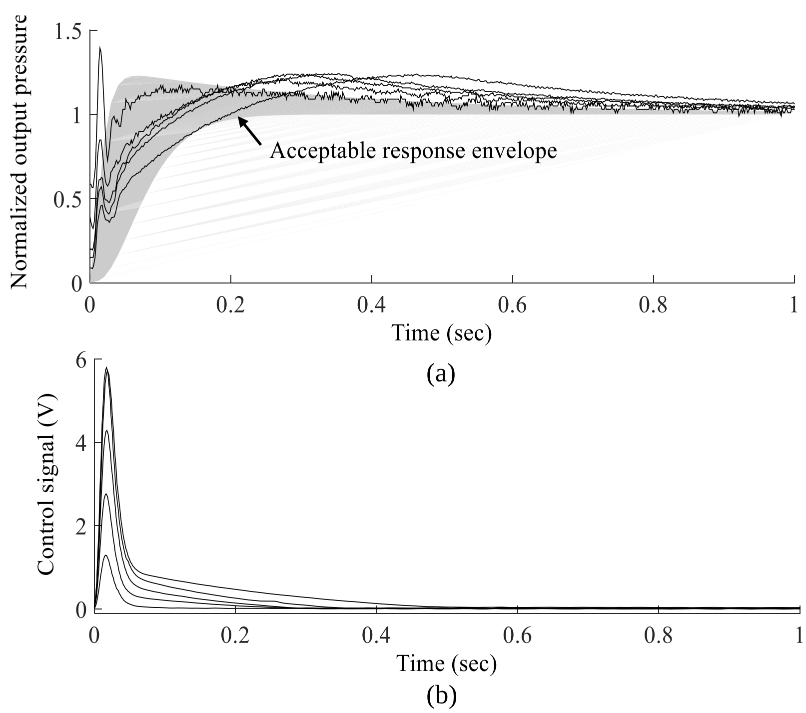

Figure 5.21. (a) Normalized output pressure responses in tracking of different step inputs (1-5 MPa); (b) corresponding control signals.

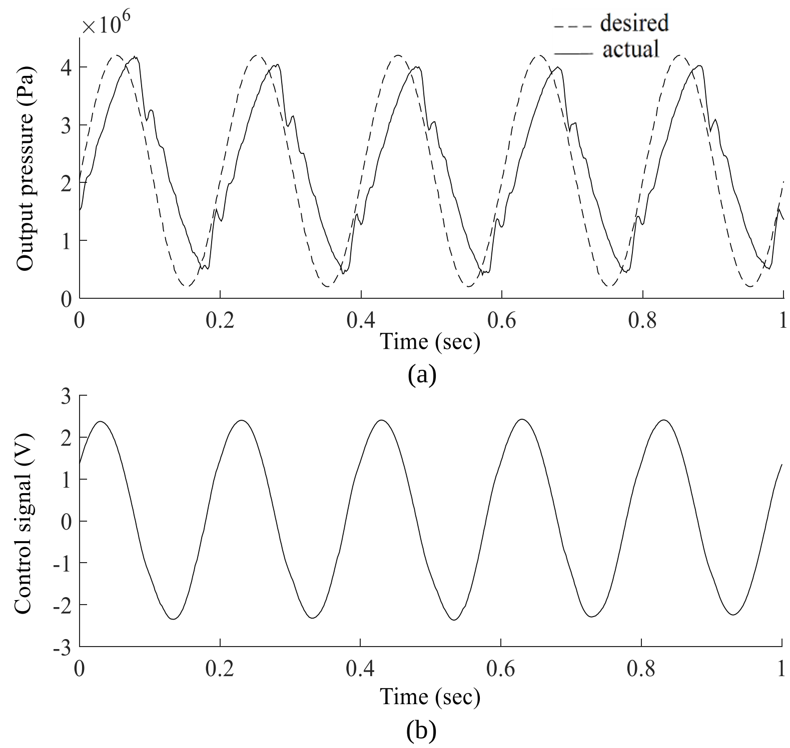

Figure 5.22. (a) 5 Hz sinusoidal output pressure tracking; (b) corresponding control signal.

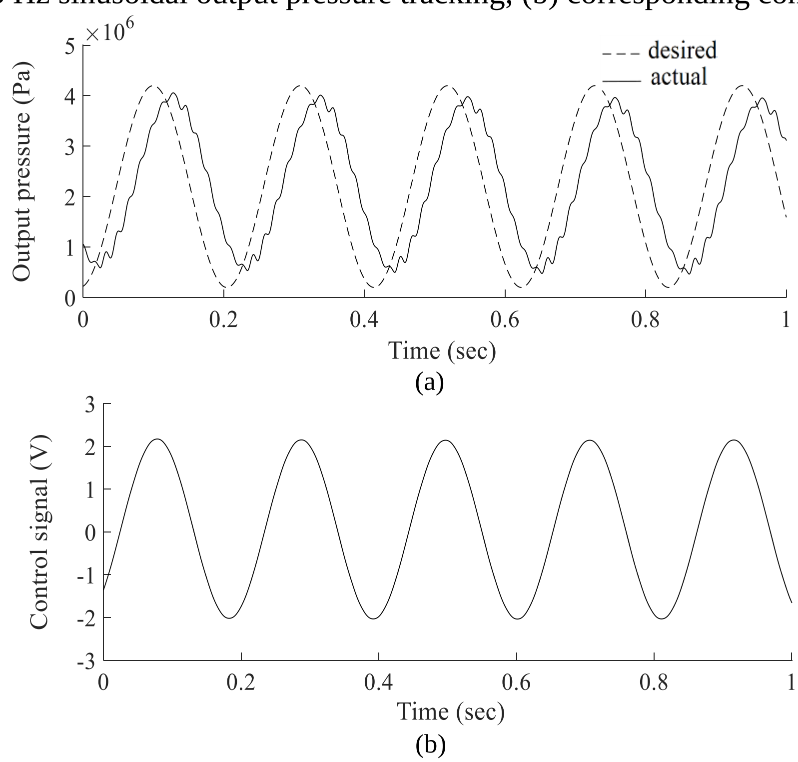

Figure 5.23. Simulation results: (a) 5 Hz sinusoidal output pressure tracking; (b) corresponding control signal.

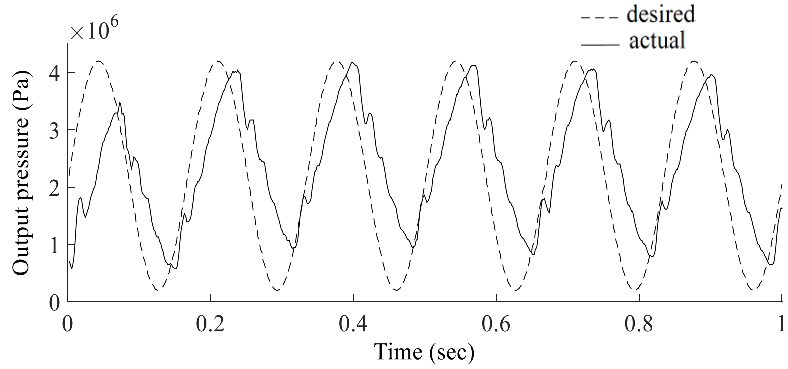

(a)

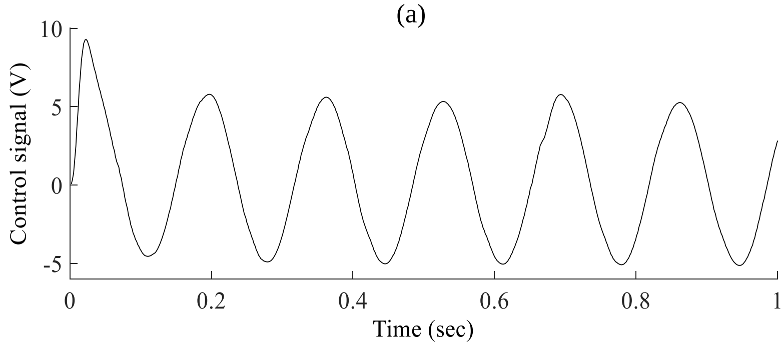

(b)

Figure 5.24. (a) 6 Hz sinusoidal output pressure tracking; (b) corresponding control signal.

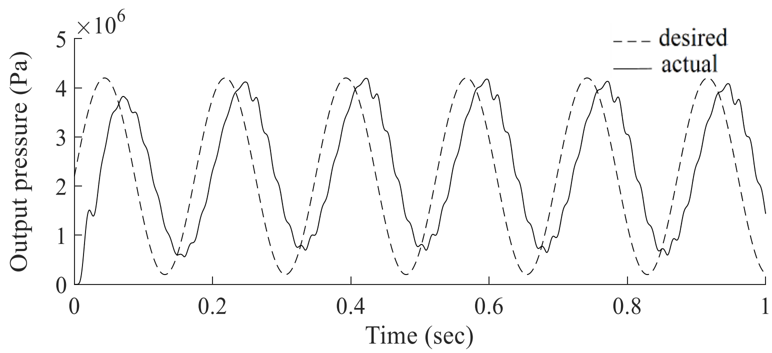

(a)

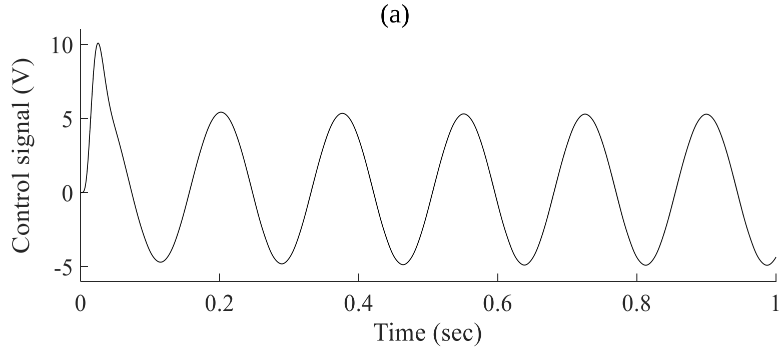

(b)

Figure 5.25. Simulation results: (a) 6 Hz sinusoidal output pressure tracking; (b) corresponding control signal.

5.4 Stability Analysis

In previous sections, two QFT control systems were designed to provide a comprehensive discussion on the performance of the closed-loop system. These controllers were designed based on a linearized model of the nonlinear hydraulic system around some operating points. Therefore, the stability of the resulting closed-loop system is limited over these particular sets of operating points, i.e., in a small-signal sense (Horowitz, 1976). To alleviate this limitation, in this section, the nonlinear stability of the QFT control systems are investigated using T-S fuzzy modeling and its stability theorem, explained in Chapter 4.

5.4.1 T-S Fuzzy Model of Electro-Hydraulic Actuator

For the stability analysis, first a T-S fuzzy model of the electro-hydraulic actuator under study is required. This model was derived in Section 4.3.2 and is used here. All the uncertain parameters in Table 2.1, should be incorporated in the T-S fuzzy model (4.21)-(4.22), using the procedure, explained in Section 4.3.2. These parameters are the bulk modulus (β), total mass (m), total damping (d), stiffness of the environment (k), valve spool gain (k_{sp}), and valve time constant (τ). In addition, uncertainty in the identified friction parameters σ_0, σ_1, F_s, F_c, α_f, and v_s, as well as the total leakage coefficient k_T are incorporated in the T-S fuzzy model. The resultant T-S fuzzy model of the double-rod hydraulic actuator in the presence of the above parametric uncertainties is as follows:

$$\begin{aligned}\dot{\vec{\boldsymbol{x}}}(t) = \sum_{i=1}^{2}\cdots\sum_{\varsigma=1}^{2} & G_i(z_1(t))\Gamma_\gamma(z_2(t))S_l(k)N_n(d)M_r(m)H_j(\beta) \\ & \times R_\kappa(k_T)W_w(k_{sp})Y_y(\tau)\Sigma_\nu(\sigma_0)\Lambda_\varsigma(\sigma_1)\left(\boldsymbol{A}_{i\gamma lnrj\kappa wy\nu\varsigma}\vec{\boldsymbol{x}}(t) + \boldsymbol{B}_{i\gamma lnrj\kappa wy\nu\varsigma}u_v\right)\end{aligned} \tag{5.18}$$

The summations in (5.18) can be aggregated as follows:

$$\dot{\vec{\boldsymbol{x}}}(t) = \sum_{\rho=1}^{2048}\left(q_\rho\left(z(t)\right)\right)\left(\boldsymbol{A}_\rho^*\vec{\boldsymbol{x}}(t) + \boldsymbol{B}_\rho^* u_v\right) \tag{5.19}$$

where $\boldsymbol{A}_\rho^*$, $\boldsymbol{B}_\rho^*$, $q_\rho(z(t))$, and ρ are as follows:

$$\boldsymbol{A}_{\rho}^{*} = \boldsymbol{A}_{i\gamma lnrj\kappa wy\nu\varsigma} = \begin{bmatrix} 0 & 1 & 0 & 0 & 0 \\ \dfrac{-k_l}{m_r} & \dfrac{-(\sigma_{1_\varsigma} + d_n)}{m_r} & \dfrac{A}{m_r} & 0 & \dfrac{-(\sigma_{0_\nu} - \sigma_{0_\nu}\sigma_{1_\varsigma}\delta_\gamma)}{m_r} \\ 0 & -\dfrac{4\beta_j}{V_t}A & -\dfrac{4\beta_j}{V_t}k_{T_\kappa} & \dfrac{4\beta_j}{V_t}g_i & 0 \\ 0 & 0 & 0 & \dfrac{-1}{\tau_y} & 0 \\ 0 & 1 & 0 & 0 & -\sigma_{0_\nu}\delta_\gamma \end{bmatrix} \tag{5.20a}$$

$$\boldsymbol{B}_{\rho}^{*} = \boldsymbol{B}_{i\gamma lnrj\kappa wy\nu\varsigma} = \begin{bmatrix} 0 & 0 & 0 & \dfrac{k_{sp_w}}{\tau_y} & 0 \end{bmatrix}^{\mathrm{T}} \tag{5.20b}$$

$$q_\rho(z(t)) = G_i(z_1(t))\Gamma_\gamma(z_2(t))S_l(k)N_n(d)M_r(m)H_j(\beta)R_\kappa(k_T)W_w(k_{sp})Y_y(\tau)\Sigma_\nu(\sigma_0)\Lambda_\varsigma(\sigma_1) \tag{5.20c}$$

$$\rho = \varsigma + 2(\nu - 1) + 4(y-1) + 8(w-1) + 16(\kappa - 1) + 32(j-1) + 64(r-1) + 128(n-1) + 256(l-1) + 512(\gamma - 1) + 1024(i-1) \tag{5.20d}$$

In equation (5.19), the total number of local linear models is 2048, which is obtained using the formulation of ρ in (5.20d). Membership functions $S_l(k)$, $N_n(d)$, $M_r(m)$, $H_j(\beta)$, $R_\kappa(k_T)$, $W_w(k_{sp})$, $Y_y(\tau)$, $\Sigma_\nu(\sigma_0)$, $\Lambda_\varsigma(\sigma_1)$ are related to the stiffness k, total damping d, total mass m, bulk modulus β, total leakage coefficient k_T, valve gain k_{sp}, valve time constant τ, and friction parameters σ_0 and σ_1. Uncertainties related to parameters F_s, F_c, α_f, and v_s are considered in calculations of δ_γ.

5.4.2 Stability of Closed-Loop System

After developing a T-S fuzzy model for the electro-hydraulic actuator, now the state-space equations of the QFT controllers in time-domain are added to present the closed-loop system with one T-S fuzzy model. This state-space model can be calculated manually using the instructions in (Rowell, 2002) or using MATLAB. Figure 5.22 shows the closed-loop structure of the output pressure control system using the state-space representation of the controllers as follows:

$$\begin{aligned} \dot{\vec{\boldsymbol{x}}}_c &= \boldsymbol{A}_c\vec{\boldsymbol{x}}_c + \boldsymbol{B}_c e_{P_L} \\ u_v &= \boldsymbol{C}_c\vec{\boldsymbol{x}}_c \end{aligned} \tag{5.21}$$

where $\boldsymbol{A}_c$, $\boldsymbol{B}_c$, and $\boldsymbol{C}_c$ are as follows for each controller:

$$C_1(s) = \frac{18(s+0.75)}{s(s+210)(s^2+312s+50000)} \Rightarrow \boldsymbol{A}_c = \begin{bmatrix} -433 & -96830 & -10^7 & 0 \\ 1 & 0 & 0 & 0 \\ 0 & 1 & 0 & 0 \\ 0 & 0 & 1 & 0 \end{bmatrix}, \boldsymbol{B}_c = \begin{bmatrix} 1 \\ 0 \\ 0 \\ 0 \end{bmatrix}, \boldsymbol{C}_c = \begin{bmatrix} 0 \\ 0 \\ 8 \\ 16 \end{bmatrix}^{\mathrm{T}} \tag{5.22}$$

$$C_2(s) = \frac{8(s+2.1)}{s(s+210)(s^2+223s+50000)} \Rightarrow \boldsymbol{A}_c = \begin{bmatrix} -522 & -115520 & -10^7 & 0 \\ 1 & 0 & 0 & 0 \\ 0 & 1 & 0 & 0 \\ 0 & 0 & 1 & 0 \end{bmatrix}, \boldsymbol{B}_c = \begin{bmatrix} 1 \\ 0 \\ 0 \\ 0 \end{bmatrix}, \boldsymbol{C}_c = \begin{bmatrix} 0 \\ 0 \\ 18 \\ 13 \end{bmatrix}^{\mathrm{T}} \tag{5.23}$$

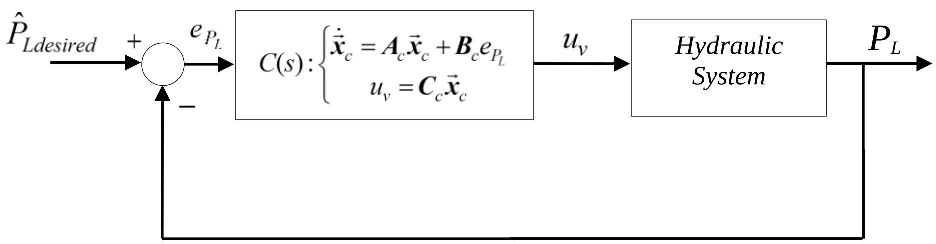

Figure 5.26. Control loop of output pressure of electro-hydraulic actuator for stability analysis.

Note that for the stability analysis, the pre-filter $F(s)$ is not considered. Referring to Figure 5.22, the following equations represent the closed-loop system:

$$\begin{cases} \dot{\vec{x}}(t) = \sum_{\rho=1}^{2048} \left(q_\rho(z(t))\right)\left(\boldsymbol{A}_\rho^* \vec{x}(t) + \boldsymbol{B}_\rho^* \boldsymbol{C}_c \vec{x}_c\right) & \text{(5.24a)} \\ \dot{\vec{x}}_c = \boldsymbol{A}_c \vec{x}_c + \boldsymbol{B}_c(\hat{P}_{Ldesired} - P_L) & \text{(5.24b)} \end{cases}$$

To derive equations (5.24), e_{P_L} was substituted as $\hat{P}_{Ldesired} - P_L$. Since $\sum_{\rho=1}^{2048}\left(q_\rho(z(t))\right) = 1$, the above equations can be combined as follows:

$$\begin{bmatrix} \dot{\vec{x}} \\ \dot{\vec{x}}_c \end{bmatrix} = \sum_{\rho=1}^{2048} q_\rho(z(t)) \left(\begin{pmatrix} \boldsymbol{A}_\rho^* & \boldsymbol{B}_\rho^* \boldsymbol{C}_c \\ -\boldsymbol{B}_c[0 \quad 0 \quad 1 \quad 0 \quad 0] & \boldsymbol{A}_c \end{pmatrix} \begin{bmatrix} \vec{x} \\ \vec{x}_c \end{bmatrix} + \begin{bmatrix} (0)_{5\times 1} \\ \boldsymbol{B}_c \end{bmatrix} \hat{P}_{Ldesired} \right) \tag{5.25}$$

To investigate the stability of the closed-loop system presented by T-S fuzzy model of (5.25), the stability theorem in Section 4.2.2 is used. First by solving

$\begin{bmatrix}\dot{\vec{x}}^{\mathrm{T}} & \dot{\vec{x}}_c^{\mathrm{T}}\end{bmatrix}^{\mathrm{T}} = \begin{bmatrix}\dot{x}_p & \dot{v}_p & \dot{P}_L & \dot{x}_v & \dot{\eta} & \dot{x}_{c1} & \cdots & \dot{x}_{c\lambda}\end{bmatrix}^{\mathrm{T}} = 0$, the equilibrium point of the closed-loop system should be obtained. However, the presence of leakage term $k_T P_L$ does not allow deriving explicit values for the equilibrium point of the electro-hydraulic closed-loop system. On the other hand, internal leakage flow has inherent stabilizing effect by providing damping for hydraulic resonant mode, thus, for the rest of the analysis, the leakage term $k_T P_L$ is omitted (Vossoughi and Donath, 1995). As a result, the following equilibrium point is obtained:

$$\begin{bmatrix}\vec{x}_{eq}^{\mathrm{T}} & \vec{x}_{ceq}^{\mathrm{T}}\end{bmatrix} = \begin{bmatrix}\dfrac{A\hat{P}_{Ldesired}}{k} & 0 & \hat{P}_{Ldesired} & 0 & 0 & x_{ceq1} & \cdots & x_{ceq\lambda}\end{bmatrix} \tag{5.26}$$

The above equilibrium point is not at the origin; therefore by defining $\vec{e} = \vec{x} - \vec{x}_{eq}$ and $\vec{e}_c = \vec{x}_c - \vec{x}_{ceq}$, the following error dynamic equations are derived:

$$\begin{bmatrix}\dot{\vec{e}} \\ \dot{\vec{e}}_c\end{bmatrix} = \sum_{\rho=1}^{1024} q_\rho(z(t)) \underbrace{\begin{pmatrix} \boldsymbol{A}_\rho^* & \boldsymbol{B}_\rho^* \boldsymbol{C}_c \\ -\boldsymbol{B}_c\begin{bmatrix}0 & 0 & 1 & 0 & 0\end{bmatrix} & \boldsymbol{A}_c \end{pmatrix}}_{\boldsymbol{A}_{closed-loop}} \begin{bmatrix}\vec{e} \\ \vec{e}_c\end{bmatrix} \tag{5.27}$$

where $\boldsymbol{A}_{closed\text{-}loop}$ is as follows:

$$\boldsymbol{A}_{closed-loop} = \begin{bmatrix}
0 & 1 & 0 & 0 & 0 & [0]_{1\times\lambda} \\
\dfrac{-k_l}{m_r} & \dfrac{-(\sigma_{1_\varsigma} + d_n)}{m_r} & \dfrac{A}{m_r} & 0 & \dfrac{-(\sigma_{0_\nu} - \sigma_{0\nu}\sigma_{1\varsigma}\delta_\gamma)}{m_r} & [0]_{1\times\lambda} \\
0 & -\dfrac{4\beta_j}{V_t}A & 0 & \dfrac{4\beta_j}{V_t}g_i & 0 & [0]_{1\times\lambda} \\
0 & 0 & 0 & \dfrac{-1}{\tau_y} & 0 & \dfrac{k_{sp_w}}{\tau_y}[\boldsymbol{C}_c]_{1\times\lambda} \\
0 & 1 & 0 & 0 & -\sigma_{0\nu}\delta_\gamma & [0]_{1\times\lambda} \\
[0]_{\lambda\times1} & [0]_{\lambda\times1} & -[\boldsymbol{B}_c]_{\lambda\times1} & [0]_{\lambda\times1} & [0]_{\lambda\times1} & [\boldsymbol{A}_c]_{\lambda\times\lambda}
\end{bmatrix} \tag{5.28}$$

For controllers $C_1(s)$ and $C_2(s)$, with state-space representations in (5.22) and (5.23), λ=4. By substituting $\boldsymbol{A}_c$, $\boldsymbol{B}_c$, $\boldsymbol{C}_c$ from (5.22) and (5.23), the stability LMIs are constructed based on conditions (4.6) and (4.7). However, the feasibility is not achievable for these LMIs. Instead for f_f=0, the LMIs become feasible. With f_f=0, the error dynamics are as follows:

$$\begin{bmatrix}\dot{\vec{e}} \\ \dot{\vec{e}}_c\end{bmatrix} = \sum_{\rho=1}^{128} q_\rho(z(t)) \underbrace{\begin{pmatrix} \boldsymbol{A}_\rho^* & \boldsymbol{B}_\rho^* \boldsymbol{C}_c \\ -\boldsymbol{B}_c\begin{bmatrix}0 & 0 & 1 & 0\end{bmatrix} & \boldsymbol{A}_c \end{pmatrix}}_{\boldsymbol{A}_{closed-loop}} \begin{bmatrix}\vec{e} \\ \vec{e}_c\end{bmatrix} \tag{5.29}$$

where $q_\rho(z(t))$, ρ, and $A_{closed\text{-}loop}$ are:

$$q_{\rho}(z(t)) = G_i(z_1(t))S_l(k)N_n(d)M_r(m)H_j(\beta)W_w(k_{sp})Y_y(\tau) \tag{5.30a}$$

$$\rho = y + 2(w-1) + 4(j-1) + 8(r-1) + 16(n-1) + 32(l-1) + 64(i-1) \tag{5.30b}$$

$$\boldsymbol{A}_{closed-loop} = \begin{bmatrix} 0 & 1 & 0 & 0 & [0]_{1\times\lambda} \\ \dfrac{-k_l}{m_r} & \dfrac{-d_n}{m_r} & \dfrac{A}{m_r} & 0 & [0]_{1\times\lambda} \\ 0 & -\dfrac{4\beta_j}{V_t}A & 0 & \dfrac{4\beta_j}{V_t}g_i & [0]_{1\times\lambda} \\ 0 & 0 & 0 & \dfrac{-1}{\tau_y} & \dfrac{k_{sp_w}}{\tau_y}[\boldsymbol{C}_c]_{1\times\lambda} \\ [0]_{\lambda\times 1} & [0]_{\lambda\times 1} & -[\boldsymbol{B}_c]_{\lambda\times 1} & [0]_{\lambda\times 1} & [\boldsymbol{A}_c]_{\lambda\times\lambda} \end{bmatrix} \tag{5.30c}$$

In equation (5.30c), the values of $g_{i(i=1,2)}$ for $P_L \in [-(2/3)P_s \quad (2/3)P_s]$, are obtained as follows:

$$g_1 = \max(z_1(t)) = \max(\frac{K_v w}{\sqrt{2}}\sqrt{P_s - \mathrm{sgn}(x_v)P_L}) = \frac{K_v w}{\sqrt{2}}\sqrt{17.2\,\mathrm{MPa} + (\frac{2}{3}\times 17.2)\,\mathrm{MPa}} = 2.182\sqrt{\frac{\mathrm{m}^5\mathrm{Pa}}{\mathrm{kg}}} \tag{5.31a}$$

$$g_2 = \min(z_1(t)) = \min(\frac{K_v w}{\sqrt{2}}\sqrt{P_s - \mathrm{sgn}(x_v)P_L}) = \frac{K_v w}{\sqrt{2}}\sqrt{17.2\,\mathrm{MPa} - (\frac{2}{3}\times 17.2)\,\mathrm{MPa}} = 1.023\sqrt{\frac{\mathrm{m}^5\mathrm{Pa}}{\mathrm{kg}}} \tag{5.31b}$$

where K_v and w are substituted from Table 2.1. Note that the range for the load pressure ($\pm 2/3P_s$), is specified according to (Merritt, 1967). The LMIs constructed based on $A_{closed\text{-}loop}$ in equation (5.30c), become feasible for a smaller uncertainty range of the parameters that QFT controllers were initially designed for. Table 5.3 lists these ranges along with the ranges that QFT controllers were initially designed for. Following positive definite matrices are found to satisfy the stability conditions (4.6) and (4.7) for system (5.29)-(5.30) with controllers $C_1(s)$ and $C_2(s)$ respectively, and for the parameter values given in Table 5.3:

Table 5.3. Range of parametric uncertainties with feasible LMIs for electro-hydraulic pressure control system.

Parameter	Range in QFT design	Range for feasible LMIs using QFT controllers $C_1(s)$ and $C_2(s)$
Total mass, m (kg)	10-14	10.9-11.1
Total damping, d (N.sec/m)	200-400	200-400
Fluid bulk modulus, β (MPa)	650-700	690-710
Spool position gain, k_{sp} (μm/V)	23.1-27	23.1-30
Load stiffness, k (kN/m)	70-130	100-130
Valve time constant, τ (sec)	0.002-0.0026	0.0022

$$P_1 = 10^5 \begin{bmatrix} 0.0464 & 0.0034 & 0.0127 & 0.0506 & 0.0569 & 0.0683 & 0.0706 & -0.0862 \\ 0.0034 & 0.0130 & 0.0008 & 0.0162 & 0.0773 & 0.0788 & 0.0592 & 0.0008 \\ 0.0127 & 0.0008 & 0.0142 & 0.0155 & 0.0191 & 0.0180 & 0.0143 & -0.0282 \\ 0.0506 & 0.0162 & 0.0155 & 0.2134 & 0.3429 & 0.3626 & 0.3315 & -0.1030 \\ 0.0569 & 0.0773 & 0.0191 & 0.3429 & 1.1831 & 1.1818 & 0.9336 & -0.0010 \\ 0.0683 & 0.0788 & 0.0180 & 0.3626 & 1.1818 & 1.2320 & 0.9935 & -0.0085 \\ 0.0706 & 0.0592 & 0.0143 & 0.3315 & 0.9336 & 0.9935 & 0.8947 & -0.0168 \\ -0.0862 & 0.0008 & -0.0282 & -0.1030 & -0.0010 & -0.0085 & -0.0168 & 1.2078 \end{bmatrix} \tag{5.32}$$

$$P_2 = \begin{bmatrix} 5.0142 & 0.3911 & 1.0111 & 5.3136 & 6.1918 & 5.7276 & 5.3982 & -6.3564 \\ 0.3911 & 3.0607 & 0.0823 & -0.2766 & 4.0931 & 3.5263 & 2.1094 & 0.5830 \\ 1.0111 & 0.0823 & 3.8366 & 1.8046 & 2.1373 & 1.3588 & 0.8253 & -2.1267 \\ 5.3136 & -0.2766 & 1.8046 & 10.9321 & 12.8644 & 11.1383 & 10.0863 & -6.2652 \\ 6.1918 & 4.0931 & 2.1373 & 12.8644 & 57.0772 & 47.3457 & 33.3460 & 8.9289 \\ 5.7276 & 3.5263 & 1.3588 & 11.1383 & 47.3457 & 44.0663 & 33.2656 & 7.2778 \\ 5.3982 & 2.1094 & 0.8253 & 10.0863 & 33.3460 & 33.2656 & 33.0391 & 6.1634 \\ -6.3564 & 0.5830 & -2.1267 & -6.2652 & 8.9289 & 7.2778 & 6.1634 & 70.8886 \end{bmatrix} \tag{5.33}$$

5.5 Summary

QFT was employed to design a robust control scheme for the output pressure of the electro-hydraulic actuator. Besides achieving desired pressure tracking bandwidth, the QFT controller satisfied other performance criteria, i.e., closed-loop stability, disturbance rejection, and desired transient time response. It was shown how assuring these criteria could conflict with increasing the bandwidth. The nature of the trade-off was discussed and results were incorporated in the controller design. Experimental results were provided to substantiate the theoretical developments. Accordingly, the QFT controller adequately satisfied closed-loop performance criteria, and achieved the bandwidth of 6 Hz for the pressure tracking. After design and experimentally verification of QFT controllers, the nonlinear stability of the closed-loop systems were proven using T-S fuzzy modeling and its stability approach, explained in Chapter 4. This analysis was done considering uncertainty in the actuator and environment parameters.

Chapter 6

Output Pressure Control of Electro-Hydrostatic Actuator

In this chapter, a robust, fixed-gain, and linear output pressure controller is designed for the double-rod electro-hydrostatic actuator using QFT. First, the family of frequency responses of the system is identified by applying an advanced form of fast Fourier transform on the open-loop input-output experimental data, in Section 6.1. This approach results in realistic frequency responses, prevents generation of unnecessary large templates, and consequently contributes to the design of a low-order QFT controller. The designed controller in Section 6.2 provides desired transient responses, desired tracking bandwidth, robust stability and disturbance rejection for the closed-loop system. Experimental results in Section 6.3 confirm the performance of the QFT controller. The controller, however, only guarantees the closed-loop stability for the family of frequency responses obtained given specific operating conditions. In order to further investigate the stability for a wider range of uncertainties, T-S fuzzy modeling and its stability theory are employed. The T-S fuzzy model is derived for the closed-loop system and the stability conditions are presented as linear matrix inequalities (LMIs). Feasible LMIs are found for the closed-loop system covering a wide and continuous range of uncertainties, including the presence of friction and leakages.

6.1 Family of Frequency Responses

To derive the family of frequency responses of the electro-hydrostatic actuator from the dynamic equations, presented in equations (2.11)-(2.16), the uncertainty ranges of the system parameter are required. However, employing identification methods to estimate the variation range of parameters is not in the scope of this research. One alternative solution is to employ frequency domain identification method, which is built upon an advanced form of fast Fourier transform, implemented in software, called CIFER (Tischler and Remple, 2012). Standard Fourier transformation has been used before to obtain frequency responses of an electro-hydraulic actuator, where only the simulation input-output data was employed (Karpenko and Sepehri, 2008). The advanced form of fast Fourier transform uses Chirp-Z transform and composite optimal window techniques, results in frequency responses with better quality as compared with the results of standard fast Fourier transform (Tischler and Remple, 2012). Furthermore, the method is applied to experimental data, which results in more accurate frequency response representation of the real system. The experimental output pressure data is obtained by exciting the test-rig with a linear chirp input signal, described by the following form (Annus et al., 2012):

$$A_{chirp} \sin\left(2\pi(f_0 + \frac{f_1 - f_0}{t_1}t)t\right) \tag{6.1}$$

where f_0 (Hz) is the start frequency at time 0 (sec), and f_1 (Hz) is the end frequency at final time t_1(sec). A_{chirp} represents the magnitude of the chirp signal, which should not excite the system close to the saturation level of the servodrive (±10V). In a linear chirp signal, the instantaneous frequency $f_0 + \frac{f_1 - f_0}{t_1}t$ varies linearly with time and is accompanied by harmonic frequencies as a result of frequency modulation. chirp excitation has the advantages of wide and flat amplitude spectrum with independent scalability in time and frequency domain. (Nahvi & Hoyle, 2009). In addition, since usually system parameters change with frequency, single frequency measurement is not enough to fully identify system under test. Therefore sweeping over a wide range of frequencies is needed. Excitation under chirp is short enough to avoid significant changes during the analysis and long enough for amplifying the excitation energy and improving signal to noise ratio (Annus et al., 2012). The chirp signal gives a good control over the excited frequency band and avoids aliasing noise in measurements (Bondarev, 1988). Using the chirp signal, characteristics of a system can be obtained in a wide frequency range during a very short measurement cycle. The sweep frequency of the chirp signal is determined to cover a range from low frequencies to beyond the natural frequency of the system; f_0=0.016 Hz to f_1 =25 Hz. According to the selected frequencies, the system should be excited for at least 1/ f_0 = 62.5 sec. The frequency responses of the system were obtained for different load masses (12.3, 13.4, and 14.56 kg) and different environment stiffnesses (82 and 125 kN/m). Figure 6.1 shows a typical chirp input voltage to the servodrive, u_m, and the corresponding output pressure, P_L, of the electro-hydrostatic actuator. Corresponding to each pair of input-output, a frequency response is obtained, consisting of magnitude and phase for the range of frequencies between f_0 and f_1.

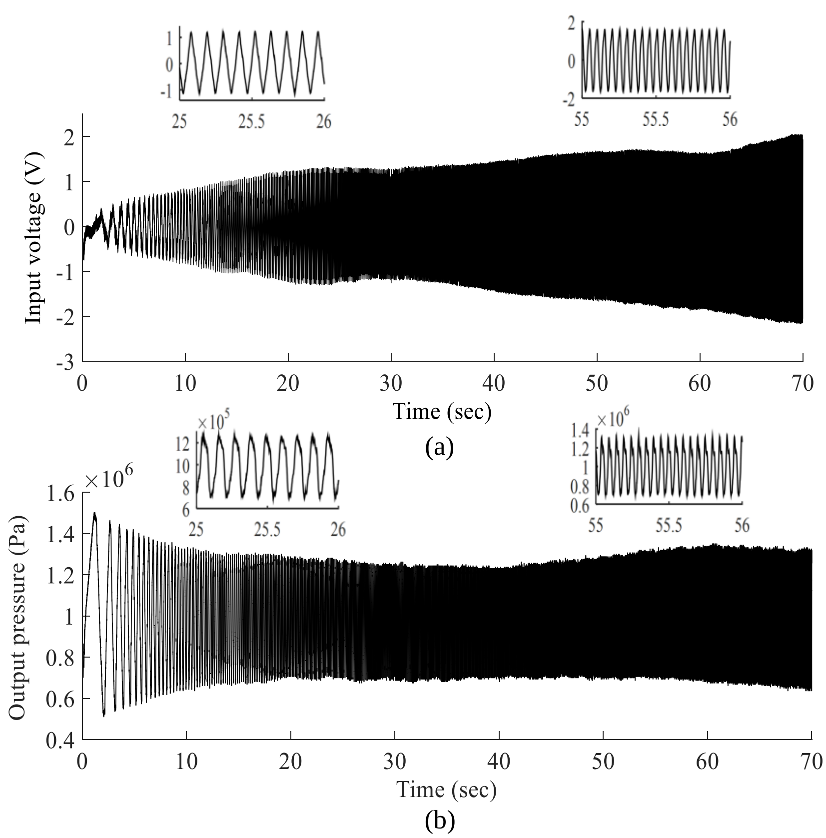

Figure 6.1. (a) Typical linear swept-frequency input signal, u_m; (b) corresponding output pressure, P_L. Hydraulic actuator is operating against a spring having stiffness of 82 kN/m, and carrying a 12.3 kg mass.

For each calculated frequency response, CIFER provided the degree of validation by a coherence coefficient for each of the frequencies between f_0 and f_1. A frequency response is valid if the coherence coefficient is close to one and there are no rapid changes in the frequency response (Rupnik, 2005). The family of frequency responses derived by CIFER for all excitation tests is calculated in this research, shown in Figure 6.2.

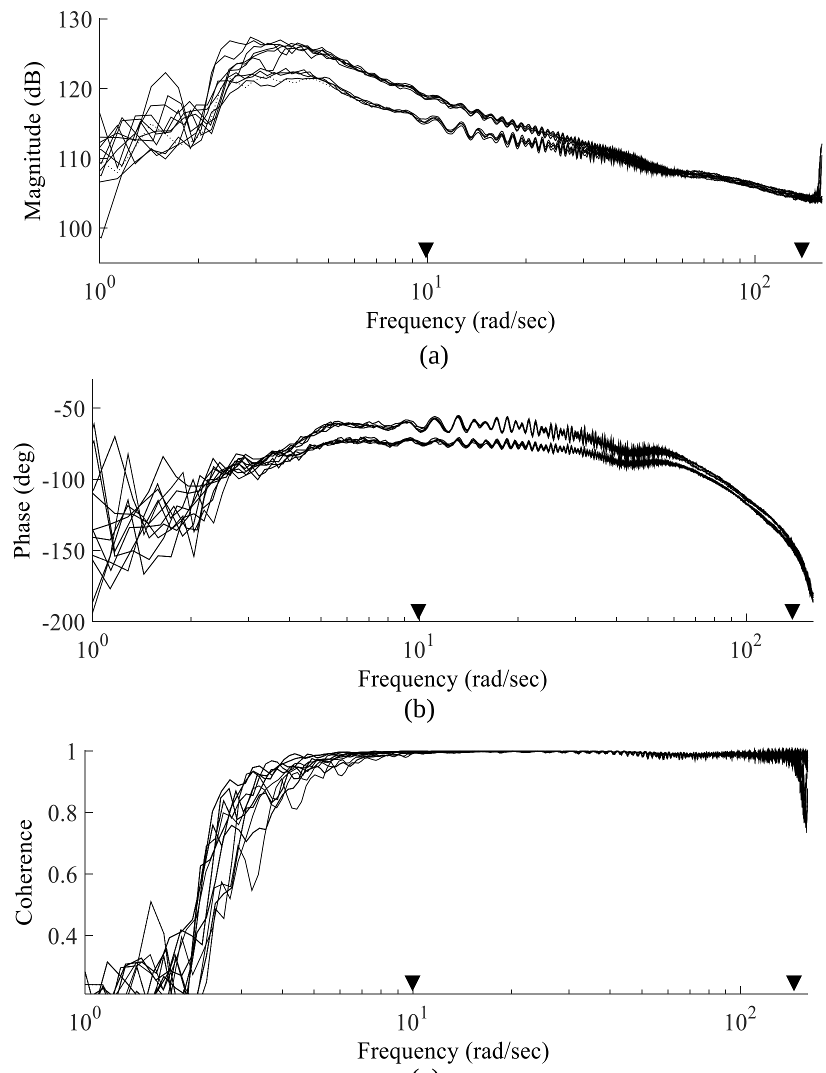

Figure 6.2. Family of frequency responses of experimental electro-hydrostatic actuator with output pressure, P_L, and input voltage, u_m, for different masses (12.3, 13.4, and 14.56 kg) and different spring stiffnesses (82 and 125 kN/m): (a) Magnitude (dB); (b) phase (deg); (c) coherence coefficient. Acceptable frequency response range is shown between arrows.

6.2 Controller Design

Figure 6.3 shows a two degree-of-freedom feedback structure (D'Azzo and Houpis, 1988) to control the output pressure P_L. The uncertain plant is shown by $G(s,\alpha)$, where α is an uncertain parameter vector of the system. Disturbance at the plant output, caused by the friction and external force, is shown by D. Using QFT design technique, the controller $C(s)$ and pre-filter $F(s)$ are designed in the frequency domain using Nichols chart and Bode diagram. First the family of frequency responses of nonlinear plant for a set of inputs-outputs and in the presence of parametric uncertainties are obtained and represented in the Nichols chart, known as plant templates. Using the plant templates, performance criteria consisting of stability, desired tracking, and disturbance rejection are graphically represented in the Nichols chart. During the loop-shaping process, the QFT controller is designed such that the nominal loop transmission function satisfies the QFT bounds presented in the Nichols chart. Finally, the pre-filter $F(s)$ is designed in Bode diagram to complete the tracking requirements.

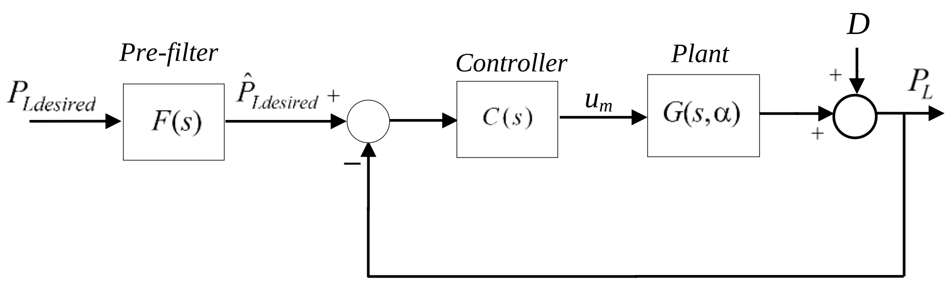

Figure 6.3. QFT control system for output pressure of electro-hydrostatic actuator.

6.2.1 Generating Plant Templates

To generate the plant templates, the identified frequency responses of the electro-hydrostatic actuator, shown in Figure 6.2 are employed. The frequency responses over ω={10,20,30,50,100,150} rad/sec are used since they are confirmed by the coherence coefficient as valid. Therefore, the corresponding magnitude and phase for each frequency in this vector are plotted in the Nichols chart, shown in Figure 6.4. These plant templates graphically represent the parametric uncertainties of the system as captured by the experiments in the frequency domain. From the family of plant templates, one arbitrary plant (actuator carrying the mass of 12.3 kg and interacting with the spring of 125 kN/m) is designated as the nominal plant, i.e., $G_0(j\omega) = G(j\omega, \alpha_0)$. The frequency response of the nominal plant at each design frequency is shown by a circle in Figure 6.4. This plant is used to calculate the QFT bounds in the next section.

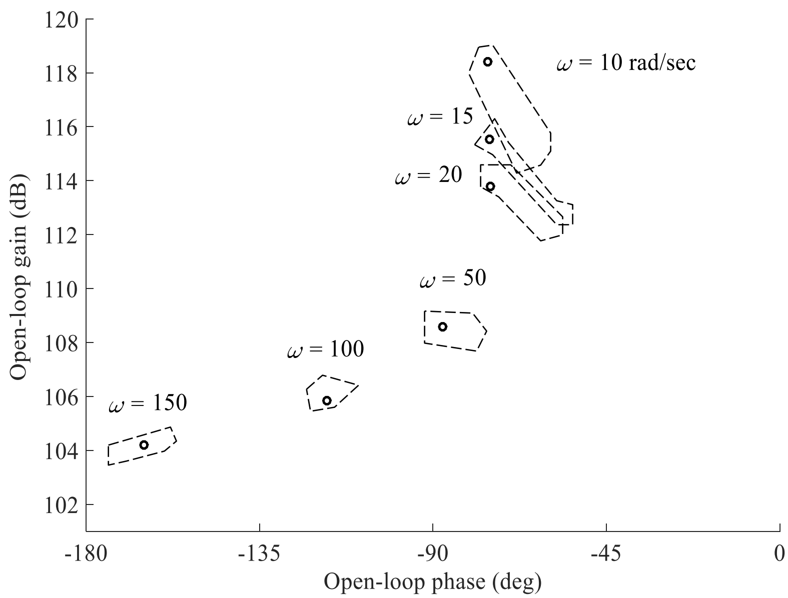

Figure 6.4. Plant templates at design frequencies ω (rad/sec) for electro-hydrostatic actuator. Circles represent frequency response of nominal plant.

6.2.2 QFT Bounds

In this section, a controller and a pre-filter are designed to satisfy the following performance criteria for the closed-loop system of electro-hydrostatic actuator:

i) *Closed-loop robust stability*. The QFT robust stability constraint is given by:

$$\left|\frac{L(j\omega)}{1+L(j\omega)}\right| \le M_t = 1.4 \quad \forall \omega \in [0 \quad \infty) \tag{6.2}$$

where the transfer function, $L(j\omega) = C(j\omega)G(j\omega, \alpha)$, is called loop transmission function, and $G(j\omega, \alpha)$ represents the family of frequency responses of the electro-hydrostatic actuator.

Criterion (6.2) implies the gain margin of 4.68 dB, and the phase margin of 42^{o} for the closed-loop system (Yaniv, 1999).

ii) *Output disturbance rejection*. For disturbance attenuation at the plant output, an upper tolerance is imposed on the disturbance attenuation transfer function as follows:

$$\left|\frac{1}{1+L(j\omega)}\right| \leq 1.65 \quad \forall\omega\in[0\ \infty) \tag{6.3}$$

The output disturbance rejection function also represents the closed-loop sensitivity transfer function.

iii) *Robust reference input tracking*. The controller must satisfy the following inequality for tracking performance requirement:

$$|T_l(j\omega)| \leq \left|F(j\omega)\frac{L(j\omega)}{1+L(j\omega)}\right| \leq |T_u(j\omega)| \quad \forall\omega\in[0 \quad \infty) \tag{6.4}$$

where $T_u(j\omega)$ and $T_l(j\omega)$ are the upper and lower bounds, respectively:

$$T_u(s) = \frac{1.7\times 10^4 (s+2.2)}{(s+2.8)(s+90)(s+150)} \tag{6.5}$$

$$T_l(s) = \frac{42000}{(s+35)^3} \tag{6.6}$$

These bounds are built from specific time and frequency domain figures of merit (D'Azzo and Houpis, 1988). The time responses of the upper and lower bounds are shown in Figure 6.5. Given these tracking bounds, the minimum bandwidth of 3 Hz is expected for the output pressure tracking. Design specifications (*i*)-(*iii*) are combined and plotted as bounds in the Nichols chart and shown in Figure 6.6. These bounds are used in the next section to design a robust QFT controller through a loop-shaping process.

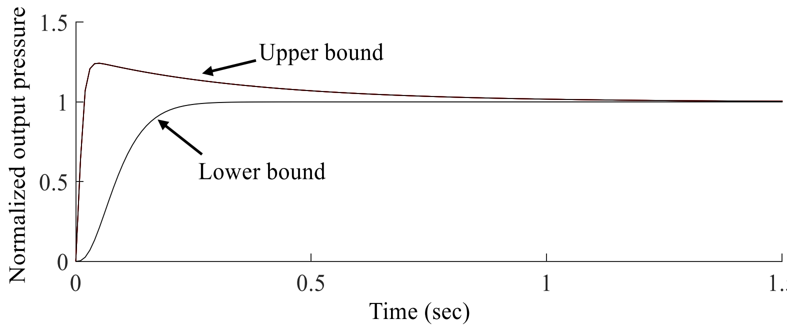

Figure 6.5. Time responses of tracking bounds.

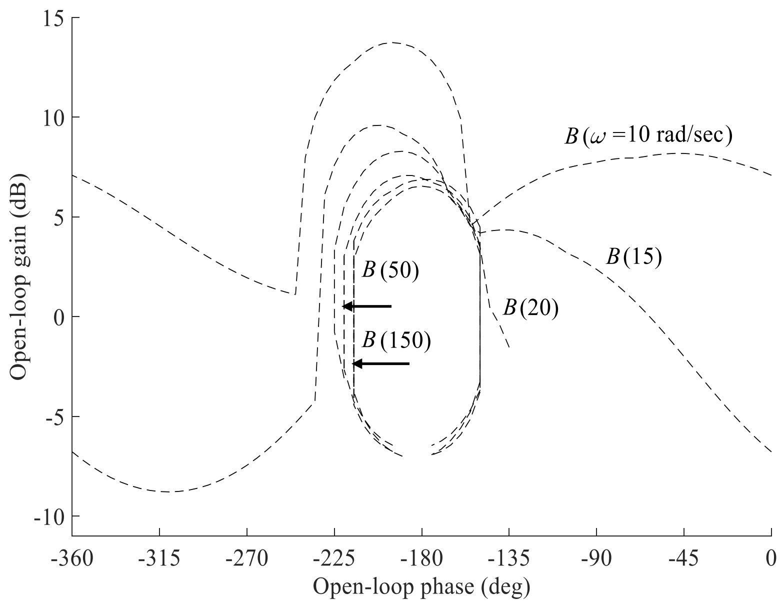

Figure 6.6. QFT bounds in Nichols chart for selected design frequencies, ω (rad/sec).

6.2.3 Loop-Shaping and Pre-filter Design

Once the QFT bounds are constructed, the frequency response of the nominal loop transmission function, $L_0(j\omega) = C(j\omega)G_0(j\omega, \alpha_0)$, is shaped by adding appropriate zeros and poles, and adjusting the controller gain, such that it lies on or above the open bounds and does not enter the closed bounds at each corresponding frequency. The following controller, $C(s)$, satisfies the QFT bounds as shown in Figure 6.7.

$$C(s) = (5\times10^{-7})\frac{(s+1000)}{(s+158)} \text{ (V/Pa)} \tag{6.7}$$

To design the controller (6.7), first the proportional loop gain was adjusted so that the QFT bounds *B*(10)-*B*(100) are satisfied. To satisfy the bound *B*(150), a slight positive phase is required which is obtained by adding a zero at -1000. This zero also contributes to a stronger stability margin and disturbance rejection. To roll off the high-frequency controller gain, a pole at -158 is added to the controller which also filters the noise in the pressure data, measured by the pressure transducers. The last step is to design a pre-filter to locate the frequency responses of the control system within the specified tracking bounds according to inequality (6.4). The following pre-filter satisfies the tracking criterion as shown in Figure 6.8:

$$F(s) = \frac{(5085)(s+8)}{(s+11.3)(s+60)^2} \tag{6.8}$$

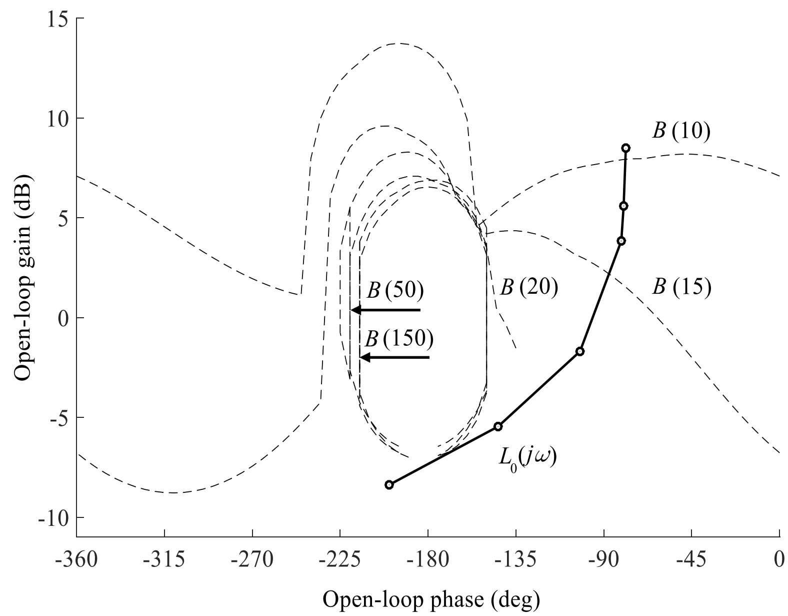

Figure 6.7. QFT bounds (dashed lines) and nominal loop transmission, $L_0(s) = C(s)G_0(s,\alpha_0)$ (solid line) after compensation by controller $C(s)$.

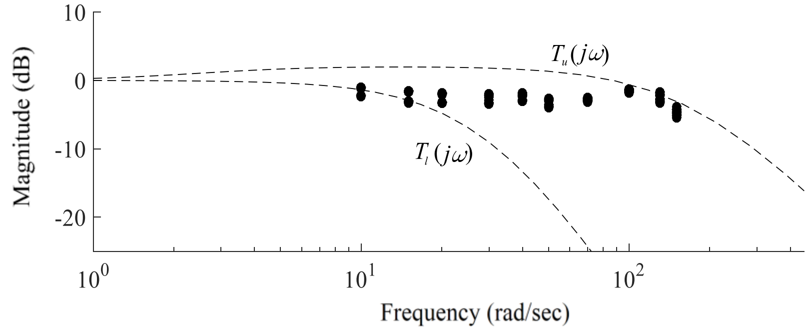

(a)

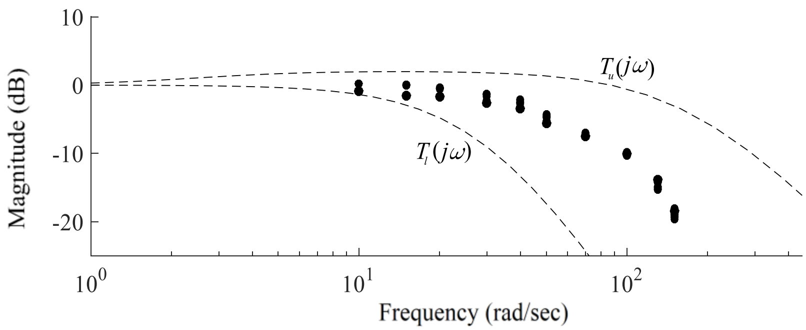

(b)

Figure 6.8. Frequency responses of closed-loop system using controller (6.7): (a) before adding pre-filter; (b) after adding pre-filter.

6.3 Experimental Validation

The designed controller and pre-filter, shown by equations (6.7) and (6.8) are applied to the experimental set-up of electro-hydrostatic actuator, described in Section 2.2.1. Figure 6.9 shows the normalized output pressure responses of the closed-loop system to different desired step inputs having the magnitudes of 1 MPa, 2 MPa, 2.5 MPa, and 3 MPa. In running the above experiments, two springs having stiffnesses of 125 kN/m and 82 kN/m, and two masses of 12.3 kg, 14.56 kg added to the actuator, were used. Figure 6.9 also shows the corresponding control signals as well as the error signals between the desired and actual responses. Using these step responses, features like overshoot and settling time are observed and compared with those specified by the tracking bounds, given by equations (6.5) and (6.6). Results show that despite the variation in the system parameters and operating conditions, the control system successfully tracks the desired step input of different magnitudes within the desired upper and lower bounds. For all responses in Figure 6.9, the settling time is within 0.2 - 0.3 sec and the percentage of overshoot stays below 5, which are in accordance with the tracking bounds. In Figure 6.9, the steady-state errors are less than 0.5% of the desired inputs. A close-up view of a typical normalized step response given the desired input of 2.5 MPa in steady-state is shown in Figure 6.10a. The corresponding control signal is shown in Figure 6.10b. Since the controller (6.7) does not have an integral term, the steady-state error is inevitable. Using the integral term slows down the system response. The steady-state error less than 0.5% is a compromise to keep the system response fast enough to comply with the tracking criterion, given in (6.4)-(6.6).

Figure 6.11 shows the output pressure of the hydraulic actuator and the corresponding control signal, in tracking of the following desired input:

$$P_{Ldesired} = (1 + 0.6\sin(10\pi t))\ \text{MPa} \tag{6.9}$$

For this experiment, the actuator operates against a spring with a stiffness of 125 kN/m, carrying a 12.3 kg load. The result shows that the closed-loop system achieves a bandwidth of 5 Hz when the actuator operates against the 125 kN/m spring. Here, the bandwidth is considered by its common definition as the frequency at which the control system attenuates the magnitude of the desired input by -3dB. The test was repeated with a 14.56 kg load. The controller successfully achieved the same amount of bandwidth. Figure 6.12 shows the simulation response to the input signal in equation (6.9). Figure 6.13 shows the output pressure of the hydraulic actuator and the corresponding control signal in tracking of the following sinusoidal input:

$$P_{Ldesired} = (1 + 0.6\sin(6\pi t))\ \text{MPa} \tag{6.10}$$

For this experiment, the actuator operated against a spring with a stiffness of 82 kN/m, moving a 12.3 kg load. Result shows the success of the control system in achieving a bandwidth of 3 Hz for this amount of stiffness. Similar result was achieved for the actuator carrying a 14.56 kg load. Figure 6.14 shows the simulation response to the input signal in equation (6.10).

One worth mentioning observation from the above experimental results is that the achieved bandwidth of the closed-loop system reduced by decreasing the stiffness of the spring. The effect of the spring stiffness on the achievable tracking bandwidth was also documented by Robinson (2000). Both achieved bandwidths of 5 Hz and 3 Hz are located within allowable tracking bandwidth according to equations (6.5) and (6.6).

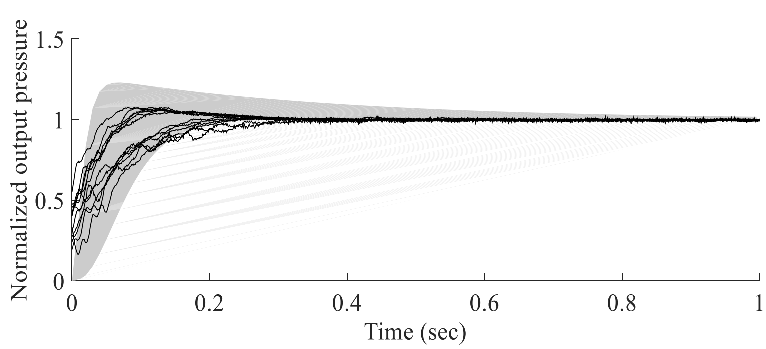

(a)

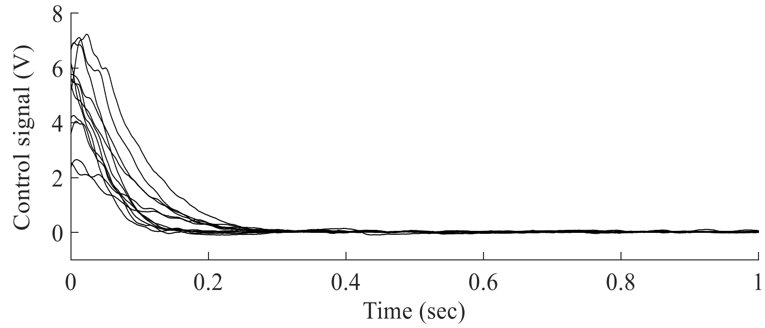

(b)

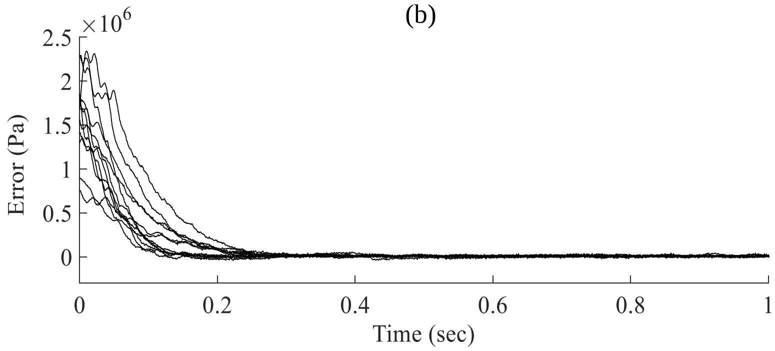

(c)

Figure 6.9. (a) Normalized output pressure responses using springs with 82 and 125 kN/m stiffnesses, and carrying 12.3 and 14.56 kg loads- the desired inputs are within 1-3 MPa; (b) corresponding control signals; (c) corresponding error signals between desired and actual output pressures.

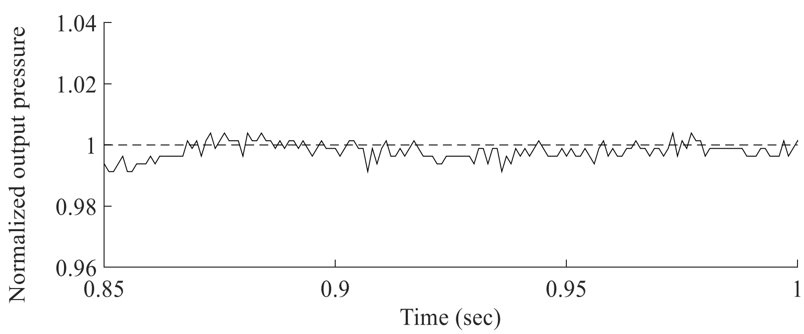

(a)

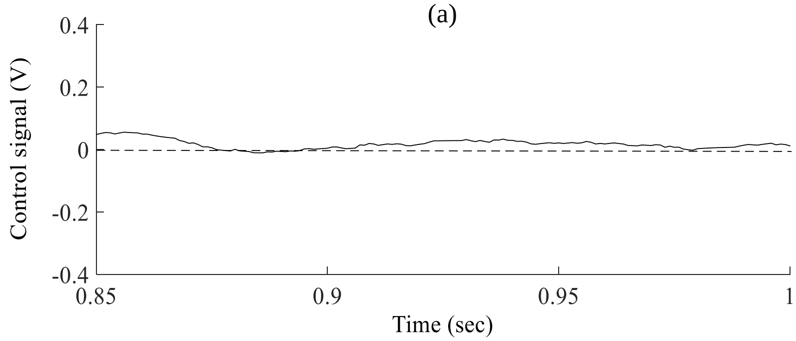

(b)

Figure 6.10. (a) Close-up view of output pressure response around steady-state using a 82 kN/m stiffness spring and carrying 12.3 kg load; (b) corresponding control signal.

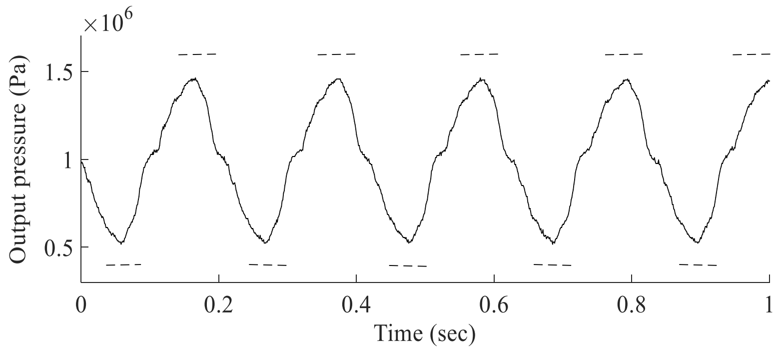

(a)

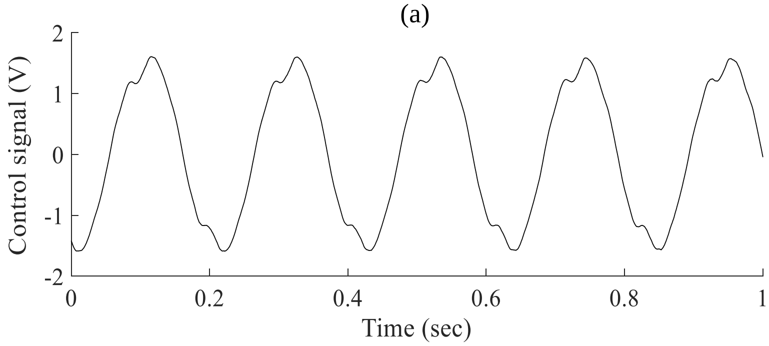

(b)

Figure 6.11. (a) 5 Hz sinusoidal output pressure tracking using 125 kN/m spring - the desired peak values are shown by dashed lines; (b) corresponding control signal.

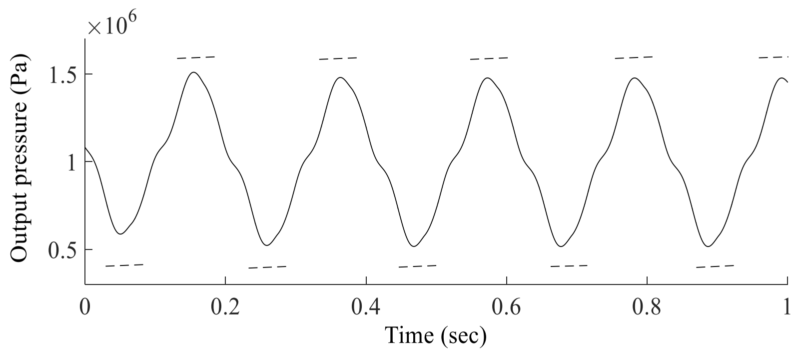

(a)

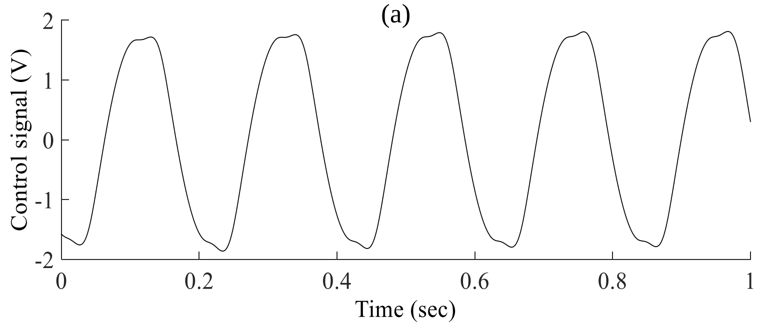

(b)

Figure 6.12. Simulation results: (a) 5 Hz sinusoidal output pressure tracking using 125 kN/m spring - the desired peak values are shown by dashed lines; (b) corresponding control signal.

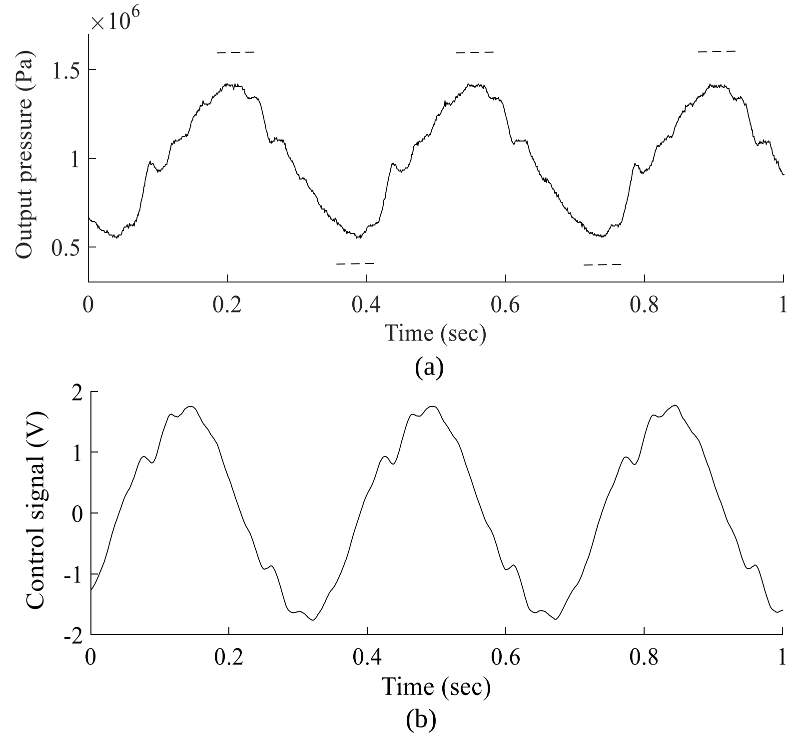

Figure 6.13. (a) 3 Hz sinusoidal output pressure tracking using 82 kN/m spring - the desired peak values are shown by dashed lines; (b) corresponding control signal.

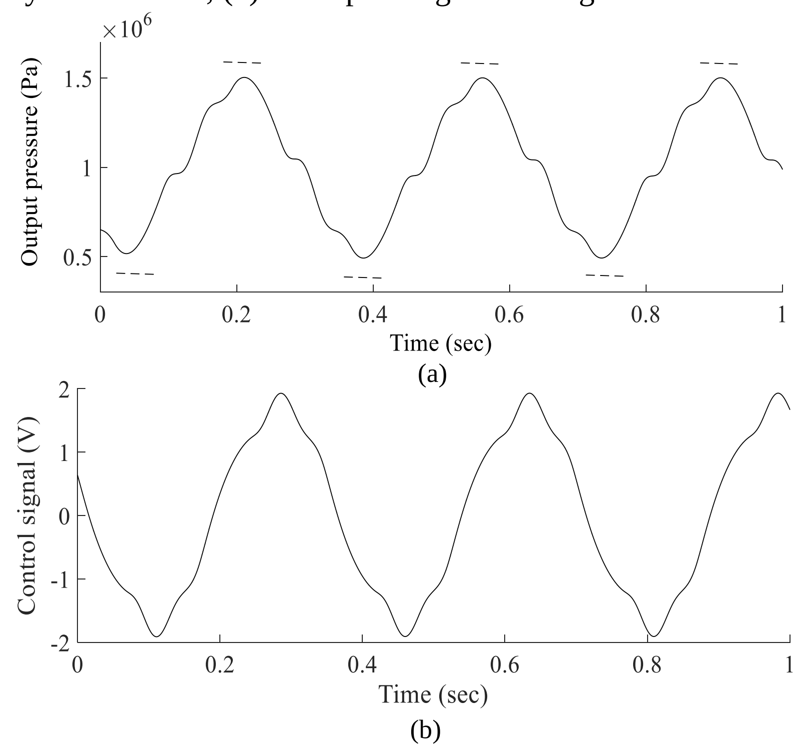

Figure 6.14. Simulation results: (a) 3 Hz sinusoidal output pressure tracking using 82 kN/m spring - the desired peak values are shown by dashed lines; (b) corresponding control signal.

6.4 Stability Analysis

The QFT controller was designed for the identified family of frequency responses of the system, in Section 6.1. These frequency responses were obtained for the particular values of system parameters and operating conditions. As a result, the designed QFT controller guarantees the closed-loop stability condition in (6.2) only for the identified set of frequency responses, and for particular values of system parameters, used in the experiments. To investigate the stability of the designed QFT controller, in the presence of a continuous range of parametric uncertainties, T-S fuzzy modeling and the corresponding stability theory (Tanaka and Wang, 2001) are employed in this section. Here, T-S fuzzy model of the electro-hydrostatic actuator is blended with the designed QFT controller to investigate the nonlinear stability of the closed-loop system. To derive the T-S fuzzy model, sector nonlinearity approach (Tanaka and Wang, 2001) is employed. Stability conditions of T-S fuzzy models are then derived.

6.4.1 T-S Fuzzy Model of Electro-Hydrostatic Actuator

The equations representing the model of electro-hydrostatic actuator were given in Section 2.2.2. Since the control variable is the output pressure P_L, first a differential equation for P_L is obtained using equations presented in Section 2.2.2. Assuming small piston displacement, the volume of the hydraulic oil in each side of the piston is approximated as $V_1 \approx V_2 \approx V_t / 2$, where V_t is the total volume of the cylinder. Furthermore, V_U and V_D are very small quantities as compared to V_1 and V_2, and having β as a large quantity, then, V_U / β and V_D / β are considered negligible. By substituting equations (2.12) into (2.14), and applying the above assumptions, the differential equation describing P_L is obtained as follows:

$$\dot{P}_L = \frac{4\beta}{V_t}(D_p \omega_m - c_T P_L - A v_p) \tag{6.11}$$

In (6.11), $c_T = C_{ip} + \dfrac{C_{ep}}{2} + \dfrac{k_e}{2} + k_i$, and is called total leakage coefficient of electro-hydrostatic actuator. By substituting friction in equation (2.10) into equation (2.16), and assuming f_l=0, the equations describing the nonlinear dynamics of the electro-hydrostatic actuator are given as follows:

$$\dot{x}_p = v_p \tag{6.12a}$$

$$\dot{v}_p = \frac{1}{m}(AP_L - kx_p - (d+\sigma_1)v_p - (\sigma_0 - \sigma_1\sigma_0\psi(v_p))\eta) \tag{6.12b}$$

$$\dot{P}_L = \frac{4\beta}{V_t}(D_p\omega_m - c_T P_L - Av_p) \tag{6.12c}$$

$$\dot{\omega}_m = \frac{-1}{\tau_m}\omega_m + \frac{k_m}{\tau_m}u_m \tag{6.12d}$$

$$\dot{\eta} = v_p - \sigma_0\psi(v_p)\eta \tag{6.12e}$$

where $\psi(v_p)$ is as follows:

$$\psi(v_p) = \frac{|v_p|}{F_c + (F_s - F_c)e^{-|v_p/v_s|^{\alpha_f}}} \tag{6.13}$$

To establish a T-S fuzzy model for the electro-hydrostatic actuator described by equations (6.12), the nonlinear terms must be represented in a sector. The only nonlinear term in equations (6.12) is $\psi(v_p)$. Therefore, a sector $[\delta_2 \quad \delta_1]$ is defined such that $\psi(v_p)\eta \in [\delta_2 \quad \delta_1]\eta$ .Then nonlinear term $\psi(v_p)$ is represented as follows:

$$\psi(v_p) = \Gamma_1(\psi(v_p))\delta_1 + \Gamma_2(\psi(v_p))\delta_2 \tag{6.14}$$

In equation (6.14), $\Gamma_{i(i=1,2)}$ are positive nonlinear membership functions, defined as follows:

$$\Gamma_1(\psi(v_p)) = \frac{\psi(v_p) - \delta_2}{\delta_1 - \delta_2} \tag{6.15a}$$

$$\Gamma_2(\psi(v_p)) = \frac{\delta_1 - \psi(v_p)}{\delta_1 - \delta_2} \tag{6.15b}$$

where $\sum_{i=1}^{2}\Gamma_i(\psi(v_p)) = 1$, and $\delta_{i(i=1,2)}$ are the extremums of $\psi(v_p)$. Given $F_c \in [70 \quad 280]$ N, $F_s \in [200 \quad 500]$ N, $v_s \in [0.007 \quad 0.015]\left(\frac{\mathrm{m}}{\mathrm{sec}}\right)$, $\alpha_f \in [0.5 \quad 2]$, and $v_p \in [-0.4 \quad 0.4]\left(\frac{\mathrm{m}}{\mathrm{sec}}\right)$, $\delta_{i(i=1,2)}$ are as follows:

$$\delta_1 = \max(\psi(v_p)) = \left.\frac{|v_p|}{F_c + (F_s - F_c)e^{-|v_p/v_s|^{\alpha_f}}}\right| = 0.0016 \tag{6.16a}$$

$$\delta_2 = \min(\psi(v_p)) = \left. \frac{|v_p|}{F_c + (F_s - F_c)e^{-|v_p / v_s|^{\alpha_f}}} \right| = 0 \tag{6.16b}$$

In addition to the nonlinear term $\psi(v_p)$, the T-S fuzzy model must also include the effect of uncertain parameters. In this research, uncertainty is considered in the environmental stiffness k, hydraulic fluid bulk modulus β, total damping d, total mass m, servomotor gain k_m, and servomotor time constant τ_m, micro damping coefficient σ_1, bristle stiffness σ_0, and total leakage coefficient c_T. The procedure of incorporating the parametric uncertainties in the T-S fuzzy model of the electro-hydrostatic actuator is similar to the procedure explained in Section 4.3.2. Here, this approach is exemplified using the environmental stiffness k. The same procedure is used for other uncertain parameters. Using the sector nonlinearity approach, the stiffness value, k, can be represented by the following formula:

$$k = S_1(k)k_1 + S_2(k)k_2 \tag{6.17}$$

where $S_1(k)$ and $S_2(k)$, ($\sum_{j=1}^{2} S_j(k) = 1$) are the membership functions, defined as:

$$S_1(k) = \frac{k - k_2}{k_1 - k_2} \tag{6.18a}$$

$$S_2(k) = \frac{k_1 - k}{k_1 - k_2} \tag{6.18b}$$

and k_1 and k_2 are the extremum values of the environmental stiffness k. Now formulations (6.14) and (6.17), replace nonlinear term $\psi(v_p)$ and uncertain parameter k, in equation (6.12):

$$\dot{x}_p = v_p \tag{6.19a}$$

$$\dot{v}_p = \frac{1}{m}\left(AP_L - \sum_{j=1}^{2} S_j(k)k_j x_p - (d + \sigma_1)v_p - \left(\sigma_0 - \sigma_1\sigma_0 \sum_{i=1}^{2} \Gamma_i(\psi(v_p))\delta_i\right)\eta\right) \tag{6.19b}$$

$$\dot{P}_L = \frac{4\beta}{V_t}(D_p\omega_m - c_T P_L - Av_p) \tag{6.19c}$$

$$\dot{\omega}_m = \frac{-1}{\tau_m}\omega_m + \frac{k_m}{\tau_m}u_m \tag{6.19d}$$

$$\dot{\eta} = v_p - \sigma_0\eta \sum_{i=1}^{2} \Gamma_i(\psi(v_p))\delta_i \tag{6.19e}$$

Since $\sum_{i=1}^{2}\Gamma_i(\psi(v_p))=1$ and $\sum_{j=1}^{2}S_j(k)=1$, therefore, $\sum_{i=1}^{2}\sum_{j=1}^{2}\Gamma_i(\psi(v_p))S_j(k)=1$. As a result, these membership functions can be factored to represent equations (6.19) in the following form:

$$\dot{\vec{\boldsymbol{x}}}(t)=\sum_{i=1}^{2}\sum_{j=1}^{2}\Gamma_i(\psi(v_p))S_j(k)\left(\boldsymbol{A}_{ij}\vec{\boldsymbol{x}}(t)+\boldsymbol{B}u_m\right) \tag{6.20}$$

where $\vec{\boldsymbol{x}}=\begin{bmatrix}x_p & v_p & P_L & \omega_m & \eta\end{bmatrix}^{\mathrm{T}}$ is the vector of the system states; $\boldsymbol{A}_{ij}$ and $\boldsymbol{B}$ are given as follows:

$$\boldsymbol{A}_{ij}=\begin{bmatrix} 0 & 1 & 0 & 0 & 0 \\ \frac{-k_j}{m} & \frac{-(\sigma_1+d)}{m} & \frac{A}{m} & 0 & \frac{-(\sigma_0-\sigma_0\sigma_1\delta_i)}{m} \\ 0 & -\frac{4\beta A}{V_t} & -\frac{4\beta c_T}{V_t} & \frac{4\beta D_p}{V_t} & 0 \\ 0 & 0 & 0 & \frac{-1}{\tau_m} & 0 \\ 0 & 1 & 0 & 0 & -\sigma_0\delta_i \end{bmatrix} \tag{6.21a}$$

$$\boldsymbol{B}=\begin{bmatrix}0 & 0 & 0 & \frac{k_m}{\tau_m} & 0\end{bmatrix}^{\mathrm{T}} \tag{6.21b}$$

Equation (6.20) represents the nonlinear model (6.12) as weighted sum ($\sum_{i=1}^{2}\sum_{j=1}^{2}\Gamma_i(\psi(v_p))S_j(k)$) of local linear models $\boldsymbol{A}_{ij}\vec{\boldsymbol{x}}(t)+\boldsymbol{B}u_m$.

Using the same procedure, the uncertainties of the remaining parameters (β, d, m, k_m, τ_m, σ_1, σ_0, c_T) are incorporated in the T-S fuzzy model. The uncertainty ranges of these parameters are considered as follows, bulk modulus ($\beta\in[\beta_2 \quad \beta_1]$), total damping ($d\in[d_2 \quad d_1]$), total mass ($m\in[m_2 \quad m_1]$), servomotor gain ($k_m\in[k_{m2} \quad k_{m1}]$), servomotor time constant ($\tau_m\in[\tau_{m2} \quad \tau_{m1}]$), micro damping coefficient $\sigma_1\in[\sigma_{12} \quad \sigma_{11}]$, bristle stiffness $\sigma_0\in[\sigma_{02} \quad \sigma_{01}]$, and total leakage coefficient $c_T\in[c_{T2} \quad c_{T1}]$. Consequently, the T-S fuzzy model of the electro-hydrostatic actuator in the presence of the above parametric uncertainties is as follows:

$$\begin{aligned}\dot{\vec{\boldsymbol{x}}}(t)=\sum_{i=1}^{2}\sum_{j=1}^{2}\sum_{l=1}^{2}\sum_{n=1}^{2}\sum_{r=1}^{2}\sum_{w=1}^{2}\sum_{y=1}^{2}\sum_{\gamma=1}^{2}\sum_{\lambda=1}^{2}\sum_{\zeta=1}^{2}&\Gamma_i(\psi(v_p))S_j(k)H_l(\beta)N_n(d)M_r(m)W_w(k_m)\\ &\times Y_y(\tau_m)X_\gamma(\sigma_1)Z_\lambda(\sigma_0)G_\zeta(c_T)\left(\boldsymbol{A}_{ijlnrwy\gamma\lambda\zeta}\vec{\boldsymbol{x}}(t)+\boldsymbol{B}_{ijlnrwy\gamma\lambda\zeta}u_m\right)\end{aligned} \tag{6.22}$$

The summations in (6.22) can be aggregated as follows:

$$\dot{\vec{x}}(t) = \sum_{\rho=1}^{1024} \big(q_\rho(z(t))\big)\big(\boldsymbol{A}_\rho^* \vec{x}(t) + \boldsymbol{B}_\rho^* u_m\big) \tag{6.23}$$

where $\boldsymbol{A}_\rho^*$, $\boldsymbol{B}_\rho^*$, $q_\rho(z(t))$, and ρ are given as follows:

$$\boldsymbol{A}_\rho^* = \boldsymbol{A}_{ijlnrwy\gamma\lambda\zeta} = \begin{bmatrix} 0 & 1 & 0 & 0 & 0 \\ \dfrac{-k_j}{m_r} & \dfrac{-(\sigma_{1\gamma} + d_n)}{m_r} & \dfrac{A}{m_r} & 0 & \dfrac{-(\sigma_{0\lambda} - \sigma_{0\lambda}\sigma_{1\gamma}\delta_i)}{m_r} \\ 0 & -\dfrac{4\beta_l A}{V_t} & -\dfrac{4\beta_l c_{T_\zeta}}{V_t} & \dfrac{4\beta_l D_p}{V_t} & 0 \\ 0 & 0 & 0 & \dfrac{-1}{\tau_{m_y}} & 0 \\ 0 & 1 & 0 & 0 & -\sigma_{0\lambda}\delta_i \end{bmatrix} \tag{6.24a}$$

$$\boldsymbol{B}_\rho^* = \boldsymbol{B}_{ijlnrwy\gamma\lambda\zeta} = \begin{bmatrix} 0 & 0 & 0 & \dfrac{k_{m_w}}{\tau_{m_y}} & 0 \end{bmatrix}^{\mathrm{T}} \tag{6.24b}$$

$$q_\rho\big(z(t)\big) = \Gamma_i(\psi(v_p)) S_j(k) H_l(\beta) N_n(d) M_r(m) W_w(k_m) Y_y(\tau_m) X_\gamma(\sigma_1) Z_\lambda(\sigma_0) G_\zeta(c_T) \tag{6.24c}$$

$$\rho = \zeta + 2(\lambda-1) + 4(\gamma-1) + 8(y-1) + 16(w-1) + 32(r-1) + 64(n-1) + 128(l-1) + 256(j-1) + 512(i-1) \tag{6.24d}$$

In equation (6.23), the total number of local linear models is 1024, which is obtained using the formulation of ρ in (6.24d). Note that $S_j(k)$, $H_l(\beta)$, $N_n(d)$, $M_r(m)$, $W_w(k_m)$, $Y_y(\tau_m)$, $X_\gamma(\sigma_1)$, $Z_\lambda(\sigma_0)$, and $G_\zeta(c_T)$ are the membership functions related to the environment stiffness k, effective bulk modulus β, total damping d, total mass of the moving actuator m, servomotor gain k_m, servomotor time constant τ_m, micro damping coefficient σ_1, bristle stiffness σ_0, and leakage coefficient c_T.

6.4.2 Stability Verification

The QFT controller in (6.7) are added to the T-S fuzzy model of the electro-hydrostatic actuator, described by equation (6.23), to represent the closed-loop system as a single T-S fuzzy model. For this purpose, the transfer function of the QFT controller must be represented in time domain. The transfer function of the controller represents the relationship between error and the input voltage to the servodrive in Laplace domain. First a dummy variable $X_c(s)$ are multiplied in the numerator and denominator of the controller transfer function as follows (Rowell, 2002):

$$\frac{U_m(s)}{E_{P_L}(s)} = (5\times10^{-7})\frac{(s+1000)}{(s+158)}\frac{X_c(s)}{X_c(s)} \tag{6.25}$$

Thus:

$$U_m(s) = \left(5\times10^{-7}\right)sX_c(s) + \left(5\times10^{-4}\right)X_c(s) \tag{6.26a}$$

$$E_{P_L}(s) = sX_c(s) + 158X_c(s) \tag{6.26b}$$

Applying inverse Laplace transformation on (6.26), the following equations in time-domain are derived:

$$u_m(t) = \left(5\times10^{-7}\right)\dot{x}_c(t) + \left(5\times10^{-4}\right)x_c(t) \tag{6.27a}$$

$$e_{P_L}(t) = \dot{x}_c(t) + 158x_c(t) \tag{6.27b}$$

From the above equations, the state-space formulation for the QFT controller is constructed:

$$\dot{x}_c(t) = -158x_c(t) + e_{P_L}(t) = a_c x_c(t) + b_c e_{P_L}(t) \tag{6.28a}$$

$$u_m(t) = \left(4.21\times10^{-4}\right)x_c(t) + \left(5\times10^{-7}\right)e_{P_L}(t) = c_c x_c(t) + d_c e_{P_L}(t) \tag{6.28b}$$

Figure 6.15 shows the state-space model of the QFT controller and the T-S fuzzy model, describing the electro-hydrostatic actuator. Note that for the stability analysis, the pre-filter $F(s)$ (see Figure 6.3) is not required to be considered. Referring to Figure 6.15, the T-S fuzzy model of the electro-hydrostatic actuator combined with the controller state-space equations, in the closed-loop format are shown in below:

$$\begin{cases} \dot{\vec{\boldsymbol{x}}}(t) = \sum\limits_{\rho=1}^{1024} q_\rho(z(t))\left(\boldsymbol{A}_\rho^*\vec{\boldsymbol{x}}(t) + \boldsymbol{B}_\rho^*\left(c_c x_c + d_c(\hat{P}_{Ldesired} - P_L)\right)\right) & (6.29a) \\ \dot{x}_c(t) = a_c x_c + b_c(\hat{P}_{Ldesired} - P_L) & (6.29b) \end{cases}$$

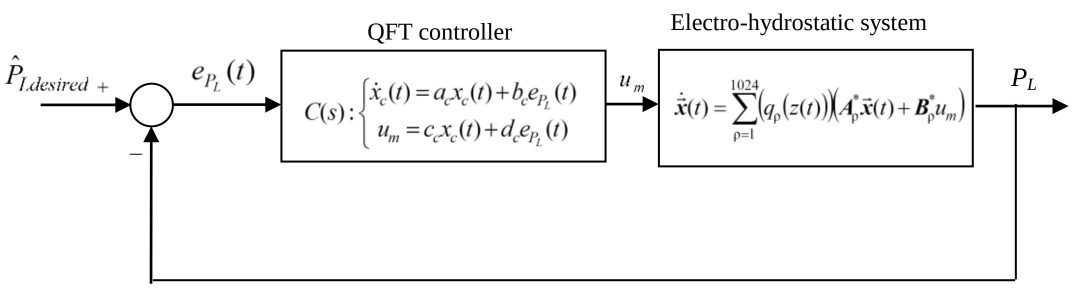

Figure 6.15. Control loop of output pressure of electro-hydrostatic actuator for stability analysis.

In the above equations, $e_{P_L}(t)$ was substituted as $\hat{P}_{Ldesired} - P_L$. Since $\sum_{\rho=1}^{1024}\left(q_\rho\left(z(t)\right)\right)=1$, equations (6.29) can be combined as follows:

$$\begin{bmatrix} \dot{\vec{x}} \\ x_c \end{bmatrix} = \sum_{\rho=1}^{1024} q_\rho(z(t)) \left(\begin{pmatrix} \boldsymbol{A}_\rho^* - \boldsymbol{B}_\rho^* d_c [0 \quad 0 \quad 1 \quad 0 \quad 0] & \boldsymbol{B}_\rho^* c_c \\ -b_c [0 \quad 0 \quad 1 \quad 0 \quad 0] & a_c \end{pmatrix} \begin{bmatrix} \vec{x} \\ x_c \end{bmatrix} + \begin{bmatrix} \boldsymbol{B}_\rho^* d_c \\ b_c \end{bmatrix} \hat{P}_{Ldesired} \right) \tag{6.30}$$

Equation (6.30) represents the closed-loop control system in the presence of parametric uncertainties, uncertain nonlinear friction, and leakages. To investigate the nonlinear stability of this system, first the equilibrium point, i.e., $\begin{bmatrix}\vec{x}_{eq}^{\mathrm{T}} & x_{ceq}\end{bmatrix}^{\mathrm{T}} = \begin{bmatrix}x_{peq} & v_{peq} & P_{Leq} & \omega_{meq} & \eta_{eq} & x_{ceq}\end{bmatrix}^{\mathrm{T}}$ is obtained by solving the equations of the closed-loop system in steady-state, i.e. $\begin{bmatrix}\dot{\vec{x}}^{\mathrm{T}} & \dot{x}_c\end{bmatrix}^{\mathrm{T}} = \begin{bmatrix}\dot{x}_p & \dot{v}_p & \dot{P}_L & \dot{\omega}_m & \dot{\eta} & \dot{x}_c\end{bmatrix}^{\mathrm{T}} = 0$. As a result, the equilibrium point is obtained with respect to $\hat{P}_{Ldesired}$ as follows:

$$x_{peq} = \frac{AD_p(-k_m d_c a_c + k_m c_c b_c)\hat{P}_{Ldesired}}{k(-c_T a_c + k_m D_p c_c b_c - d_c k_m a_c D_p)} \tag{6.31a}$$

$$v_{peq} = 0 \tag{6.31b}$$

$$P_{Leq} = \frac{D_p(-k_m d_c a_c + k_m c_c b_c)\hat{P}_{Ldesired}}{(-c_T a_c + k_m D_p c_c b_c - d_c k_m a_c D_p)} \tag{6.31c}$$

$$\omega_{meq} = \frac{c_T(-k_m d_c a_c + k_m c_c b_c)\hat{P}_{Ldesired}}{(-c_T a_c + k_m D_p c_c b_c - d_c k_m a_c D_p)} \tag{6.31d}$$

$$\eta_{eq} = 0 \tag{6.31e}$$

$$x_{ceq} = \frac{b_c c_T \hat{P}_{Ldesired}}{-c_T a_c + k_m D_p c_c b_c - d_c k_m a_c D_p} \tag{6.31f}$$

The above equilibrium point is not at the origin; therefore by defining $\vec{e} = \vec{x} - \vec{x}_{eq}$ and $e_c = x_c - x_{ceq}$, the following error dynamic equation is derived:

$$\begin{bmatrix} \dot{\vec{e}} \\ \dot{e}_c \end{bmatrix} = \sum_{\rho=1}^{1024} q_\rho(z(t)) \underbrace{\begin{pmatrix} \boldsymbol{A}_\rho^* - \boldsymbol{B}_\rho^* d_c [0 \quad 0 \quad 1 \quad 0 \quad 0] & \boldsymbol{B}_\rho^* c_c \\ -b_c [0 \quad 0 \quad 1 \quad 0 \quad 0] & a_c \end{pmatrix}}_{\boldsymbol{A}_{closed-loop}} \begin{bmatrix} \vec{e} \\ e_c \end{bmatrix} \tag{6.32}$$

where $\boldsymbol{A}_{closed-loop}$ is:

$$
\boldsymbol{A}_{closed-loop} = \begin{bmatrix} 0 & 1 & 0 & 0 & 0 & 0 \\ \dfrac{-k_j}{m_r} & \dfrac{-(\sigma_{1\gamma}+d_n)}{m_r} & \dfrac{A}{m_r} & 0 & \dfrac{-(\sigma_{0\lambda}-\sigma_{0\lambda}\sigma_{1\gamma}\delta_i)}{m_r} & 0 \\ 0 & -\dfrac{4\beta_l A}{V_t} & -\dfrac{4\beta_l c_{T_\zeta}}{V_t} & \dfrac{4\beta_l D_p}{V_t} & 0 & 0 \\ 0 & 0 & \dfrac{-k_{mw} d_c}{\tau_{my}} & \dfrac{-1}{\tau_{my}} & 0 & \dfrac{k_{mw}}{\tau_{my}} c_c \\ 0 & 1 & 0 & 0 & -\sigma_{0\lambda}\delta_i & 0 \\ 0 & 0 & -b_c & 0 & 0 & a_c \end{bmatrix} \tag{6.33}
$$

The stability LMIs for T-S fuzzy model of the closed-loop system described by equations (6.32)-(6.33) are constructed based on conditions (4.6) and (4.7). As a result these LMIs become feasible for the uncertainty ranges of parameters given in Table 6.1, with the following positive definite matrix $\boldsymbol{P}$:

$$
\boldsymbol{P} = \begin{bmatrix} 1.71\times10^6 & 300 & 2.6\times10^5 & -9200 & 200 & 1.768 \\ 300 & 65.41 & -21.68 & -3.64 & -0.019 & 0.0001 \\ 0.26\times10^6 & -21.68 & 1.8\times10^5 & 880 & 162.81 & 0.7271 \\ -9200 & -3.64 & 880 & 186.9 & 0.771 & -0.0014 \\ 200 & -0.019 & 162.81 & 0.771 & 13.482 & 0.0151 \\ 1.768 & 0.0001 & 0.7271 & -0.0014 & 0.0151 & 75.956 \end{bmatrix} \tag{6.34}
$$

Table 6.1. Range of parametric uncertainties with feasible LMIs for electro-hydrostatic pressure control system.

Parameter	Range for feasible LMIs
Environment stiffness, k (kN/m)	80-125
Total mass, m (kg)	11-16
Total damping coefficient, d (N.sec/m)	200-300
Effective bulk modulus, β (MPa)	20-900
Servomotor time constant, τ_m (sec)	9×10^{-4}-1×10^{-3}
Servomotor gain, k_m (rad/V.sec)	24-26
Leakage coefficient, c_T (m^3/sec/$Pa^{1/2}$)	5×10^{-12}-5×10^{-13}
Stribeck velocity, v_s (m/sec)	0.007-0.015
Friction geometry parameter α_f	0.5-2
Coulomb friction, F_c (N)	70-280
Stiction friction, F_s (N)	200-500
Average stiffness of bristles, σ_0 (N/m)	1.03×10^9-1.07×10^9
Micro damping coefficient, σ_1 (N.sec/m)	90-110

6.5 Summary

Quantitative feedback theory (QFT) was employed to design a robust, linear, and fixed-gain controller for the output pressure of a double-rod electro-hydrostatic actuator. The family of frequency responses of the actuation was derived experimentally using an advanced form of fast Fourier transform on the measured input-output data. This approach avoided creation of unnecessary large templates and resulted in the design of a low-order controller. The designed QFT controller satisfied robust stability, disturbance rejection, desired tracking bandwidth and desired transient response performance criteria. Experimental results showed settling-times below 0.3 sec, overshoots below 5% and, steady-state errors less than 0.5% of the desired output pressure step inputs of different magnitudes. The experiments included interaction with environments having different stiffnesses and carrying different loads. The closed-loop system exhibited bandwidths of 5 Hz and 3 Hz, when interacting with 125 kN/m and 82 kN/m springs, respectively. Some comparisons between the results in Chapters 5 and 6, are as follows. The maximum bandwidth achieved for the closed-loop system of the electro-hydrostatic actuator, i.e. 5 Hz was less than that of electro-hydraulic actuator, i.e., 6 Hz, for the same amount of stiffness (125 kN/m) and mass (12.3 kg). The step responses of electro-hydrostatic actuator were more damped than step responses of the electro-hydraulic actuator. The lower bandwidth and higher damping in the step responses of the electro-hydrostatic actuator are the results of high inertia of rotational parts in the variable speed electric motor in this actuation system. The QFT controller presented in this chapter was designed based on a limited number of identified frequency responses. These frequency responses did not include the behaviour of the system for all possible values of parameters and/or scenarios. Therefore, this chapter further investigated the stability of the control system expanding the uncertainties to include friction as well as internal and external leakages. The approach taken was to construct a T-S fuzzy model of the electro-hydrostatic actuator. Since the T-S fuzzy model comprises linear local models, it easily incorporated the linear QFT controller and as a result, the whole closed-loop control system was presented by a single T-S fuzzy model. The stability conditions were then presented as LMIs and the stability of the closed-loop system was proven for the wide range of parametric uncertainties and in the presence of uncertain friction, external leakage, and internal leakage in both the pump and the actuator.

Chapter 7

Contributions and Future Directions

7.1 Contributions of this Thesis

This thesis presented a comprehensive study on the design and stability analysis of the output pressure controllers of hydraulic actuators in the presence of parametric uncertainties. The contributions of this thesis can be grouped into two parts. First, using quantitative feedback theory, linear, fixed-gain, robust, and low-order controllers were designed for the output pressure of the hydraulic actuator in this study. This actuator was run by two different actuation systems, electro-hydraulic and electro-hydrostatic. The designed controllers successfully satisfied specified performance criteria consisting of desired time and frequency responses, robust stability, disturbance rejection, and desired tracking bandwidth for the closed-loop system, despite the presence of parametric uncertainties. Second, the nonlinear stability of the designed QFT controllers for the both electro-hydraulic and electro-hydrostatic actuation systems was investigated, using T-S fuzzy modeling and its corresponding stability theorem. This analysis was performed in the presence of uncertainty in the system and environment parameters, as well as the nonlinear friction, and external and internal leakages. The detailed contributions of this thesis are outlined below:

1. Output pressure control of electro-hydraulic actuator

QFT was employed to design a robust, linear, low-order controller for the output pressure of the double-rod electro-hydraulic actuator. The controller satisfied the performance criteria consisting of stability, disturbance rejection, desired transient response, and desired tracking bandwidth in the closed-loop system of output pressure, in the presence of parametric uncertainties. Considering the constraints on the experimental system, such as the supply pressure, servovalve input voltage, and environment stiffness, the performance criteria were specified based on the best achievable responses, from the experimental system. To design the QFT controller, the family of frequency responses was obtained by linearizing the hydraulic nonlinear function around operating points of interest, and constructing an equivalent linear plant set. Towards achieving high bandwidth in the output pressure control, the conflicts between different performance criteria were discussed. It was shown that high bandwidth for the closed-loop system is obtained at the cost of lowering performance in step response, i.e. higher overshoot and longer settling time. This finding was confirmed by the experimental results. For QFT controller that achieved a bandwidth of 6 Hz, the step response showed 22% overshoot and settling time of 1 sec. However when the QFT controller was designed to provide less bandwidth, i.e. 2 Hz, the transient response characteristics were improved, i.e., no overshoot and shorter settling time of 0.4 sec.

2. Output pressure control of electro-hydrostatic actuator

QFT was employed to design a robust, linear, and low-order controller for the output pressure of the double-rod electro-hydrostatic actuator. Performance criteria consisted of closed-loop stability, disturbance rejection, desired transient response, and desired bandwidth in the output pressure tracking, in the presence of parametric uncertainties. The family of frequency responses was obtained by applying an advanced form of fast Fourier transform on the experimental input-output data of the electro-hydrostatic actuator. This approach provided accurate and high quality frequency responses, avoided unnecessary large templates, and resulted in the design of a low-order controller, as compared with the QFT controller designed in Chapter 5 for electro-hydraulic actuator. The results of applying the designed QFT controller on the experimental set-up of electro-hydrostatic actuator, showed the bandwidth of 5 Hz in the sinusoidal tracking, and 5% overshoot and 0.2 sec settling time in step responses. The closed-loop system of the electro-hydrostatic actuator achieved slightly less tracking bandwidth (5 Hz) than that in electro-hydraulic actuator (6 Hz), while had more damped step responses as compared with that in electro-hydraulic actuator. The lower bandwidth and higher damping in the step responses of electro-hydrostatic actuators are the results of high inertia of rotational parts in the variable speed electric motor.

3. *Stability analysis*

The QFT controllers were designed based on families of frequency responses, which represent the physical system only for specified operating conditions or particular values of the parameters. Therefore, the stability of the resultant control systems was only guaranteed for the specified conditions and parameter values. To investigate the nonlinear stability of the control system, for a continuous and wide range of parametric uncertainties and beyond limited number of operating points, a solution was provided in this thesis. In this solution, the Takagi-Sugeno (T-S) fuzzy model of hydraulic actuator was derived and combined with the state-space representation of the designed QFT controllers. The stability conditions were presented in the format of Linear Matrix Inequalities (LMIs). By presenting several case studies, T-S fuzzy modeling and its corresponding stability approach were established as reliable solution that produce correct stability results, can be used to extend stability regions for some existing controllers and to study the nonlinear stability of QFT controllers in fluid power systems. Using T-S fuzzy modeling and its stability theorem, the nonlinear stability of the designed QFT controllers was investigated and proven for both the electro-hydraulic and electro-hydrostatic actuators. The stability analysis was performed in the presence of uncertainty in the system and environment parameters. For electro-hydrostatic actuator, the stability of the closed-loop system was achieved even in the presence of the nonlinear friction, and external and internal leakages.

7.2 Future Work

1- QFT controllers for the electro-hydraulic and the electro-hydrostatic actuators were designed based on the family of frequency responses of the system. These frequency responses were obtained by linearizing the nonlinear model of electro-hydraulic actuator around some operating points or, by applying fast Fourier transform on input-output data, obtained by running the experimental system in certain conditions and excitations, and for specified values of parameters. Therefore, the performance of the designed QFT controllers was guaranteed only over the limited number of operating points or conditions, and specified values of system parameters. To broaden the operating range of the control system without changing the structure of the controller, one way is online tuning of the values of the controller coefficients. In this method, one error minimization approach like gradient decent method can be used to estimate the new coefficients of the controller. This way even if the system is exposed to inputs outside of the acceptable range that the QFT controller was initially designed for, the controller adapts to minimize the error between the desired and actual response. Since only the coefficients of QFT controller are allowed to change, and not the order of the controller, T-S fuzzy modeling and its stability theorem can be employed to analyze the nonlinear stability of the closed-loop system. In deriving the T-S fuzzy model of the closed-loop system, the coefficients of QFT controller should be considered as bounded uncertain parameters.

2- Having more uncertain parameters in the nonlinear model of the hydraulic actuator, the number of local linear models in the corresponding T-S fuzzy model is increased. As a result, it becomes more difficult to find one positive definite matrix to satisfy the stability conditions for all local linear models. On the other hand, literature pointed out that the stability conditions, presented by Tanaka and Sugeno (1992), which used in this thesis, are actually very conservative and likely unsuccessful to deal with highly nonlinear systems (Tanaka et al. 1998; Wang and Sun, 2005). The literature suggested new stability conditions as relaxed versions of conditions presented by Tanaka and Sugeno (1992). By applying the relaxed stability conditions (Tanaka and Wang, 2001), the stability of the designed QFT controllers can be proven for wider ranges of parametric uncertainties than those obtained in Chapters 5 and 6, and in the presence of friction.

References

Ahn, K. and Chau, N. (2006). “Force control of hybrid actuator using learning vector quantization neural network,” *Journal of Mechanical Science and Technology*, Vol. 20, No. 4, pp. 447-454.

Ahn, K., Truong, D., Thanh, T., and Lee, B. (2008). “Online self-tuning fuzzy proportional-integral-derivative control for hydraulic load simulator,” *Proceedings of the Institution of Mechanical Engineers, Part I: Journal of Systems and Control Engineering*, Vol. 222, No. 2, pp. 81-95.

Ahn, K. and Truong, D. (2009). “Online tuning fuzzy PID controller using robust extended Kalman filter,” *Journal of Process Control*, Vol. 19, No. 6, pp. 1011-1023.

Alleyne, A. and Liu, R. (2000). “Systematic control of a class of nonlinear systems with application to electro hydraulic cylinder pressure control,” *IEEE Transaction on Control System Engineering*, Vol. 8, No. 4, pp. 623-634.

Alleyne, A. and Liu, R. (1999). “On the limitations of force tracking control for hydraulic servosystems,” *ASME Journal of Dynamic Systems, Measurement, and Control*, Vol. 121, No. 2, pp. 184-190.

Annus, P., Land, R., Min, M., and Ojarand, J. (2012). *Simple signals for system identification, Fourier transform - signal processing*, Intech.

Astrom, K. (2002). *Control system design.* Lecture notes, University of California.

Barreiro, A. and Banos, A. (2000). “Nonlinear robust stabilization by conicity and QFT techniques,” *Automatica*, Vol. 36, No. 9, pp. 1309-1320.

Banos, A., Barreiro, A., Gordillo, F., and Aracil, J. (2002). “A QFT framework for nonlinear robust stability,” *International Journal of Robust and Nonlinear Control*, *(Isaac Horowitz Special Issue)*, Vol. 12, No. 12, pp. 357-372.

Banos, A. and Horowitz, I. (2004). “Nonlinear quantitative stability,” *International Journal of Robust and Nonlinear Control*, Vol. 14, pp. 289-306.

Bondarev, V.N. (1988). “On system identification using pulse-frequency modulated signals”, EUT report 88-E-195.

Borghesani, C., Chait, Y., and Yaniv, O. (2003). *The QFT frequency domain control design toolbox for use with MATLAB, user's guide*. Terasoft, Inc.

Boyd, S., El Ghaoui, L., Feron, E., and Balakrishnan, V. (1994). *Linear matrix inequalities in system and control theory*. SIAM, Philadelphia, PA.

Bowers, A., Pahle, J., Wilson, R., Flick, B., and Rood, R. (1996). An overview of the NASA F-18 high alpha research vehicle. NASA technical memorandum.

Chinniah, Y. (2004). Fault detection In the electro hydraulic actuator using extended Kalman filter. Doctoral thesis, University of Saskatchewan.

Conrad, F. and Jensen, C. (1988). “Design of hydraulic force control systems with state estimate feedback,” *Automatic Control - World Congress*, Vol. 3, pp. 307-312.

Dimig, J., Shield, C., French, C., Bailey, F., and Clark A. (1999). “Effective force testing: a method of seismic simulation for structural testing,” *Journal of Structural Engineering*, Vol. 125, No. 9, pp. 1028-1037.

Dinh, Q., Ahn, K., and Yoon, J. (2008). “Introduction to quantitative feedback theory for robust force control of load simulator,” *Proceedings of Second International Conference on Communications and Electronics*, pp. 42-47.

D'Azzo, J. and Houpis, C. (1988). *Linear control system analysis and design.* McGraw-Hill.

Du, H. and Zhang, N. (2009). “Static output feedback control for electrohydraulic active suspensions via T-S fuzzy model approach,” *ASME Journal of Dynamic Systems, Measurement and Control*, Vol. 131, No. 5, pp. 1004-1015.

Dyke, S., Spencer, B., Quast, P., and Sain, M. (1995). “Role of control-structure interaction in protective system design,” *Journal of Engineering Mechanics*, Vol. 121, No. 2, pp. 322-338.

Esfandiari, M. and Sepehri, N. (2014). “On high bandwidth output pressure control design of hydraulic actuators using quantitative feedback theory,” *Transactions of the CSME*, Vol. 38, No. 4, pp. 533-555.

Esfandiari, M. and Sepehri, N. (2013). “Stability analysis of QFT controllers designed for hydraulic actuators using Takagi-Sugeno Fuzzy modeling approach,” *Proceedings of the ASME/BATH Symposium on Fluid Power and Motion Control*, pp. V001T01A031-V001T01A031.

Gahinet, P., Nemirovski, A., Laub, A., and Chilali, M. (1995). *LMI control toolbox*. The Math Works Inc.

Golubev, B. and Horowitz, I. (1982). “Plant rational transfer approximation from input-output data,” *International Journal of Control*, Vol. 36, pp. 711-723.

Guzman, J., Rodriguez, F., Moreno, J., Sanchez-Hermosilla, J., and Berenguel, M. (2011). *A frequency domain quantitative technique for robust control system design*. Intech.

Habibi, S. and Goldenburg, A. (1999). “Design of a new high performance electrohydraulic actuator,” *IEEE/ASME Transactions on Mechatronics*, Vol. 5, No. 2, pp. 227-232.

Horowitz, I. (1993). *Quantitative feedback design theory*. Colorado, QFT Publications.

Houpis, C., Rassmussen, S., and Sanz, M. (2005). *Quantitative feedback theory: fundamentals and applications*. CRC Press.

Horowitz, I. (1976). “Synthesis of feedback systems with nonlinear time-varying uncertain plants to satisfy quantitative performance specifications,” *IEEE Transactions on Automatic Control*, Vol. 20, No. 4, pp.454-464.

Hrovat, D. (1997). “Survey of advanced suspension developments and related optimal control applications,” *Automatica*, Vol. 33, No. 10, pp. 1781-1817.

Jacazio, G. and Balossini, G. (2005). “A high performance force control system for dynamic loading of fast moving actuators,” *Power Transmission and Motion Control*, pp. 3-15.

Karpenko, M. and Sepehri, N. (2008). “Equivalem time-invariant modeling of electro hydraulic actuators with application to robust control synthesis,” *International Journal of Fluid Power*, Vol. 9, No. 3, pp. 7-18.

Karpenko, M. and Sepehri, N. (2009). “Hardware-in-the-loop simulator for research on fault tolerant control of electrohydraulic actuators in a flight control application,” *Mechatronics*, Vol. 19, No. 7, pp. 1067-1077.

Karpenko, M. and Sepehri, N. (2012). “Electrohydraulic force control design of a hardware-in-the-loop load emulator using a nonlinear QFT technique,” *Control Engineering Practice*, Vol. 20, No. 6, pp. 598-609.

Kim, J., Xuan, D., and Kim, Y. (2011). “Robust control application for a three-axis road simulator,” *Journal of Mechanical Science and Technology*, Vol. 25, No. 1, pp. 221-231.

Laval, L., M'Sirdi, N., and Cadiou, J. (1996). “H_∞-force control of a hydraulic servo-actuator with environmental uncertainties,” *Proceedings of IEEE International Conference on Robotics and Automation*, Vol. 2, pp. 1566-1571.

Lamming, C. (2009). “Robust electrohydraulic force control,” Transfer report, University of Bath.

Levine, W. (1996). *The control handbook*. CRC press.

Lee, C. (1990). “Fuzzy logic in control systems: fuzzy logic controller. II,” *IEEE Transactions on Systems, Man and Cybernetics*, Vol. 20, No. 2, pp. 419-435.

Liu, R. and Alleyne, A. (2000). “Nonlinear force/pressure tracking of an electro-hydraulic actuator,” *ASME Journal of Dynamic Systems, Measurement, and Control*, Vol. 122, No. 1, pp. 232-237.

Lovrec, D. and Kastrevc, M. (2011). “Modelling and simulating a controlled press-brake supply system,” *International Journal of Simulation Modelling*, Vol. 10, No. 3, pp. 133-144.

Lovrec, D. and Ulaga, S. (2007). “Pressure control in hydraulic systems with variable or constant pumps?,” *Journal of Experimental Techniques*, Vol. 31, pp. 33-41.

Lovrec, D., Kastrevc, M., and Ulaga, S. (2009). “Electro-hydraulic load sensing with a speed-controlled hydraulic supply system on forming-machines,” *International Journal of Advanced Manufacturing Technology*, Vol. 41, pp. 1066-1075.

Merritt, H. (1967). *Hydraulic Control Systems*. New York, Wiley.

Melik-Gaikazov, V., Navrotskii, K., and Romashkin, M. (1975). “Control systems of hydraulic drives of crane mechanisms,” *Russian Engineering Journal*, Vol. 55, No. 10, pp. 56-60.

Nam, Y. (2001). “QFT force loop design for the aerodynamic load simulator,” *IEEE Transaction on Aerospace and Electronic Systems*, Vol. 37, No. 4, pp. 1384-1392.

Nabulsi, S., Sarria, J., and Armada, M. (2007). "Indirect force measurement for hydraulic walking robot," *Proceedings of the IEEE International Symposium on Intelligent Signal Processing*, pp. 1-6.

Newton, R. (1969). Hydraulic actuator for an injection molding machine. *U.S. Patent* No. 3,452,397.

Nahvi, M.; Hoyle, B. S. (2009). "Electrical Impedance Spectroscopy Sensing for Industrial Processes," *IEEE Sensors Journal*, Vol. 9, No. 12, pp.1808-1816.

Niksefat, N. and Sepehri, N. (1999). "Robust force controller design for a hydraulic actuator based on experimental input-output data," *Proceedings of the American Control Conference*, Vol. 5, pp. 3718-3722.

Niksefat, N. and Sepehri, N. (2000). "Design and experimental evaluation of a robust force controller for an electro-hydraulic actuator via quantitative feedback theory," *Control Engineering Practice*, Vol. 8, pp. 1335-1345.

Niksefat, N. and Sepehri, N. (2001). "Designing robust force control of hydraulic actuators despite system and environmental uncertainties," *IEEE Control Systems Magazine*, Vol. 21, No. 2, pp. 66-77.

Ohtake, H., Tanaka, K., and Wang, H. (2003). "Fuzzy modeling via sector nonlinearity concept," *Integrated Computer-Aided Engineering*, Vol. 10, No. 4, pp. 333-341.

Plummer, A. (2007). "Robust electrohydraulic force control," *Proceedings of the Institution of Mechanical Engineers, Part I. Journal of Systems and Control Engineering*, Vol. 221, No. 4, pp. 717-31.

Radermacher, T., Weber, J., and Dorner, D. (2013). "Dynamic force control of displacement controlled drives by means of an iterative learning algorithm," *Proceedings of the ASME/BATH Symposium on Fluid Power and Motion Control*, pp. V001T01A058-V001T01A058.

Robinson, D. (2000). Design and analysis of series elasticity in closed-loop actuator force control. Doctoral thesis, Massachusetts Institute of Technology.

Rowell, D. (2002). Analysis and design of feedback control systems. Course handout, Massachusetts Institute of Technology.

Rupnik, B. (2005). CIFER®-MATLAB interfaces, development and application. Master thesis, California Polytechnic State University.

Sivaselvan, M., Reinhorn, A., Shao, X., and Weinreber. S. (2008). "Dynamic force control with hydraulic actuators using added compliance and displacement compensation," *Earthquake Engineering & Structural Dynamics*, Vol. 37, No. 15, pp.1785-1800.

Takagi, T. and Sugeno, M. (1985). "Fuzzy identification of systems and its applications to modeling and control," *IEEE Transactions on Systems, Man and Cybernetics*, Vol. 1, pp. 116-132.

Tanaka, K. and Sugeno, M. (1992). "Stability analysis and design of fuzzy control systems," *Fuzzy sets and systems*, Vol. 45, No.2, pp.135-156.

Tanaka, K., Ikeda, T., and Wang, H. (1998). “Fuzzy regulators and fuzzy observers: relaxed stability conditions and LMI-based designs,” *IEEE Transactions on Fuzzy Systems,* Vol. 6, No. 2, pp. 250-265.

Tanaka, K. and Wang, H. (2001). *Fuzzy control systems design and analysis*. Jon Wiley & Sons.

Tischler, M. and Remple, R. (2012), *Aircraft and rotorcraft system identification,* Second Edition, American Institute of Aeronautics and Astronautics, New York.

Truong, D., Ahn, K., Soo, K., and Soo, Y. (2007). “Application of fuzzy-PID controller in hydraulic load simulator,” *Proceedings of International Conference on Mechatronics and Automation*, pp. 3338-3343.

Truong, D. and Ahn, K. (2011). “Force control for press machines using an online smart tuning fuzzy PID based on a robust extended Kalman filter,” *Expert Systems with Applications,* Vol. 38, No. 5, pp. 5879-5894.

Truong, D., Kwan, A., and Yoon, J. (2008). “A study on force control of electric-hydraulic load simulator using an online tuning Quantitative Feedback Theory,” *Proceedings of International Conference on Control, Automation and Systems,* pp. 2622-2627.

Tran, X., Hafizah, N., and Yanada, H. (2012). “Modeling of dynamic friction behaviors of hydraulic cylinders,” *Mechatronics,* Vol. 22, No. 1, pp. 65-75.

Turolla (2013), Hydraulic fluids & lubricant. Technical information.

Vossoughi, G. and Donath, M. (1995). “Dynamic feedback linearization for electrohydraulically actuated control systems,” *ASME Journal of Dynamic Systems, Measurement, and Control*, Vol. 117, pp. 468–477.

Wang, W. and Sun, C. (2005). “Relaxed stability and stabilization conditions for a T–S fuzzy discrete system,” *Fuzzy Sets and Systems,* Vol. 156, No. 2, pp. 208-225.

Wang, T., Hwang, Y., and Tsai, T. (1990). “Synthesis of feedback control systems with large plant uncertainty and time-varying gain,” *International Journal of Control,* Vol. 51, No. 3, pp. 687-704.

Xu, Z. and Da, Q. (2003). “An overview of operators for aggregating information,” *International Journal of Intelligent Systems,* Vol. 18, No.9, pp. 953-969.

Yao, J., Jiao, Z., Yao, B., Shang, Y., and Dong, W. (2012). “Nonlinear adaptive robust force control of hydraulic load simulator,” *Chinese Journal of Aeronautics,* Vol. 25, No. 5, pp. 766-775.

Yao, B., Bu, F., Reedy, J., and Chiu, G. (2000). “Adaptive robust motion control of single-rod hydraulic actuators: theory and experiments,” *IEEE/ASME Transactions on Mechatronics,* Vol. 5, No. 1, pp. 79-91.

Yaniv, O. (1999). *Quantitative feedback design of linear and nonlinear control systems*, Kluwer.

Zarei-Nia, K. and Sepehri, N. (2012). “Lyapunov stable displacement-mode haptic manipulation of hydraulic actuators, Theory and experiment,” *International Journal of Control,* Vol. 85, No. 9, pp. 1313-1326.

Zhu, W. and Piedboeuf, J. (2005). “Adaptive output force tracking control of hydraulic cylinders with application to robot manipulators,” *ASME Journal of Dynamic Systems, Measurement, and Control*, Vol. 127, No. 2, pp. 206-217.